Fundamental and Applied Studies on Self-assembling of Polymer-brush-modified Nanoparticles in Ionic Liquid

Yohei Nakanishi

2018

Fundamental and Applied Studies on Self-assembling of Polymer-brush-modified Nanoparticles in Ionic Liquid

Yohei Nakanishi

2018

Department of Polymer Chemistry

Graduate School of Engineering, Kyoto University

Contents

Chapter 1 General Introduction **1**

Chapter 2 USAXS Analysis of Concentration-dependent Self-assembling of Polymer-brush-modified Nanoparticles in Ionic Liquid: [I] Concentrated-brush Regime **21**

Chapter 3 USAXS Analysis of Concentration-dependent Self-assembling of Polymer-brush-modified Nanoparticles in Ionic Liquid: [II] Semi-diluted-brush Regime **43**

Chapter 4 USAXS Analysis of Concentration-dependent Self-assembling of Polymer-brush-modified Nanoparticles in Ionic Liquid: [III] Unified Explanation **57**

Chapter 5 Understanding Dynamics of Self-Assembling of Polymer-brush-modified Nanoparticles/Ionic Liquid Composites by Shear Oscillation **73**

Chapter 6 Understanding Dynamics of Self-Assembling of Polymer-Brush-Modified Nanoparticles/Ionic Liquid Composites by Dip-coating Method **85**

Chapter 7 Fabrication of quasi-solid electrolyte of concentrated-polymer-brush-modified nanoparticles self-assembled in iodide-containing ionic liquid toward dye-sensitized solar cell **101**

Summary **119**

List of Publications **121**

Acknowledgements **123**

Chapter 1

General Introduction

1-1. Colloidal crystals

Solid–liquid–gas phase transition is one of fundamental properties in chemistry, which have received sufficient attention among the various researchers. Among others, the crystallization is of great importance not only in basic science but also for many applications, because the control of structure can induce a novel function of materials. Colloidal crystals, which can be formed by colloidal particles in a solvent, are useful to understand the phase transition and crystallization process instead of atoms or molecules. Many groups have been researching a variety of colloidal crystals not only as fundamentals including theoretical, simulational, and experimental studies but also as applications for photonic,[1-4] phononic,[5-7] chemical and bio-sensing materials.[8] These applications are related to the properties characteristic to the colloidal crystal with an interparticle distance in the order of a visible-light wavelength. As general topics of colloidal crystals, static and kinetic aspects are discussed. Static aspects are related to thermodynamic properties, determined by interparticle potential, particle concentration, and temperature. On the other hand, kinetic aspects include crystal nucleation and growth. In general,

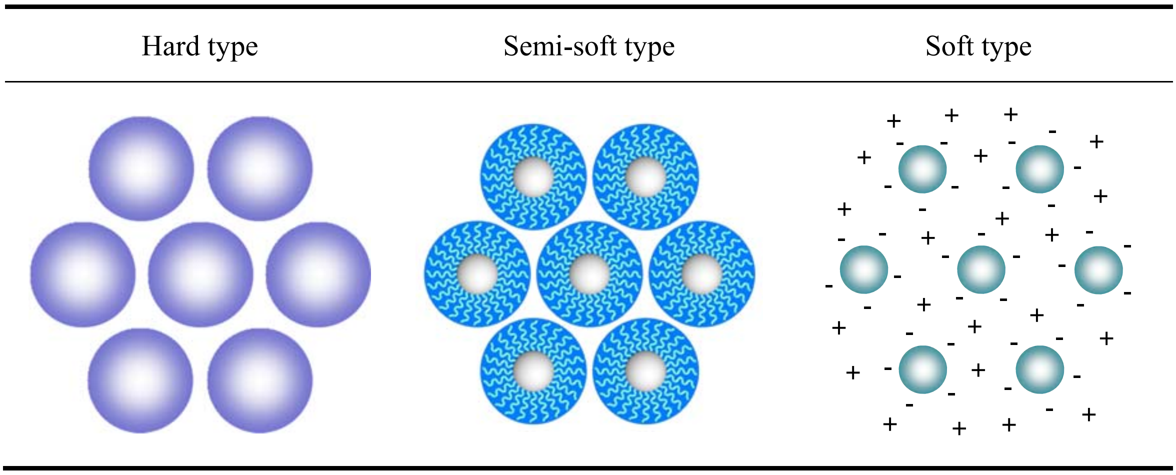

Figure 1-1. Schematic illustration of colloidal crystals of different types.

colloidal systems are divided into three categories, i.e., "hard",[9-14] "soft",[15-23] and "semi-soft" types,[24-29] depending on the interparticle interaction of different origins, i.e., a hard-sphere repulsion, electrostatic interaction, and steric repulsion between swollen polymer brushes, respectively (see Figure 1-1). Major types of higher-order structures include the hexagonal close-packed (hcp), the face-centered cubic (fcc), the random hexagonal close-packed (rhcp) and the body center cubic (bcc) lattices. The first three have the same packing fraction of 74 % at the 3-dimensionally densest packing of equal spheres and the difference in the stacking sequence of the 2-dimensionally hexagonal closed-packed (hcp) plane (see Figure 1-2). There are three equivalently projected hcp planes (A, B, and C). The hcp, fcc, and rhcp consist of the two planes alternately stacked (ABABAB…), three planes regularly stacked (ABCABC…), and three planes randomly stacked, respectively. Previous and current research on these three types of colloidal crystals is briefly reviewed in the following sessions.

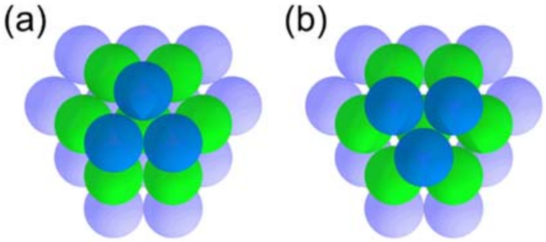

Figure 1-2. Schematic illustration of particle stacking in (a) fcc (ABC-stacking) and (b) hcp (ABA-stacking) structures.

1-1-1. Hard spheres

Because of the conceptual simplicity of the phase behavior, the interaction, and the importance of packing effects of colloidal particles in many systems, a purely repulsive hard sphere is one of the simplest models to understand the fundamental aspects of colloidal systems including a phase behavior, analogous to that of atomic and molecular substances. The interaction potential of hard spheres ($V_{\mathrm{HS}}(r)$) is defined as follows:

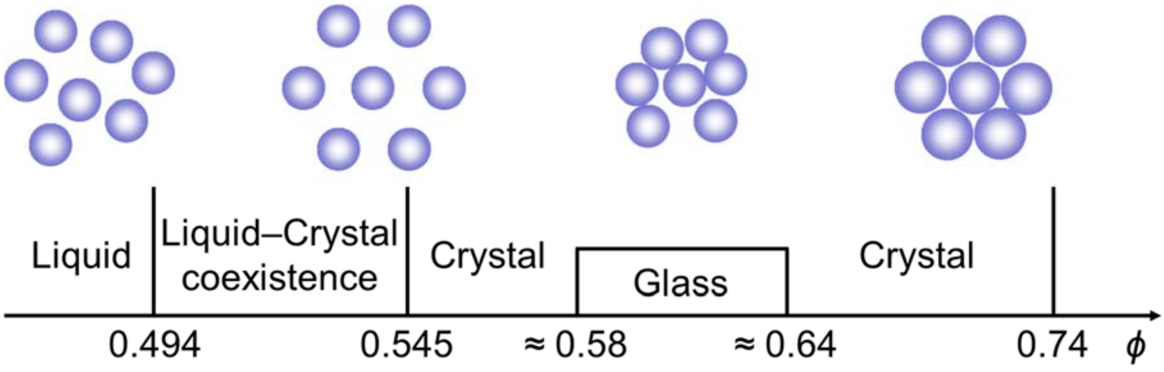

Figure 1-3. The phase diagram of hard spheres depending on the volume fraction ϕ.

$$V_{\mathrm{HS}}(r) = \begin{cases} \infty & \text{for } r \le \sigma \\ 0 & \text{for } r > \sigma \end{cases} \quad (1\text{-}1)$$

where r and σ are the mutual particle distance and the "effective" radius of hard spheres, respectively. So their phase behavior is determined by entropy and depends on volume fraction ϕ.[30,31] Figure 1-3 shows the proposed phase diagram for hard spheres as a function of ϕ. Colloidal particles in the suspension randomly move, which is well known as Brownian motion. Kirkwood discussed that the transition from liquid to crystal may occur when the volume fraction of the particles is exceeded by a certain value in hard sphere systems.[32] And then, the computer simulations predicted that this transition for hard sphere systems occurs at ϕ = 0.494 ~ 0.545 as a liquid/crystal-coexisting region.[33,34] This transition is well known as the Kirkwood–Alder transition and understood by the translational entropy of the particle gained by ordering. The computer simulations also suggest the formation of the colloidal crystal of rhcp,[10,35] because there is little difference in free energy between the fcc and hcp lattices.[36-39] The colloidal-crystal structure is expected to be affect by the sedimentation and gravity. Some experiments were performed in microgravity.[14] In order to experimentally demonstrate some predictions for the above-mentioned hard-sphere system, there have been extensive studies using inorganic or polymer bulk spheres sterically stabilized with a thin layer of poly-hydroxystearic acid[10,14] (modified by grafting-to method) or hydrocarbons and dispersed in apolar solvents without agglomeration.[40] In hexagonally close-packed system, the ordered close packing with ϕ = 0.74 is the densest possible packing in three dimensions,[34] while it is reduced to ϕ = 0.64 for a disordered particle configuration, called as random close packing.[41-43] At middle volume fraction, a glass transition is observed at $\phi \approx$ 0.58,[10,44,45] so the range of volume fraction for colloidal glass was considered to be as $0.58 < \phi < 0.64$.

1-1-2. Charged and soft particles

An advantage of charged colloidal suspensions is that the interaction potential can be systematically tuned from a long ranged soft (10^{-6} M salt concentration) to a short-ranged hard sphere-like potential (10^{-4} M salt concentration). A large number of research papers have already published from various groups especially for the "soft" colloidal crystal formed by the electrostatic (Coulomb) potential. In the most common theoretical and simulational studies, the interparticle interaction of core particles with surface charges were modelled using Yukawa potential or Debye-Hückel potential, which was adjusted in surface potential and screening length by tuning the particle charge, the particle number density and the electrolyte concentration.[46] This simulation predicted the phase diagram containing the bcc structure at low particle and electrolyte concentrations in addition to fcc structure.[47-49] Figure 1-4 shows an example of phase diagram of charged particles, in which liquid, bcc, fcc, and glass-like phases

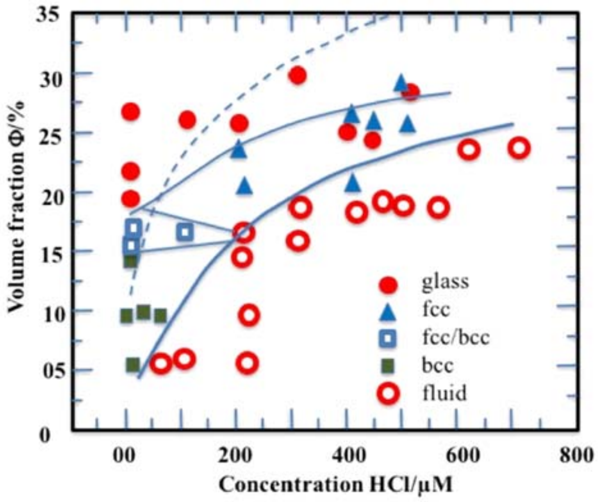

Figure 1-4. An example of phase diagram of soft type colloidal system, volume fraction ϕ as the function of electrolyte concentration (ref. 47).

are observed. The excess of screening ions leads to a reduced electrostatic repulsion and a decrease of the strength of interaction where no crystals of long-range order exist. In addition, the bcc structure formed at the liquid/crystal-threshold concentration is considered to be characteristic to the soft system. This was experimentally confirmed with the suspension of charged silica and polymeric-latex particles.[50-53]

Another examples categorized into the soft system include polymeric nanocolloids such as dendrimers, star polymers, and block-copolymer micelles, self-organizing in a number of ordered structures. By tuning copolymer molecular weight and composition, solution concentration, monomer incompatibility, and temperature, the colloidal crystals of the bcc as well as fcc structures were experimentally demonstrated to be formed.[54-60] The driving force was the electrostatic interaction in some of them and the steric hindrance, i.e., the osmotic pressure increasing with overlapping of swollen polymer segments in others.

1-1-3. Polymer brush-modified particles

Well-defined and low-polydispersity polymers can be densely grown up on various solid surfaces by living radical polymerization[61-67] (LRP; also called controlled reversible-deactivation radical polymerization as per the IUPAC recommendation). The graft density in such cases is more than one order of magnitude higher than that of a typical "semidilute" polymer brush (SDPB), going deep into the "concentrated"-brush regime.[68-71] Graft chains of such a concentrated polymer brush (CPB) in a good solvent are highly extended, almost to their full lengths, because of the exceptionally high osmotic pressure of the brush.[68,72-74] Because of such a highly stretched conformation, CPB in a good solvent exhibits characteristics such as high resistance against compression described in Figure 1-5, very less mutual interpenetration that gives rise to very high lubrication with an extremely low friction coefficient ($\mu \sim 10^{-4}$),[68,69,75] and definite size exclusion with a very low threshold of molecular weight that gives good biocompatibility in an aqueous system.[68,76,77]

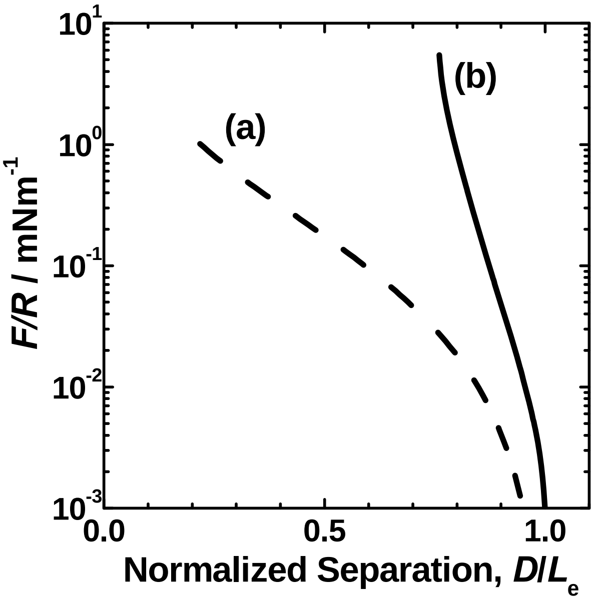

Figure 1-5. Scaled force profiles (*F*/*R* vs *D*/L_e curves) plotted in semilogarithmic scale: (a) SDPB and (b) CPB.

The above-mentioned high-density grafting has been achieved even on colloid particles, giving a broad range of polymer-brush-modified and core-shell-type particles including as cores, specifically silica particles (SiP) as well as various metal nanoparticles, semiconductor nanoparticles, metal oxide particles, carbon nanotubes, carbon nanoparticles, and the like. Previously, our group succeeded in synthesizing a series of PSiP with a CPB of PMMA with high uniformity and high dispersibility and firstly demonstrated that these polymer-grafted hybrid nanoparticles (PSiP) were crystallized at a certain concentration of a dispersed solution with the help of highly repulsive and lubricating properties of the CPB layer. The obtained colloid crystals of PSiPs can be distinguished as a "semisoft" type[24-29] in contrast to the previously reported "hard"[9-14] and "soft"[15-23] types which are formed by a hard-sphere and electrostatic interactions, respectively, as mentioned above.

As illustrated in Figure 1-6, the "effective" graft density at the outermost surface of the swollen polymer-brush layer should decrease with increasing thickness on a spherical-particle surface. On the basis of the Daoud-Cotton scaling model, the polymer-brush layer was revealed to be divided into the inner CPB and outer SDPB layers at a virtual interface of certain critical radius.[25,78-80] Correspondingly, there was observed a change in the structure of colloidal crystals from rhcp to fcc structures. Interestingly,

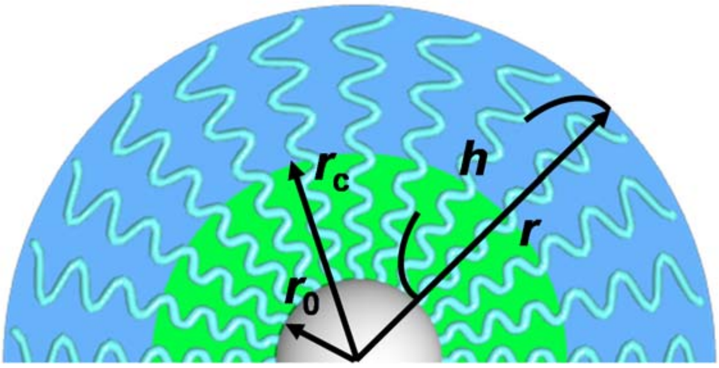

Figure 1-6. Schematic representation of the radius r_0 of core particle, the radius r of hybrid particle, the thickness h of brush layer, and the concentrated-to-semidilute (CPB-to-SDPB) crossover radius r_c.

this boundary of molecular weight corresponded to a surface occupancy of 10% at a virtual surface formed by completely elongated chains. This was eventually identical to the crossover density between SDPB and CPB estimated on the flat surface. Since these higher-order structures are formed by the steric hindrance of swollen brushes, the above-mentioned semi-soft colloidal crystals can be formed even in IL in which the electrostatic interactions are shielded.

1-1-4. Crystal nucleation

Crystallization, which means that liquid changes into solid, evolutions in both symmetry and density take place, is an important process in condensed-matter physics and material science. A lot of researches about crystal nucleation of colloidal crystal have been reported, determining the nucleation rates and the growth laws in colloidal suspensions.[11,30,47,81-83] Small-angle light scattering were common methods for the determination of nucleation rates, which is sensitive to large scale density fluctuations. Crystal nuclei are denser than the liquid around them because of the larger density of the crystal as well as Laplace pressure, which means the pressure deference between the inside and outside of a curved surface that forms the boundary between two-regions. As shown in Figure 1-7,[81] homogeneous nucleation rate density J is found to grow with increasing ϕ until it reaches its maximum at $\phi \approx 0.545$, which is the melting point. On the other hand, for higher ϕ, J decreases and vanishes at the glass

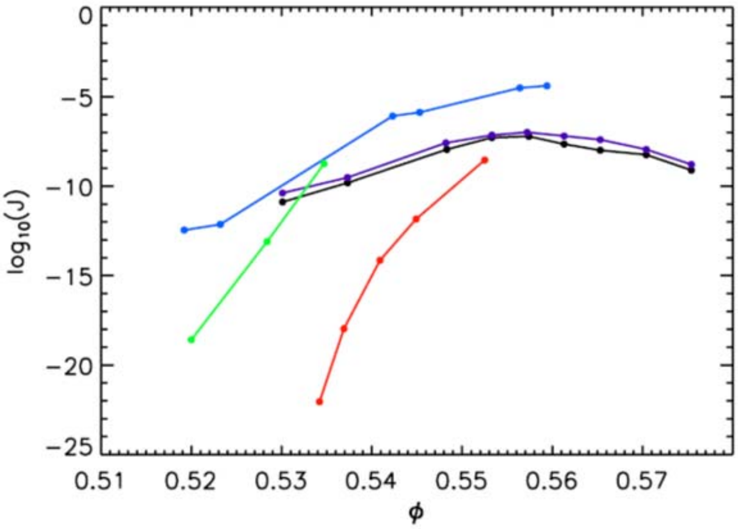

Figure 1-7. Nucleation rate density J of hard spheres as a function of volume fraction ϕ observed in experiments ((purple) maximal nucleation rate density J_{max} and (black and blue) average J) and simulations ((green) monodisperse hard spheres and (red) polydisperse hard spheres). This figure is cited from ref. 81.

transition. The maximum of the nucleation rate is then attributed to a decrease of the rate with which particles can be incorporated into nuclei with a volume fraction in liquid–crystal coexistence region. In terms of the theory and simulation studies, the classical nucleation theory (CNT) provides a nice framework in order to understand crystallization, which indicates that the crystallization kinetics proceeds as nucleation and growth of small crystals. However, it is well-recognized that CNT doesn't provide all aspects of crystallization process. CNT explains that the density variation accompanying symmetry transformation is within one step. On the other hand, recent simulation researches indicate that the possibility of either a two-step variation where densification precedes other construction,[84] or a gradual transition in both symmetry and density driven by the bond order fluctuation.[85,86]

1-1-5. Ultra-small-angle X-ray scattering

The structure of colloidal systems can be examined in different ways. Optical microscopy, and especially confocal laser scanning microscopy are widely used techniques. These methods, however, are severely limited in terms of their resolution. Scanning electron microscopy (SEM) can provide high spatial resolution; however, due to low penetration depth of electrons, SEM can only access the surface structure of a colloidal crystal and typically involves elaborate sample preparation. Among the various methods available for structural analyses, small-angle X-ray scattering (SAXS) method is one of the most powerful techniques, indeed, various researches on the structures of materials containing nanoparticles with polymers using SAXS were reported.[87-90] The scattered intensities are expressed as a function of the scattering vector, $q = (4\pi \sin\theta)/\lambda$, where 2θ is the angle between the incident X-ray beam and the detector measuring the scattered intensity, and small-angle generally means $\theta < 10°$. The q value was calibrated using a collagen fiber extracted from a chicken leg. Recent technological advance, including the development of synchrotron beams, enables us to obtain X-ray-scattered images of materials in the range below 0.1°, categorized as ultra-small-angle X-ray scattering (USAXS). USAXS was used to analyze the higher-order structure of polymer-brush-modified nanoparticles in a stretched polymer film.[91,92] These results demonstrated that the USAXS method can be used effectively for a colloidal system.

1-2. Background and purposes of this thesis

There are various theoretical and simulational studies about the concentration-dependent self-assembling, i.e., the crystal formation of colloidal suspension. Many of them, however, targeted the order-disorder transition and hence its nearby concentration range but little on a higher concentration one, which might be difficult to experimentally approach because of difficulty in homogenous and concentrated dispersion of colloids. This is attempted to be overcome as follows: an appropriate amount of PSiP is dispersed in a mixture of ionic liquid (IL) and a volatile co-solvent and cast on a substrate. By slowly vaporizing the co-solvent, the particle concentration in the suspension is expected to gradually increase with keeping homogeneity, giving a homogenous PSiP/IL mixture even at a finally high particle concentration. Another important point in this system is higher density and viscosity of an IL. Higher density can suppress sedimentation of PSiP. Of course, higher viscosity is not good for keeping sufficient mobility and then self-assembling PSiPs in a high-concentration suspension. In this regard, it should be noted that in many ILs, the viscosity becomes high because of strong interaction or clustering of ionic molecules and hence dramatically decreases by the addition of a small amount of organic solvent. This means that the mobility (involving Brownian motion) of the PSiP may be kept even at a high concentration of PSiP/IL mixture. Better mobility may also be enhance by the highly lubricating property especially for the PSiP with a polymer-brush layer in the CPB regime.

In the case of PSiP, the effective diameter is one of the structural parameters especially important from the viewpoint of colloidal crystallization, e.g., for theoretically calculating the PSiP concentration at the Kirkwood–Alder transition. The determination of the effective diameter of PSiP, which is the challenging issue, is attempted not only by the SAXS as well as DLS measurements. Especially for the former, the following points are discussed; how the SAXS data should be analyzed and whether or not Percus–Yevick model[93-95] can be a sufficiently good model for this. In the case of PSiP, the interparticle potential relating to the dynamics and higher-order structure of the colloidal crystal can be tuned by the length of polymer brush grafted on a nanoparticle. Previous work by our group reported that PSiPs self-assemble in the rhcp or fcc structure in an organic solvent at the liquid/crystal-threshold concentration[96], while they assemble in the fcc structure in ionic liquid at the concentration giving a closed packing of PSiP.[97,98] Thermodynamic equilibrium was confirmed for the former but not for the latter, since the latter was discovered at the application of such a self-assembled structure as a novel quasi-solid electrolyte to a bipolar-type lithium-ion rechargeable battery. Therefore, a detailed and systematic study of the PSiP self-assembling process in an IL in a wide range of particle concentration should be required not only for further understanding the science of the semisoft-type colloidal crystal but also for developing high-performance electrochemical devices.

1-3. The outline of this thesis

The purposes of this thesis are divided into three parts: (i) clarifying the concentration dependence of structures of polymer-brush-modified nanoparticles (PSiPs) in IL, (ii) observing the process of structure formation and controlling the orientation of PSiPs, and (iii) applying PSiPs to functional materials.

In **Chapter 2**, I focus on the colloidal system, in which the main component of the interparticle interactions is set to be the completely repulsive interaction between the swollen CPBs. Thus, the PSiP with a polymer-brush layer in the CPB regime is targeted, being achieved by a sufficiently short graft chain as well as a sufficiently high graft density. Specifically, the CPB of the IL-type polymer with a length approximately 1/10 as long as the SiP-core diameter is synthesized and dispersed in the similar kind of IL, i.e., DEME-TFSI. This meets the good-solvent condition, i.e., the indispensable requirement for the expected CPB effect being valid. Another important point in the strategy of this chapter is the homogeneous mixing of the PSiP and IL in a wide range of concentration, which is successfully achieved by the ingenious casting method using a volatile co-solvent. The swollen-CPB and higher-order structures of the obtained PSiP/IL blends with different compositions are analyzed by the USAXS technique and discussed from the viewpoint of concentration-dependent self-assembling, i.e., the formation of a colloidal crystal in the comparison with the previously studied colloidal systems, i.e., a hard or soft colloidal system.

In **Chapter 3**, I focused on the PSiP with an outermost surface of the swollen polymer-brush layer in the SDPB regime in order to discuss how the interparticle interaction affects the higher-order structure of PSiP between the CPB and SDPB regimes by the preparation and analysis techniques similar to Chapter 1. Here, PMMA with a sufficiently high molecular weight is used as a polymer-brush component by taking account of the following points; DEME-TFSI is also a good solvent for PMMA (which is demonstrated by the DLS measurement), and for the PMMA, the cross-over length between the CPB and SDPB regimes at the outermost surface was already experimentally determined. Among the discussion on the concentration-dependent self-assembling, special attention is paid for a bcc structure, which is typical for a "soft" colloidal system but never observed for the PSiP system with a high graft density.

In **Chapter 4**, the self-assembled, higher-order structures of the PSiP in IL are investigated on some additional PSiP samples and totally discussed along with the data reported in Chapters 2 and 3. The phase diagram is given as a function of polymer-brush length (degree of polymerization of the polymer brush) and particle concentration. These two parameters are expected to correspond to the softness of the interparticle interaction and the pressure of the system (affecting the compression of the swollen polymer-brush layer and hence the repulsion force), respectively. The discussion points include the concentration and structure at the threshold concentration of the liquid/crystal states from the viewpoint of the Kirkwood–Alder transition and the effect of the high compression of the swollen polymer-brush layer corresponding to e.g., the soft shell system and a high particle-concentration regime.

In **Chapter 5**, the higher-order structural formation of CPB-PSiP in ionic liquid is investigated under shear oscillation using *in-situ* USAXS measurement. The dynamics of the self-assembling process in the field of colloidal science and technology one of current topics. The present system, i.e., the PSiP with a CPB shell, is also interesting, since it can be regarded as a good model for the hard-sphere model, which is extensively studied by theory and simulation. First of all, the shear condition to repeatedly produce a disordered state is explored. Then, the self-assembling process is monitored and discussed about its rate constant under an appropriate condition of oscillating shear, which is strong enough to locally change the relative position of the PSiP (which is difficult at thermal perturbation) but weak enough not to disturb the ordered state.

In **Chapter 6**, the higher-order structure of the dip-coated PSiP/IL composite and the process of its structural formation is revealed using the USAXS and GISAXS measurements, since the dip-coating process is important as one of the most powerful and simple tools for fabricating highly oriented colloidal crystals not only in the fundamental interests but also toward a variety of application. For this, the particle concentration and interparticle ordering must be determined near the meniscus formed at the dipping a solution containing PSiP, IL and volatile solvent, which is successfully achieved by the *in-situ* simultaneous measurement of USAXS and X-ray absorption.

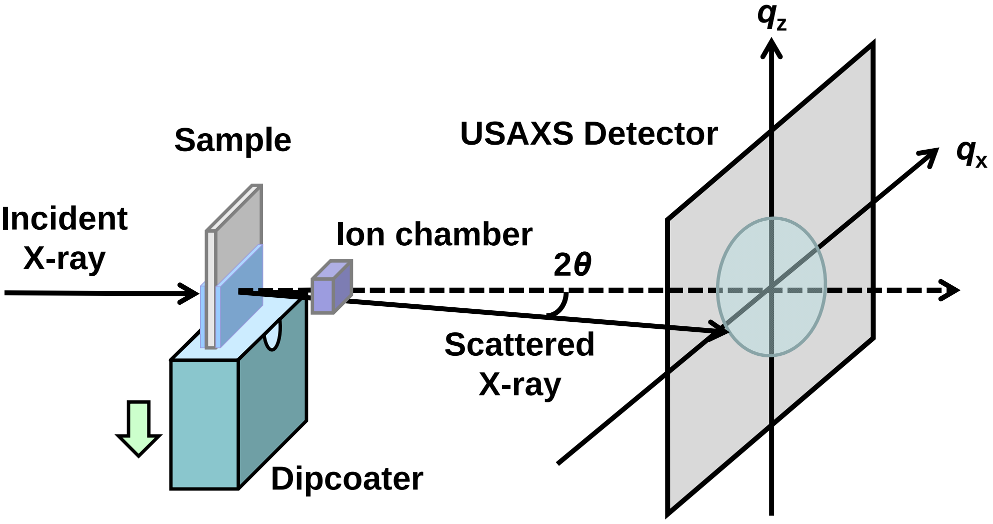

Figure 1-8. Schematic illustration of USAXS measurement using dip-coater. An ion chamber is used for measuring X-ray absorption.

In **Chapter 7**, the quasi-solid and iodide-redox electrolyte membrane of PSiP/IL is fabricated by the dip-coating technique described in Chapter 6 and applied to the dye-sensitized solar cell (DSSC). The solidification of electrolyte without spoiling the ion-conductivity has been required for a long time, and the PSiP/IL system can be one of the most high-performance system. First of all, the self-assembling of PSiP in the iodide-redox-containing IL is explored especially from the prediction that the PSiP must be self-assembled with the help of the CPB effect, that the affinity between the polymer-brush component and the dispersion medium, i.e., the iodide/iodine-containing IL in this study. Finally, the photovoltaic performance of the DSSC prepared by this membrane is discussed from the viewpoint of ionic conductivity, electron-transfer efficiency/rate at the interface of the electrodes, and so on.

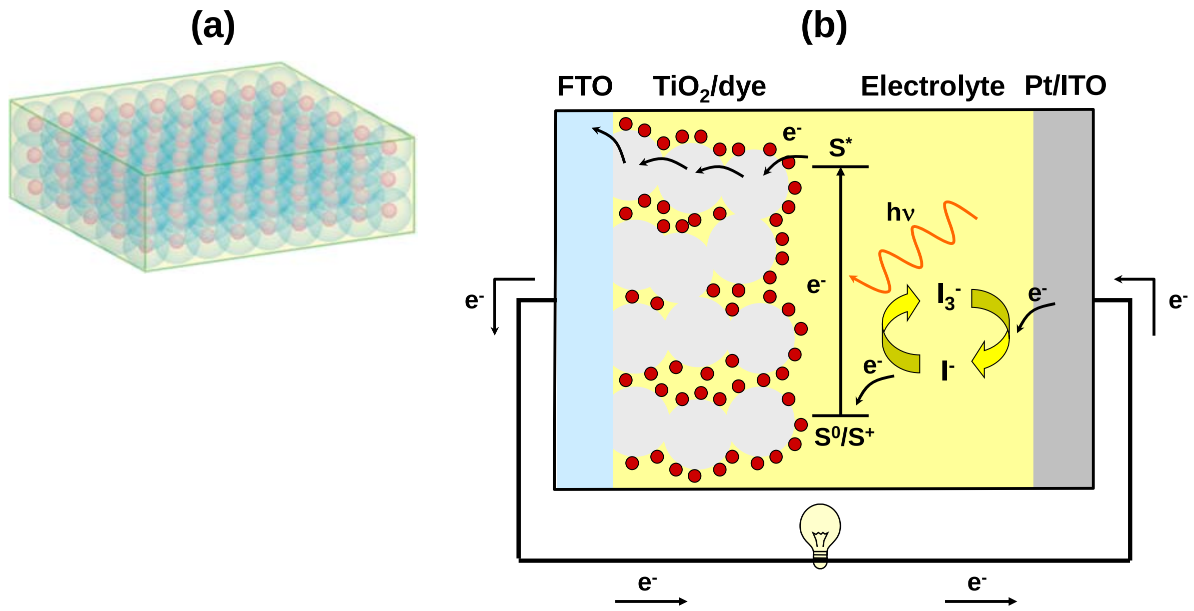

Figure 1-9. Schematic illustration of (a) the electrolyte consisting of PSiP/IL composites and (b) the dye-sensitized solar cell.

References

1. E. Yablonovitch. *Phys. Rev. Lett.* **1987**, *58*, 2059–2062.

2. S. John. *Phys. Rev. Lett.* **1987**, *58*, 2486–2489.

3. J. M. Weissman, H. B. Sunkara, A. S. Tse, S. A. Asher. *Science* **1996**, *274*, 959–960.

4. H. S. Yang, J. Jang, B. S. Lee, T. H. Kang, J. J. Park, W. R. Yu. *Langmuir* **2017**, *33*, 9057–9065.

5. E. Alonso-Redondo, M. Schmitt, Z. Urbach, C. M. Hui, R. Sainidou, P. Rembert, K. Matyjaszewski, M. R. Bockstaller, G. Fytas. *Nat. Commun.* **2015**, *6*, 8309.

6. W. Cheng, J. J. Wang, U. Jonas, G. Fytas, N. Stefanou. *Nat. Mater.* **2006**, *5*, 830–836.

7. T. Still, W. Cheng, M. Retsch, R. Sainidou, J. Wang, U. Jonas, N. Stefanou, G. Fytas. *Physical Review Letters* **2008**, *100*, 194301.

8. J. H. Holtz, S. A. Asher. *Nature* **1997**, *389*, 829–832.

9. W. K. Kegel, A. van Blaaderen. *Science* **2000**, *287*, 290–293.

10. P. N. Pusey, W. Vanmegen. *Nature* **1986**, *320*, 340–342.

11. W. Vanmegen, S. M. Underwood. *Nature* **1993**, *362*, 616–618.

12. A. Kose, S. Hachisu. *J. Colloid Interface Sci.* **1974**, *46*, 460–469.

13. Z. D. Cheng, W. B. Russell, P. M. Chaikin. *Nature* **1999**, *401*, 893–895.

14. J. X. Zhu, M. Li, R. Rogers, W. Meyer, R. H. Ottewill, W. B. Russell, P. M. Chaikin. *Nature* **1997**, *387*, 883–885.

15. S. Hachisu, Y. Kobayashi, A. Kose. *J. Colloid Interface Sci.* **1973**, *42*, 342–348.

16. S. Hachisu, K. Takano. *Adv. Colloid Interface Sci.* **1982**, *16*, 233–252.

17. I. S. Sogami, T. Yoshiyama. *Phase Transitions* **1990**, *21*, 171–182.

18. R. Williams, R. S. Crandall. *Phys. Lett. A* **1974**, *48*, 225–226.

19. N. A. Clark, A. J. Hurd, B. J. Ackerson. *Nature* **1979**, *281*, 57–60.

20. H. Yoshida, J. Yamanaka, T. Koga, N. Ise, T. Hashimoto. *Langmuir* **1998**, *14*, 569–574.

21. H. Yoshida, K. Ito, N. Ise. *Phys. Rev. B* **1991**, *44*, 435–438.

22. P. A. Hiltner, I. M. Krieger. *J. Phys. Chem.* **1969**, *73*, 2386–2389.

23. T. Okubo. *Prog. Polym. Sci.* **1993**, *18*, 481–517.

24. K. Ohno, T. Morinaga, S. Takeno, Y. Tsujii, T. Fukuda. *Macromolecules* **2006**, *39*, 1245–1249.

25. K. Ohno, T. Morinaga, S. Takeno, Y. Tsujii, T. Fukuda. *Macromolecules* **2007**, *40*, 9143–9150.

26. T. Morinaga, K. Ohno, Y. Tsujii, T. Fukuda. *Macromolecules* **2008**, *41*, 3620–3626.

27. T. Morinaga, K. Ohno, Y. Tsujii, T. Fukuda. *Eur. Polym. J.* **2007**, *43*, 243–248.

28. Y. Huang, T. Morinaga, Y. Tai, Y. Tsujii, K. Ohno. *Langmuir* **2014**, *30*, 7304–7312.

29. Y. Huang, A. Takata, Y. Tsujii, K. Ohno. *Langmuir* **2017**, *33*, 7130–7136.

30. D. Frenkel. *Physica A* **1999**, *263*, 26–38.

31. T. Zykova-Timan, J. Horbach, K. Binder. *J. Chem. Phys.* **2010**, *133*, 014705.

32. J. G. Kirkwood. *J. Chem. Phys.* **1939**, *7*, 919–925.

33. B. J. Alder, W. G. Hoover, D. A. Young. *J. Chem. Phys.* **1968**, *49*, 3688–3696.

34. W. G. Hoover, F. H. Ree. *J. Chem. Phys.* **1968**, *49*, 3609–3617.

35. P. N. Pusey, W. Vanmegen, P. Bartlett, B. J. Ackerson, J. G. Rarity, S. M. Underwood. *Phys. Rev. Lett.* **1989**, *63*, 2753–2756.

36. D. Frenkel, A. J. C. Ladd. *J. Chem. Phys.* **1984**, *81*, 3188–3193.

37. L. V. Woodcock. *Nature* **1997**, *385*, 141–143.

38. P. G. Bolhuis, D. Frenkel, S. C. Mau, D. A. Huse. *Nature* **1997**, *388*, 235–236.

39. S. Pronk, D. Frenkel. *J. Chem. Phys.* **1999**, *110*, 4589–4592.

40. A. V. Petukhov, D. Aarts, I. P. Dolbnya, E. H. A. de Hoog, K. Kassapidou, G. J. Vroege, W. Bras, H. N. W. Lekkerkerker. *Phys. Rev. Lett.* **2002**, *88*, 208301.

41. J. G. Berryman. *Phys. Rev. A* **1983**, *27*, 1053–1061.

42. M. Baus, J. L. Colot. *J. Phys. C: Solid State Phys.* **1986**, *19*, L135–L139.

43. G. D. Scott, D. M. Kilgour. *J. Phys. D: Appl. Phys.* **1969**, *2*, 863–866.

44. P. N. Pusey, W. Vanmegen. *Phys. Rev. Lett.* **1987**, *59*, 2083–2086.

45. L. Cipelletti, L. Ramos. *J. Phys.: Condens. Matter* **2005**, *17*, R253–R285.

46. Y. Levin. *Rep. Prog. Phys.* **2002**, *65*, 1577–1632.

47. D. M. Herlach, T. Palberg, I. Klassen, S. Klein, R. Koboldl. *J. Chem. Phys.* **2016**, *145*, 211703.

48. M. O. Robbins, K. Kremer, G. S. Grest. *J. Chem. Phys.* **1988**, *88*, 3286–3312.

49. A. P. Hynninen, M. Dijkstra. *Phys. Rev. E* **2003**, *68*, 021407.

50. E. B. Sirota, H. D. Ouyang, S. K. Sinha, P. M. Chaikin, J. D. Axe, Y. Fujii. *Phys. Rev. Lett.* **1989**, *62*, 1524–1527.

51. Y. Monovoukas, A. P. Gast. *J. Colloid Interface Sci.* **1989**, *128*, 533–548.

52. P. A. Rundquist, P. Photinos, S. Jagannathan, S. A. Asher. *J. Chem. Phys.* **1989**, *91*, 4932–4941.

53. T. Okubo. *Colloid. Polym. Sci.* **1992**, *270*, 1018–1026.

54. T. P. Lodge, B. Pudil, K. J. Hanley. *Macromolecules* **2002**, *35*, 4707–4717.

55. G. A. McConnell, A. P. Gast, J. S. Huang, S. D. Smith. *Phys. Rev. Lett.* **1993**, *71*, 2102–2105.

56. M. Watzlawek, C. N. Likos, H. Lowen. *Phys. Rev. Lett.* **1999**, *82*, 5289–5292.

57. E. E. Dormidontova, T. P. Lodge. *Macromolecules* **2001**, *34*, 9143–9155.

58. I. W. Hamley, J. A. Pople, O. Diat. *Colloid Polym. Sci.* **1998**, *276*, 446–450.

59. I. W. Hamley, C. Daniel, W. Mingvanish, S. M. Mai, C. Booth, L. Messe, A. J. Ryan. *Langmuir* **2000**, *16*, 2508–2514.

60. M. Laurati, J. Stellbrink, R. Lund, L. Willner, D. Richter, E. Zaccarelli. *Phys. Rev. Lett.* **2005**, *94*, 195504.

61. K. Matyjaszewski. *Macromolecules* **2012**, *45*, 4015–4039.

62. M. Ouchi, T. Terashima, M. Sawamoto. *Chem. Rev.* **2009**, *109*, 4963–5050.

63. E. Rizzardo, D. H. Solomon. *Aust. J. Chem.* **2012**, *65*, 945–969.

64. G. Moad, E. Rizzardo, S. H. Thang. *Aust. J. Chem.* **2012**, *65*, 985–1076.

65. S. Yamago. *Chem. Rev.* **2009**, *109*, 5051–5068.

66. T. Fukuda, A. Goto, K. Ohno. *Macromol. Rapid Comm.* **2000**, *21*, 151–165.

67. C. Boyer, N. A. Corrigan, K. Jung, D. Nguyen, T. K. Nguyen, N. N. M. Adnan, S. Oliver, S. Shanmugam, J. Yeow. *Chem. Rev.* **2016**, *116*, 1803–1949.

68. Y. Tsujii, K. Ohno, S. Yamamoto, A. Goto, T. Fukuda. *Adv. Polym. Sci.* **2006**, *197*, 1–45.

69. M. Kobayashi, Y. Terayama, M. Kikuchi, A. Takahara. *Soft Matter* **2013**, *9*, 5138–5148.

70. R. Barbey, L. Lavanant, D. Paripovic, N. Schuwer, C. Sugnaux, S. Tugulu, H. A. Klok. *Chem. Rev.* **2009**, *109*, 5437–5527.

71. D. Dukes, Y. Li, S. Lewis, B. Benicewicz, L. Schadler, S. K. Kumar. *Macromolecules* **2010**, *43*, 1564–1570.

72. M. Ejaz, S. Yamamoto, K. Ohno, Y. Tsujii, T. Fukuda. *Macromolecules* **1998**, *31*, 5934–5936.

73. S. Yamamoto, M. Ejaz, Y. Tsujii, M. Matsumoto, T. Fukuda. *Macromolecules* **2000**, *33*, 5602–5607.

74. S. Yamamoto, M. Ejaz, Y. Tsujii, T. Fukuda. *Macromolecules* **2000**, *33*, 5608–5612.

75. A. Nomura, K. Ohno, T. Fukuda, T. Sato, Y. Tsujii. *Polym. Chem.* **2012**, *3*, 148–153.

76. C. Yoshikawa, A. Goto, Y. Tsujii, T. Fukuda, T. Kimura, K. Yamamoto, A. Kishida. *Macromolecules*

2006, *39*, 2284–2290.

77. C. Yoshikawa, A. Goto, Y. Tsujii, N. Ishizuka, K. Nakanishi, T. Fukuda. *J. Polym. Sci., Part A: Polym. Chem.* **2007**, *45*, 4795–4803.

78. M. Daoud, J. P. Cotton. *J. Phys. (Paris)* **1982**, *43*, 531–538.

79. E. B. Zhulina, T. M. Birshtein, O. V. Borisov. *Eur. Phys. J. E* **2006**, *20*, 243–256.

80. J. Kalb, D. Dukes, S. K. Kumar, R. S. Hoy, G. S. Grest. *Soft Matter* **2011**, *7*, 1418–1425.

81. U. Gasser. *J. Phys.: Condens. Matter* **2009**, *21*, 203101.

82. T. Palberg. *J. Phys.: Condens. Matter* **2014**, *26*, 333101.

83. P. Tan, N. Xu, L. Xu. *Nat. Phys.* **2014**, *10*, 73–79.

84. P. R. ten Wolde, D. Frenkel. *Science* **1997**, *277*, 1975–1978.

85. T. Kawasaki, H. Tanaka. *Proc. Natl Acad. Sci. USA* **2010**, *107*, 14036–14041.

86. J. Russo, H. Tanaka. *Sci. Rep.* **2012**, *2*, 505.

87. T. B. Martin, K. I. S. Mongcopa, R. Ashkar, P. Butler, R. Krishnamoorti, A. Jayaraman. *J. Amer. Chem. Soc.* **2015**, *137*, 10624–10631.

88. H. Koerner, L. F. Drummy, B. Benicewicz, Y. Li, R. A. Vaia. *ACS Macro Lett.* **2013**, *2*, 670–676.

89. J. S. Meth, S. G. Zane, C. Z. Chi, J. D. Londono, B. A. Wood, P. Cotts, M. Keating, W. Guise, S. Weigand. *Macromolecules* **2011**, *44*, 8301–8313.

90. V. Goel, J. Pietrasik, H. C. Dong, J. Sharma, K. Matyjaszewski, R. Krishnamoorti. *Macromolecules* **2011**, *44*, 8129–8135.

91. G. A. Williams, R. Ishige, O. R. Cromwell, J. Chung, A. Takahara, Z. B. Guan. *Adv. Mater.* **2015**, *27*, 3934–3941.

92. R. Ishige, G. A. Williams, Y. Higaki, N. Ohta, M. Sato, A. Takahara, Z. B. Guan. *Iucrj* **2016**, *3*, 211–218.

93. J. K. Percus, G. J. Yevick. *Phys. Rev.* **1958**, *110*, 1–13.

94. M. S. Wertheim. *Phys. Rev. Lett.* **1963**, *10*, 321–323.

95. J. L. Lebowitz. *Phys. Rev.* **1964**, *133*, A895–A899.

96. T. Morinaga, K. Ohno, Y. Tsujii, T. Fukuda. *Macromolecules* **2008**, *41*, 3620–3626.

97. T. Sato, T. Morinaga, S. Marukane, T. Narutomi, T. Igarashi, Y. Kawano, K. Ohno, T. Fukuda, Y. Tsujii. *Adv. Mater.* **2011**, *23*, 4868–4872.

98. T. Morinaga, S. Honma, T. Ishizuka, T. Kamijo, T. Sato, Y. Tsujii. *Polymers* **2016**, *8*, 146.

Chapter 2

USAXS analysis of concentration-dependent self-assembling of polymer-brush-modified nanoparticles in ionic liquid: [I] concentrated-brush regime

2-1. Introduction

Well-defined and low-polydispersity polymers can be densely grown up on various solid surfaces by living radical polymerization[1-7] (LRP; also called controlled reversible-deactivation radical polymerization as per the IUPAC recommendation). The graft density in such cases is more than one order of magnitude higher than that of a typical "semi-dilute" polymer brush (SDPB), going deep into the "concentrated"-brush regime.[8-11] Graft chains of such a concentrated polymer brush (CPB) in a good solvent are highly extended, almost to their full lengths, because of the exceptionally high osmotic pressure of the brush.[8,12-14] Because of such a highly stretched conformation, CPB in a good solvent exhibits characteristics such as high resistance against compression, very less mutual interpenetration that gives rise to very high lubrication with an extremely low friction coefficient ($\mu \sim 10^{-4}$),[8,9,15] and definite size exclusion with a very low threshold of molecular weight that gives good biocompatibility in an aqueous system.[8,16,17]

Such highly repulsive and lubricating properties lead to a good dispersion of CPB-modified silica nanoparticles (PSiPs), thereby forming stable suspensions and colloidal crystals above a certain concentration. The obtained colloid crystals of PSiPs can be distinguished as a "semi-soft" type[18-23] in contrast to the previously reported "hard"[24-29] and "soft"[30-38] types which are formed by a hard-sphere and electrostatic interactions, respectively. Note that the above-mentioned semi-soft colloidal crystals can be formed even in an ionic liquid in which the electrostatic interactions are shielded.[39] Different types of higher-order structures can be expected by varying the interparticle potential and particle concentration. For examples, there are typically three types of closed packing pattern: face-centered

cubic (fcc; ABC-stacking), hexagonal close packing (hcp; ABA-stacking), and random-hexagonal close packing (rhcp; random stacking). The difference lies in the way of stacking of the planes (A, B, or C), in which the colloids are hexagonally packed. Previous work by our group reported that PSiPs self-assemble in the rhcp structure in an organic solvent at the liquid/crystal-threshold concentration,[20] while they assemble in the fcc structure in an ionic liquid at a higher particle concentration.[40,41] Thermodynamic equilibrium was confirmed for the former but not for the latter. The latter focused on the application of such a self-assembled structure as a novel pseudo-solid electrolyte to a bipolar-type lithium-ion rechargeable battery. Therefore, a detailed and systematic study of the PSiP self-assembling process in an ionic liquid as a function of particle concentration should be carried out not only to further understand the basics of colloid science but also to develop highly functionalized devices.

This paper discusses the concentration-dependent self-assembling of PSiP based on the above discussion. However, it is highly challenging to precisely analyze a higher-order structure of PSiP as a function of particle concentration. Among the various methods available for structural analyses, small-angle X-ray scattering (SAXS) method is one of the most powerful techniques, indeed, various researches on the structures of materials containing nanoparticles with polymers using SAXS were reported.[42-45] In this study, we carried out measurements at ultra-small angles, because we used over submicron-scale materials. Recently, ultra-small-angle X-ray scattering (USAXS) was used to analyze the higher-order structure of polymer-brush-modified nanoparticles in a stretched polymer film.[46,47] These results demonstrated that the USAXS method can be used effectively for a colloidal system. In this study, we systematically analyzed higher-order structures of CPB-modified nanoparticles in an ionic liquid as a function of particle concentration using the USAXS method.

Various static and dynamic aspects of the colloid crystals including phase behavior, crystal nucleation/growth process, and their control have been discussed over the last 50 years not only for fundamental understanding but also for a wide range of applications.[25,48,49] Among others, a so-called "hard sphere (HS)" system showing the Kirkwood–Alder transition,[50,51] i.e., phase transition from liquid to crystal, as well as an amorphous or glass phase with higher concentrations.[25,52] It has been most extensively studied on theories, simulations, and experiments and is still of great importance. The HS-model system most experimentally studied was polymeric colloids (nonswelling-bulk or micro-gel polymeric cores) sterically stabilized and dispersed in non-aqueous solvents, because the electrostatic interaction forming a soft shell must be shielded. For steric stabilization, a lyophilic polymer was usually adsorbed on the core particle. The problem in this system is the compression or desorption of polymeric stabilizer at a high particle concentration. As above-mentioned, our studied system is considered to be a good HS-model because of a sufficiently thin but completely repulsive CPB layer covalently end-grafted on a hard, nonswelling silica core as well as little electrostatic interaction (well shielded) in an ionic liquid. It is typically well-known that the Daoud-Cotton model describes the transition from CPB to SDPB as polymer chains end-grafted to spherical and cylindrical surfaces become longer,[19,53-55] which indicates that a shorter length of polymer brush of PSiP should be required for this work.

2-2. Experimental section

2-2-1. Materials

N,*N*-Diethyl-*N*-(2-methacryloylethyl)-*N*-methylammonium bis(trifluoromethylsulfonyl) imide (DEMM-TFSI) was obtained from Toyo Gosei Co., Ltd., Tokyo, Japan. Silica particle (SiP) (SEAHOSTER KE-E10, 20 wt% suspension of SiP in ethylene glycol) was kindly donated by Nippon Shokubai Co., Ltd., Osaka, Japan. Ethyl 2-bromoisobutyrate (2-(EiB)Br; Tokyo Chemical Industry Co., Ltd, Japan, 98%), *N*,*N*-diethyl-*N*-(2-methoxyethyl) ammonium bis(trifluoromethane sulfonyl) imide (DEME-TFSI; Kanto Chemical Co., Inc., Japan), 2,2′-bipyridine (Nacalai Tesque Inc., Japan, 97%), copper(II) dichloride (Cu(II)Cl_2; Nacalai, 98%), sodium nitrate ($NaNO_3$; Wako, 99.0%), acetonitrile (Kanto Chemical, 99.5%), and 28% aqueous ammonia (Nacalai) were used as received. Copper(I) chloride (Cu(I)Cl; Wako Pure Chemical Industries, Ltd., Japan, 99.9%) was washed with glacial acetic acid (CH_3CO_2H; Wako, 99.7%) to remove any soluble oxidized impurity, filtered, washed with ethanol

(Wako) and diethyl ether (Wako), and dried. An atom transfer radical polymerization (ATRP)-initiator-holding silane coupling agent, (2-bromo-2-methyl)propionyloxypropyltriethoxysilane (BPE), was synthesized as reported previously.[56] Water was purified by a Milli-Q system (Nihon Millipore Ltd., Tokyo, Japan) to a specific resistivity of ~18 MΩ cm. Poly(ethylene oxide) (PEO) standards were obtained from TOSOH Corporation, Japan.

2-2-2. Synthesis and characterization of polymer-brush-modified hybrid particles

PSiP was synthesized by surface-initiated ATRP, as reported previously.[40,41] In brief, SiP was surface-modified using a mixture of ethanol/water/ammonia containing BPE, and the surface-initiated ATRP of DEMM-TFSI was carried out in a solution of acetonitrile (300 g) containing initiator-fixed SiP (BPE-SiP; 10 g), DEMM-TFSI (150 g, 0.31 mol), 2-(EiB)Br (1.10 g, 5.68 mmol), Cu(I)Cl (0.450 g, 4.54 mmol), Cu(II)Cl_2 (0.153 g, 1.14 mmol), and 2,2′-bipyridine (1.95 g, 0.0125 mol). Here, 2-(EiB)Br was added as a nonfixed (free) initiator, not only to control the polymerization but also to produce a free (unbound) polymer, which was reasonably assumed to have the same molecular weight and distribution as a graft polymer. An aliquot of the polymerization solution was removed for NMR measurement to estimate monomer conversion using a JEOL/AL400 spectrometer (JEOL, Tokyo, Japan), and for gel permeation chromatography (GPC) measurement to determine the molecular weight and its distribution. GPC measurement was carried on a Shodex GPC-101 high-speed liquid chromatography system equipped with a multi-angle laser light-scattering (MALLS) detector (Wyatt Technology DAWN HELEOS, Santa Barbara, CA). Two SB-806M HQ (Shodex) columns were installed and calibrated by

Table 2-1. Characteristics of silica particle grafted with concentrated P(DEMM-TFSI) brush.

$M_{n,\,theo}$[a]	$M_{n,\,exp}$[b]	$M_{w,\,exp}$[b]	M_w/M_n[b]	A_g[c]	σ / chains nm^{-2} [c]	σ^*
24 300	27 800	29 900	1.08	0.17	0.19	42%

[a] Determined by NMR conversion. [b] Measured by GPC-MALLS. [c] Determined by TGA results.

PEO standards. The eluent comprised a solution of acetonitrile/water (50/50 by vol/vol) containing 0.1 M $NaNO_3$ and 0.25 M CH_3CO_2H. The obtained PSiP was purified by carrying out repeated cycles of redispersion/centrifugation in acetonitrile. To determine the graft density (σ) and the surface occupancy (σ^*), the weight of the grafted polymer in comparison to the SiP-core weight (A_g) was analyzed by thermogravimetry using the Shimadzu TGA-50 instrument (Shimadzu, Kyoto, Japan) under an argon atmosphere. Finally, the ATRP at 70 °C for 18.5 h was performed to obtain a well-defined PSiP at 98% conversion. Its molecular characteristics are summarized in Table 2-1; the M_n and M_w/M_n values were determined by simultaneously carrying out MALLS for the produced free polymer. Note that the M_n value was very close to the theoretical value estimated from the conversion assuming complete initiation, and that the M_w/M_n ratio was nearly equal to that estimated using PEO calibration, suggesting successful evaluation as the absolute value of the molecular weight and its distribution.

2-2-3. Preparation of PSiP/IL composites

In this study, DEME-TFSI was used as an IL, which is a good solvent for poly(DEMM-TFSI) (P(DEMM-TFSI)). A suspension of PSiP in acetonitrile was mixed with DEME-TFSI in different compositions; to this solution, acetonitrile was added to adjust its concentration to 60 wt% in the solution. Then, the prepared solutions were cast by slowly evaporating acetonitrile for 12 h, followed by drying it in a vacuum oven at 90 °C for 24 h to obtain PSiP/IL composites in different compositions. The weight fractions of PSiP in the composite (f_{PSiP}) were 22, 24, 26, 28, 30, 36, 44, 50, 55, 60, 68, and 75 by wt%, and they were denoted as P-22, P-24, P-26, P-28, P-30, P-36, P-44, P-50, P-55, P-60, P-68, and P-75, respectively. Samples P-50 to P-75 were prepared on a Teflon sheet (YODOFLON, Yodogawa Hu-Tech Co. Ltd.), and others were prepared in the capillary with an outer-diameter of 2 or 3 mm (Hilgenberg GmbH, Malsfeld, Germany) because of they were liquid. For the capillary, a gentle flow of argon was applied.

2-2-4. Ultra-small-angle/small-angle X-ray scattering (USAXS) measurements

Ultra-small-angle X-ray scattering (USAXS) measurements were performed at the beamlines, BL19B2 and BL03XU, in SPring-8 (Harima, Hyogo, Japan). The USAXS profiles were obtained on a two-dimensional hybrid pixel array detector, PILATUS 2M with 3 × 6 modules (DECTRIS Ltd.) and 1475 × 1679 pixels of 172 μm pixel size at BL19B2, on a complementary metal oxide semiconductor image sensor (CMOS) camera (C11440-22C; Hamamatsu Photonics, Shizuoka, Japan) coupled to an X-ray image intensifier system (V7735P; Hamamatsu Photonics) consisting of 2048 × 2048 pixels with a 43.1 μm pixel size at BL40B2, and on an imaging plate (IP; Rigaku R-AXIS VII) with 3000 × 3000 pixels of a 100 μm pixel size and PILATUS 1M (DECTRIS Ltd.) with 981 × 1043 pixels of 172 μm pixel size at BL03XU. The X-ray beam size at the sample position (horizontal × vertical) was 300 μm × 100 μm (BL19B2), 600 μm × 600 μm (BL40B2), and 112 μm × 100 μm (BL03XU). The X-ray wavelengths (λ) were 0.0689 nm (BL19B2), 0.19 nm (BL40B2), 0.15 nm (BL03XU using IP), and 0.20 nm (BL03XU using PILATUS 1M). The sample-to-detector distances were 42629 mm, 41741 mm, or 41546 mm (BL19B2), 4325 mm (BL40B2), 7870 mm (BL03XU using IP), and 8003 mm (BL03XU using PILATUS 1M). The scattered intensities are expressed as a function of the scattering vector, $q = (4\pi \sin\theta)/\lambda$, where 2θ is the scattering angle relative to the incident beam. The q value was calibrated using a collagen fiber extracted from a chicken leg.

2-2-5. SEM observation

Field-emission scanning electron microscopy (FE-SEM) observation was carried out on a JSM-6700F instrument (JEOL Ltd., Japan). In order to observe the cross-sectional surface, the freeze-fractured sample was mounted on a brass stub and sputter-coated with gold/palladium to minimize sample charging using a Hitachi ion sputter E-1010.

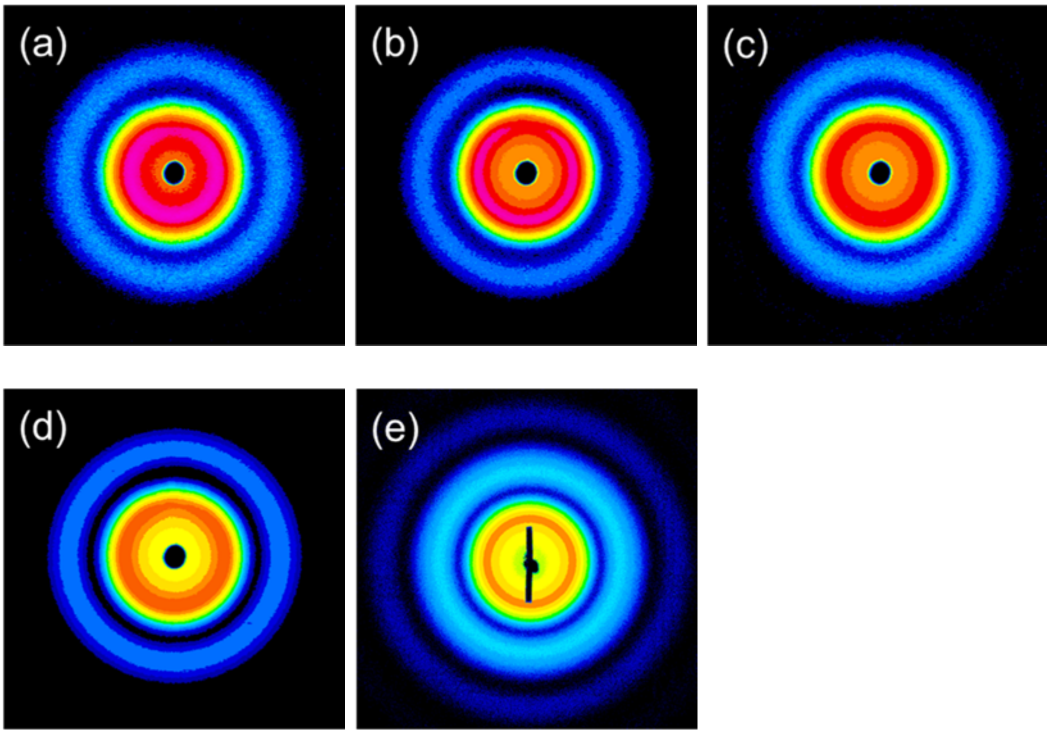

Figure 2-1. 2D USAXS images of (a) P-22, (b) P-30, (c) P-36, (d) P-44, and (e) P-50. Images (a)–(d) were obtained at BL03XU using IP as the detector, and other image (e) was obtained at BL19B2 in SPring-8

2-3. Results and Discussion

Using a simple tube-inverting method, the samples at f_{PSiP} below 50 wt% (P-22 to P-50) and above 55 wt% (P-55 to P-75) were found to be liquid and solid, respectively. Figure 2-1 shows the 2D USAXS images of samples P-22, P-30, P-36, P-44, and P-50. No diffraction pattern was observed, suggesting little higher-order structures. In order to obtain the information on the core/shell structure of these sample s and hence the effective particle size and its distribution as the HS-model system, 2D USAXS images were circularly averaged in intensity, and the thus obtained 1D USAXS intensity profiles were analyzed as follows.

The scattering intensity $I(q)$ of the dispersed particles can be obtained using the following relation:[57]

$$I(q) = Kn\Delta\rho_{\mathrm{e}}{}^{2}[\langle F(q)^{2}\rangle + \langle F(q)\rangle^{2}(S(q)-1)] \qquad \text{(2-1)}$$

where K is a constant that is a function of the type of radiation used and the sample properties, n is the number density of scattering units (core particles in this case), $\Delta\rho_{\mathrm{e}}$ is the difference in the scattering length density between a particle and a matrix, and $F(q)$ and $S(q)$ are the form factor and structure factor of particles of radius r, respectively. The brackets $\langle\,\rangle$ refer to an ensemble or time average with respect to the scattering volume. Here, $F(q)$, its average $\langle F(q)\rangle$, and its mean square $\langle F(q)^2\rangle$ are given by[58]

$$F(q) = \frac{4\pi r^3[\sin(qr) - qr\cos(qr)]}{(qr)^3} \tag{2-2}$$

$$\langle F(q)\rangle = \int_0^\infty F(q)D(r)\,dr \tag{2-3}$$

$$\langle F(q)^2\rangle = \int_0^\infty F(q)^2 D(r)\,dr \tag{2-4}$$

where $D(r)$ is the Gaussian distribution function defined by the average radius r_0 and its standard deviation a of the scattering particle. $D(r)$ is obtained by

$$D(r) = \frac{1}{\sqrt{2\pi a^2}}\exp\left[-\frac{(r-r_0)^2}{2a^2}\right] \tag{2-5}$$

$S(q)$ was estimated for the samples at a relatively low concentration using the Percus–Yevick (PY) approximation,[59-61] one of the most widely used classical approximations for a liquid state.

$$S(q) = \frac{1}{1 - nC(q)} \tag{2-6}$$

$$C(q) = -4\pi\int_0^{D_{\mathrm{PY}}}\left[\alpha + \beta\left(\frac{r}{D_{\mathrm{PY}}}\right) + \gamma\left(\frac{r}{D_{\mathrm{PY}}}\right)^3\right]\frac{\sin(qr)}{qr}r^2\mathrm{d}r \tag{2-7}$$

where D_{PY} is the diameter of the hard-sphere assumed by the PY model, and parameters α, β, and γ are given as follows:

$$\alpha = \frac{(1+2\varphi_{\mathrm{PY}})^2}{(1-\varphi_{\mathrm{PY}})^4} \tag{2-8}$$

$$\beta = -\frac{6\varphi_{\mathrm{PY}}(1+\varphi_{\mathrm{PY}}/2)^2}{(1-\varphi_{\mathrm{PY}})^4} \tag{2-9}$$

$$\gamma = \frac{\varphi_{\mathrm{PY}}(1+2\varphi_{\mathrm{PY}})^2}{2(1-\varphi_{\mathrm{PY}})^4} \tag{2-10}$$

Here, φ_{PY} is the volume fraction of the hard-sphere and is defined as follows:

$$\varphi_{\mathrm{PY}} = n\frac{\pi {D_{PY}}^{3}}{6} \qquad (2\text{-}11)$$

These theoretical equations were used for analyzing the 1D USAXS intensity profiles of the samples (P-22 to P-30) at sufficiently low concentrations by considering the PY approximation.[59] Figure 2-2(a) shows the experimental and theoretical data of 1D USAXS intensity profiles of these samples along with BPE-SiP. Close resemblance between the chemical structures of CPB and IL makes it easier to fit the USAXS profile, i.e., (i) $\Delta\rho_{\mathrm{e}}$ can be estimated using the scattering length density of silica and IL, (ii) the scattering unit was reasonably assumed to be the silica core even for PSiP, and hence, the r_0 and a values in $F(q)$ correspond to those of the core as the common parameters not only for BPE-SiP but also for PSiP, and (iii) the swollen layer of CPB on the core is only reflected in $S(q)$ as the D_{PY} value.

BPE-SiP particles dispersed in acetonitrile at very low concentration (<1 wt%) were assumed to have $S(q) = 1$.[57,62] The data fitting shown in Figure 2-2(a) successfully estimated the r_0 and a values

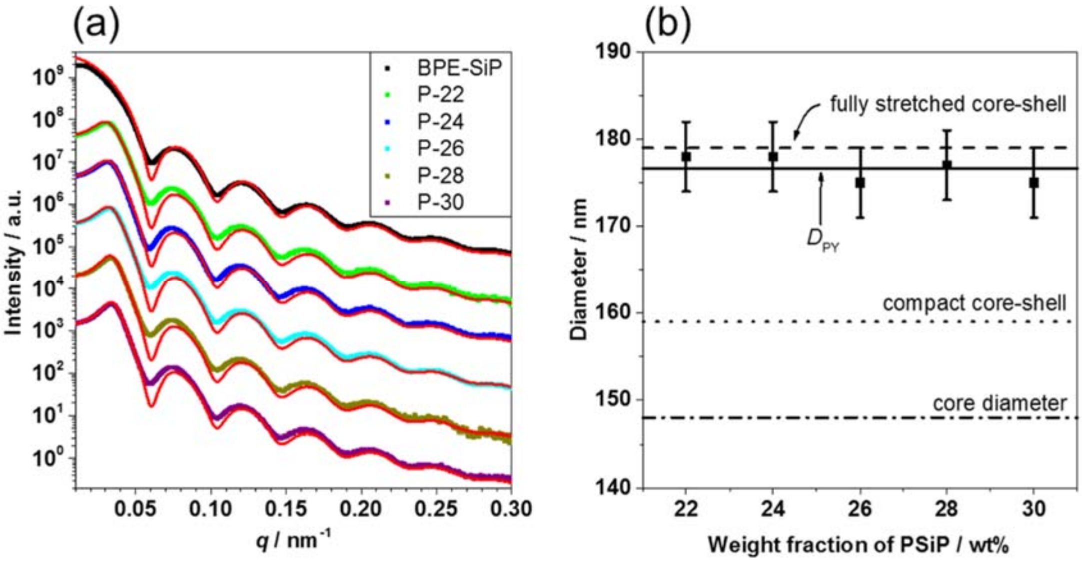

Figure 2-2. (a) 1D USAXS intensity profiles of the suspension of BPE-SiP, P-22, P-24, P-26, P-28, and P-30. These USAXS profiles were obtained using PILATUS 1M and IP as the detector at BL03XU as well as using a CMOS camera at BL40B2 in SPring-8. The solid red line is the theoretical profile using Percus–Yevick model. (b) Plot of D_{PY} of PSiP estimated using Percus–Yevick model as a function of PSiP concentration (f_{PSiP}). The average value of D_{PY} is given as 177 nm (solid line). For the fully stretched and compact core-shell models, see the accompanying text.

of the SiP core to be 74 nm and 4 nm, respectively, confirming a narrow distribution of the core size as expected.

To analyze the data for the PSiP samples shown in Figure 2-2(a), the particle number density n was estimated by:

$$n = \frac{f_0/w_0}{f_0/\rho_0 + (1 - f_0)/\rho_{\mathrm{IL}}} \tag{2-12}$$

$$f_0 = \frac{f_{\mathrm{PSiP}}}{1 + A_{\mathrm{g}}} \tag{2-13}$$

$$w_0 = \frac{4\pi\rho_0 {r_0}^3}{3} \tag{2-14}$$

where f_0 and w_0 are the weight fraction of the silica-core part and the weight of one core particle, respectively; ρ_0 and ρ_{IL} are the bulk densities of silica core (2.0) and IL (1.42), respectively. For these equations, the density of P(DEMM-TFSI), and hence the graft layer in bulk, was reasonably assumed to be equal to that of IL because of the similar chemical structure. Finally, the D_{PY} value was estimated only as a fitting parameter for the USAXS profile of the PSiP samples and plotted as a function of f_{PSiP} (Figure 2-2(b)). The estimated D_{PY} was independent of f_{PSiP} in this range, giving an average value of 177 nm. Meth et al. reported that the effective diameter of charged particles in the dispersion using theoretical model about SAXS,[44] however, the effective volume decreased with the increase of the particle concentration, which was considered to derive from the effect of charged double layers. On the other hand, an almost constant value of D_{PY} in PSiP system was obtained, which suggests the validity of this analysis using the PY model. The PY model assumes a "hard" particle, which is not allowed to penetrate each other, and hence, D_{PY} can be regarded as an "effective" size against compression caused by the Brownian motion. Therefore, it is interesting to compare the thus obtained D_{PY} values with the values obtained using two different models of the CPB-shell layer. One is the "fully stretched core-shell model,"[18,63] which consists of a SiP core and P(DEMM-TFSI) chains radially stretched in all-trans conformation, and hence, diameter D_{full} is described as follows:

$$D_{\mathrm{full}} = 2(r_0 + l_0 x_{\mathrm{w}}) \tag{2-15}$$

where l_0 is the chain contour length per monomer unit (l_0 = 0.25 nm for vinyl polymers), and x_w is the weight-average degree of polymerization of CPB. To estimate the outermost shell, the weight-average value rather than the number-average value in the chain length was applied, since longer chains show more participation to form the outermost surface. Thus, D_{full} was calculated as 179 nm for the used sample. The second model is the "compact core-shell model,"[18,63] which consists of a SiP core and a P(DEMM-TFSI) shell in bulk. The diameter of a PSiP particle with a compact core-shell model D_c was calculated as 159 nm using the following equation:

$$D_{\mathrm{c}} = 2(r_0 + \sigma^* l_0 x_{\mathrm{n}}) \tag{2-16}$$

where x_n is the number-average degree of polymerization of CPB. As shown in Figure 2-2(b), the CPB layer of P(DEMM-TFSI) was demonstrated to be highly swollen, comparable to full stretching, as was expected for a good solvent. The above discussion also suggests that the CPB of swollen P(DEMM-TFSI) in IL was so highly repulsive that the PY model could be used to evaluate the swollen structure. Incidentally, the USAXS intensity profiles of P-36 and P-44 with PY model fitting were shown in Figure 2-3. It looks well-fitted, however, the value of D_{PY} was estimated shorter than that of lower concentration

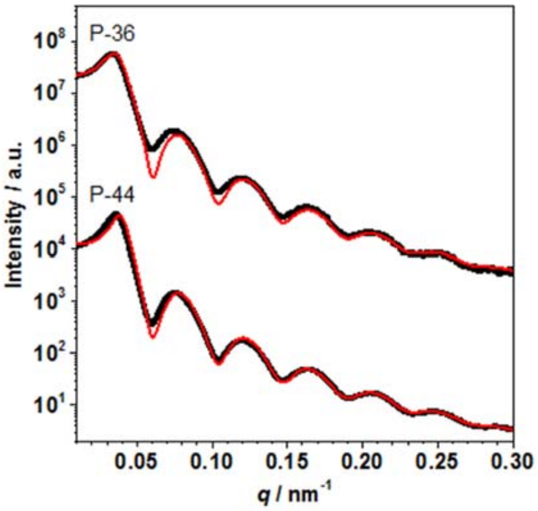

Figure 2-3. 1D USAXS intensity profiles of P-36 and P-44. These profiles were measured using IP as the detector at BL03XU in SPring-8. The solid red line is the theoretical profile using Percus–Yevick model. The value of D_{PY} is given as 166 nm for P-36 and 161 nm for P-44.

samples (P-22 to P-30). It is possible to say that PY model fitting is not suitable for P-36 and P-44 because of too much higher concentration for PY approximation, or CPBs on SiP start shrinking for the order-disorder transition.

Then, we focus on the samples at higher f_{PSiP}. Figure 2-4(a) and (b) show the 2D USAXS image and 1D intensity profile of P-60, respectively. Some diffraction peaks were clearly observed, suggesting the self-assembling of PSiP in IL, i.e., the formation of a colloidal crystal. Here, the crystal structure of fcc, hcp, and rhcp, as well as body-centered cubic (bcc), were considered as a candidate of the formed

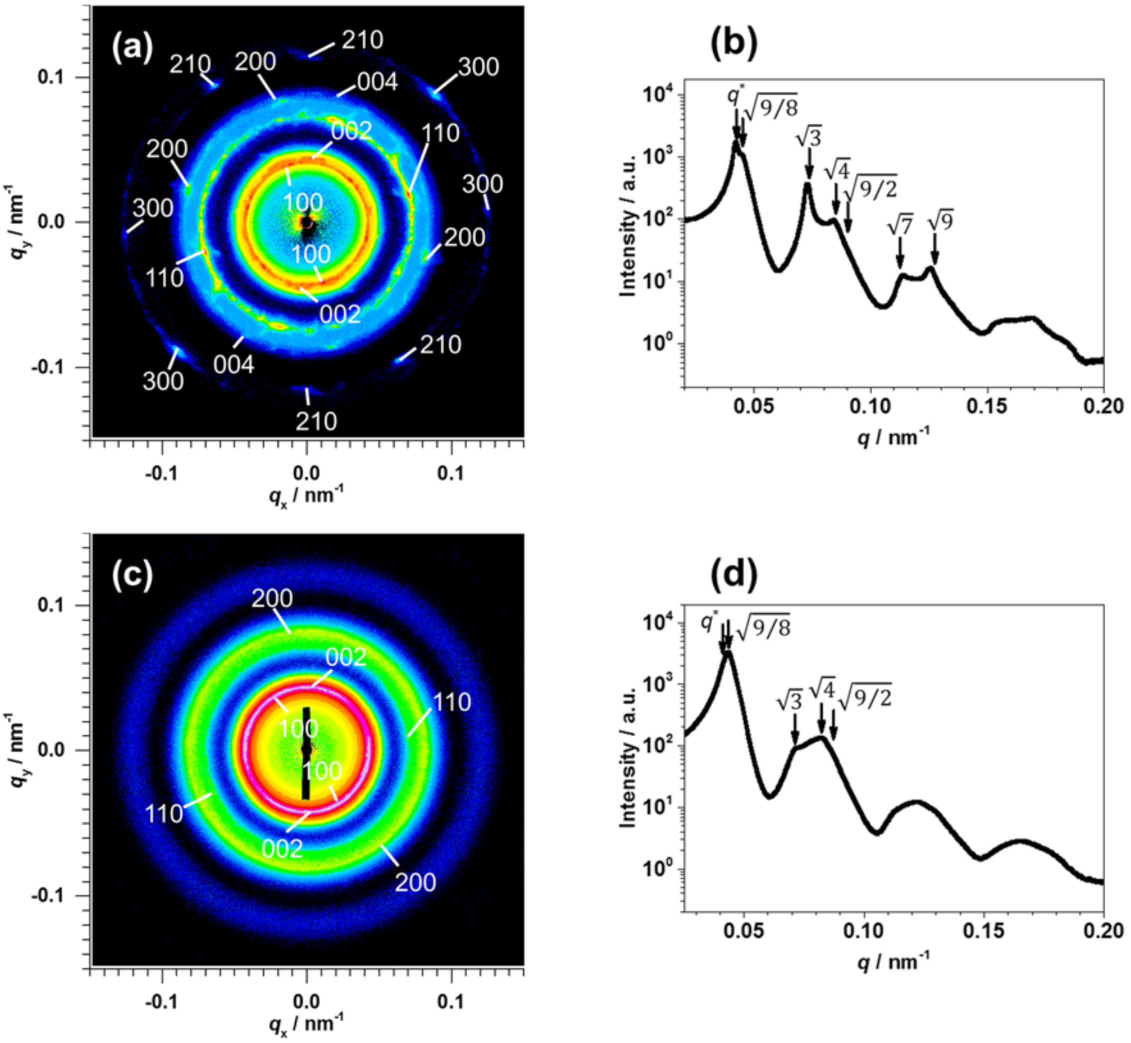

Figure 2-4. (a)(c) 2D USAXS image of P-60 and P-55 obtained at BL19B2 in SPring-8, respectively. The assigned *hkl* indices of the 3D hexagonal lattice are given in the image. (b)(d) 1D USAXS intensity profile of P-60 and P-55, respectively.

higher-order structure. The diffraction peaks were observed at q values of the q/q^*ratio of approximately $1:\sqrt{(9/8)}:\sqrt{3}:\sqrt{4}:\sqrt{(9/2)}:\sqrt{7}:\sqrt{9}$ (Figure 2-4(b)). This was reasonably ascribed to the hcp-type lattice, but not to the bcc or the fcc. These diffraction peaks were well fitted as those of *hk*0 or 00*l* in the description of the Miller index for the *hexagonal system* (hcp-type lattice). The diffraction patterns of *hkl* (except *hk*0 or 00*l*) that should appear for the hcp were not observed (Figure 2-4(a)). Therefore, the crystal structure of P-60 was determined as rhcp. Figure 2-4(c) and (d) show the 2D USAXS image and 1D intensity profile of P-55, respectively. The diffraction patterns and peaks of P-55 appeared, which were weaker than those of P-60. Based on the structure analysis for P-60, it is reasonable that the diffraction patterns of P-55 were fitted as those of those of *hk*0 or 00*l* in the description of the Miller index for the hcp-type lattice as well. In addition, the diffraction peaks of P-55 were observed at q values of the q/q^*ratio of approximately $1:\sqrt{(9/8)}:\sqrt{3}:\sqrt{4}:\sqrt{(9/2)}$ (Figure 2-4(d)). Therefore, the crystal structure of P-55 was also determined as rhcp.

Figure 2-5 shows the 2D USAXS images from the edge and through-views of P-68 and P-75. High-quality diffraction patterns were obtained, especially for the edge-view data. Possible diffraction peaks are indicated by circles in the figure, assuming the fcc with the (111) lattice plane parallel to the cast substrate.[64] Good correlation between them was confirmed. One of characteristic diffraction patterns for the fcc is from (200) lattice plane, which was observed clearly in both USAXS images from the edge view. In addition, some diffraction peaks in the through-view data were assigned to the fcc, as shown along with the Miller index in the figure. Finally, we reasonably determined the fcc to be the main structure at $f_{\mathrm{PSiP}} = 68$ and 75 wt%. Indeed, the cross-sectional FE-SEM image of P-75 as shown in Figure 2-6 revealed that PSiPs were regularly stacked as fcc. Note that the domain size of the colloidal crystal for P-75 was over several-hundred micrometers because the diffraction points unambiguously appeared not only in the edge view but also in the through-view.

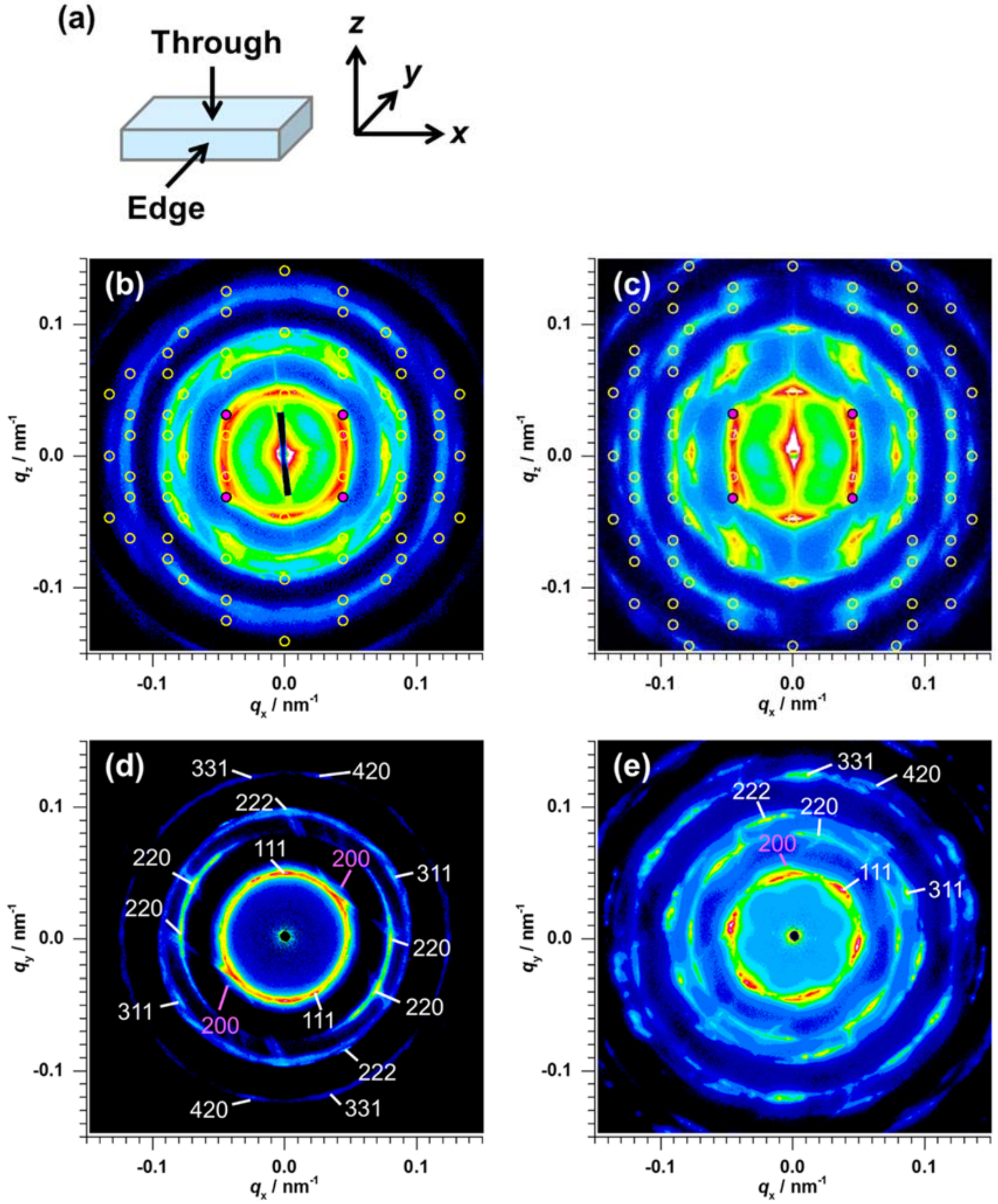

Figure 2-5. (a) A schematic illustration of the direction of USAXS measurement for P-68 and P-75. The *z*-axis line of this image was perpendicular to the cast substrate. (b)(c)(d)(e) 2D USAXS images in the edge-view of (b) P-68 and (c) P-75, and in the through-view of (d) P-68 and (e) P-75. All images were obtained at BL19B2 in SPring-8. The yellow circles in the edge-view images indicate the prediction of diffraction patterns of fcc-type lattice, while pink circles mean the diffraction patterns of the (200) plane of the fcc.

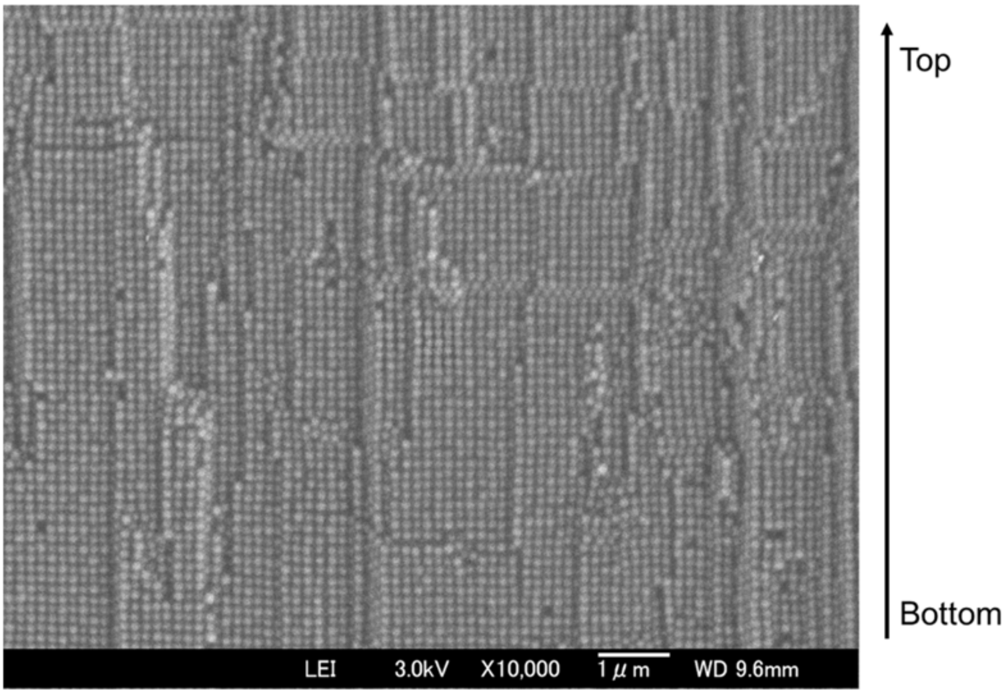

Figure 2-6. A cross-sectional FE-SEM image of P-75. The image was obtained with some tilts to observe the (100) plane of fcc-type lattice. The tetragonal packed spheres of the image correspond to the (100) plane.

During the formation of these higher-order structures, any exudation of IL, i.e., any macroscopic phase separation of the colloidal crystal domain and IL, was not observed. In addition, the center-to-center distance D_{dis} between neighboring particles was estimated from the USAXS data ($D_{\mathrm{dis,diff}}$) and the feed particle concentration ($D_{\mathrm{dis.feed}}$) for the close-packed structures according to the following equations:

$$D_{\mathrm{dis,diff}} = \begin{cases} \dfrac{4\sqrt{3}\pi}{3q_{100}} = \dfrac{4\pi}{q_{110}} \quad \text{(rhcp)} \\ \dfrac{\sqrt{6}\pi}{q_{111}} = \dfrac{4\pi}{q_{220}} \quad \text{(fcc)} \end{cases} \tag{2-17}$$

$$D_{\mathrm{dis,feed}} = 2^{1/6} n^{-1/3} \tag{2-18}$$

In eq (2-17), q_{hkl} is the peak value of the diffraction from the (*hkl*) plane. $D_{\mathrm{dis,diff}}$ in Table 2-2 was determined using the averaged value of q_{110} for rhcp or q_{220} for fcc and was confirmed to be equal in an experimental error with that obtained from q_{100} or q_{111}, respectively. Table 2-2 suggests that $D_{\mathrm{dis,diff}}$ was approximately equal to $D_{\mathrm{dis.feed}}$. These results indicate that a homogenous composite of PSiP and IL was

Table 2-2. Structure characteristics of P-55, P-60, P-68, and P-75.

Sample ID	Structure	$D_{\mathrm{dis,diff}}$[a]	$D_{\mathrm{dis,feed}}$[b]
P-55	rhcp	176 nm	184 nm
P-60	rhcp	172 nm	178 nm
P-68	fcc	164 nm	169 nm
P-75	fcc	160 nm	163 nm

[a,b] Calculated using eqs (2-17) and (2-18), respectively.

successfully prepared and that the colloidal crystal was characterized as the main component, based on the USAXS data.

As already discussed, the higher-order structure of PSiP in IL changed from liquid to solid and from disorder to the rhcp and finally to the fcc as increasing particle concentration. In general, the structure of colloidal systems with higher particle concentration is mainly glass.[25,52] However, in our work, the higher-order structures of PSiP in IL don't follow these behaviors, which is the unique point because of brush-modified particles in CPB in regime.

Because the process of self-assembling the PSiP with a fully repulsive and low-frictional surface involves slow evaporation of the solvent, these structures and states can be understood in quasi-equilibrium. In fact, the PSiP dispersed in a solvent was previously reported to form a colloidal crystal when it was left to stand for a quite short duration after mixing.[18] Thus, it would be interesting to compare the above-mentioned concentration-dependent self-assembling with the Kirkwood–Alder transition.[50,51] The threshold concentration for the former and the latter are 0.494–0.545 in volume fraction ϕ for a hard particle, corresponding to 44–48 wt% in f_{PSiP}, respectively, by assuming that the hard sphere has diameter D_{PY}. The closed packing for the compact core-shell model can be achieved at 79 wt% in f_{PSiP}, which is presumably the maximum concentration in a uniformly ordered state. The threshold concentration between the solid and liquid states and that between the disorder and order states are roughly close to each other, which can be reasonably understood by the Kirkwood–Alder transition.

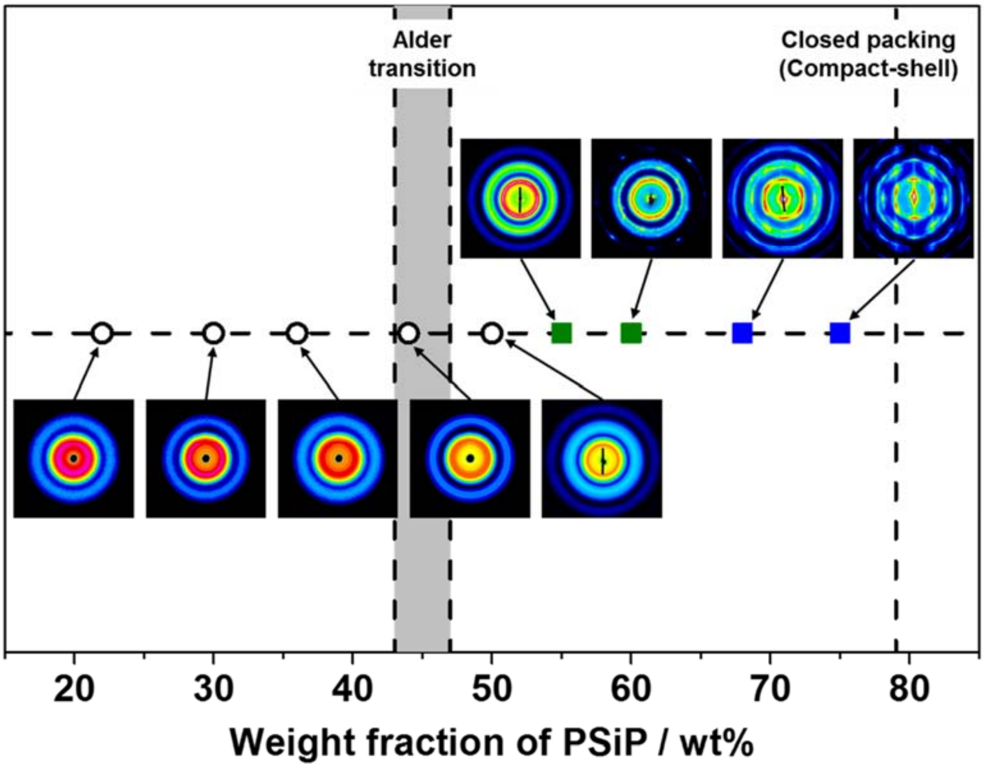

Figure 2-7. Higher-order structure and state of PSiP/IL composites as a function of particle concentration; liquid-disorder (black open circle), rhcp (green filled square), and fcc (blue filled square). For Alder transition and closed packing, see the accompanying text.

The rhcp was also obtained at around the threshold concentration for the equilibrium system of the PSiP of a CPB of poly(methyl methacrylate) in a good organic solvent.[20] Noted that these two systems are understood in a similar situation: the solvent is good for the CPB layer, and the main repulsive interaction between PSiPs is the steric hindrance by the swollen brushes (even in the present system, additional (electrostatic) interaction of a polyelectrolyte-type brush is shielded in IL of a high ionic strength).

Thus, we herein also discuss why the fcc was formed at higher concentrations. In the second closed-packed plane, a particle is placed at two different positions, A and B, relative to the first plane, i.e., whether a particle is at its underneath in the first layer. Since any long-range interaction between discontiguous particles can be ignored for our system because of the extremely high ionic strength, position A or B must be randomly selected, which gives rise to rhcp stacking. This is the case at $f_{\mathrm{PSiP}} \leqq$ 60 wt%; the $D_{\mathrm{dis,diff}}$ value was close to D_{PY}, indicating that the swollen CPB layer was little compressed and retained its spherical form. In contrast, the $D_{\mathrm{dis,diff}}$ value at f_{PSiP} = 68 and 75 wt% was close to D_{c}, indicating that the swollen CPB layer was highly compressed. This means extremely high (osmotic) repulsion force imposed for a particle from 12 neighboring particles. This situation is different in the fcc and hcp; Figure 2-8 shows schematic illustrations of the stacking of particles and the interaction between neighboring shell layers in (a) fcc (ABC-stacking) and (b) hcp (ABA-stacking) structures. For a PSiP, the total force from the nearest neighbors is zero in the fcc but not in the hcp; of course, such force can be balanced in a macroscopic scale. This heterogeneity may result in enhancing the difference of thermodynamic stability between these two stackings. The possibility of kinetic controlled assembling cannot be entirely ruled out, and the further detailed study is still ongoing.

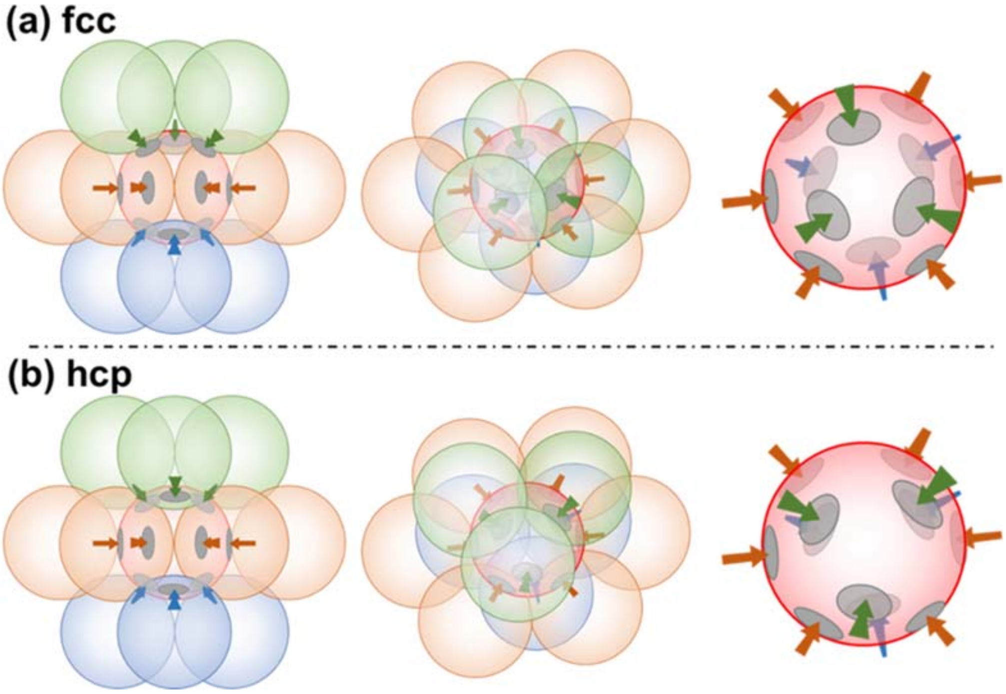

Figure 2-8. Schematic illustrations of the stacking of particles and the interaction between neighboring shell layers in (a) fcc (ABC-stacking) and (b) hcp (ABA-stacking) structures: the arrow and gray ellipsoid depict the force for the center particle (red sphere) from neighboring ones and the interacting region of overlapped shell layers, respectively. The overlapped area depends on the particle concentration, i.e., the pressure.

2-4. Conclusion

I fabricated and analyzed higher-order structures of CPB-modified nanoparticles in IL with a wide range of concentrations. I evaluated the “effective” swollen structure of PSiP using Percus–Yevick model in lower concentration of PSiP, and revealed the concentration-dependent crystallization of PSiP in higher concentration as well. The higher-order (crystal) structures of PSiP/IL composites are rhcp and fcc, although the structure depends on the concentration of PSiP. While the swollen CPBs in good solvents indicate high elasticity, this work reveals the relationship between the concentration and the higher-order structure of colloidal particles with high elasticity. In future, the relationship between the concentration and the interparticle potential of colloidal particles will be investigated to understand the formation of higher-order structure of colloidal particles with polymer brushes, which may results in the development of new application of colloidal system with regularly-arrayed structures.

References

1. K. Matyjaszewski. *Macromolecules* **2012**, *45*, 4015–4039.

2. M. Ouchi, T. Terashima, M. Sawamoto. *Chem. Rev.* **2009**, *109*, 4963–5050.

3. E. Rizzardo, D. H. Solomon. *Aust. J. Chem.* **2012**, *65*, 945–969.

4. G. Moad, E. Rizzardo, S. H. Thang. *Aust. J. Chem.* **2012**, *65*, 985–1076.

5. S. Yamago. *Chem. Rev.* **2009**, *109*, 5051–5068.

6. T. Fukuda, A. Goto, K. Ohno. *Macromol. Rapid Comm.* **2000**, *21*, 151–165.

7. C. Boyer, N. A. Corrigan, K. Jung, D. Nguyen, T. K. Nguyen, N. N. M. Adnan, S. Oliver, S. Shanmugam, J. Yeow. *Chem. Rev.* **2016**, *116*, 1803–1949.

8. Y. Tsujii, K. Ohno, S. Yamamoto, A. Goto, T. Fukuda. *Adv. Polym. Sci.* **2006**, *197*, 1–45.

9. M. Kobayashi, Y. Terayama, M. Kikuchi, A. Takahara. *Soft Matter* **2013**, *9*, 5138–5148.

10. R. Barbey, L. Lavanant, D. Paripovic, N. Schuwer, C. Sugnaux, S. Tugulu, H. A. Klok. *Chem. Rev.* **2009**, *109*, 5437–5527.

11. D. Dukes, Y. Li, S. Lewis, B. Benicewicz, L. Schadler, S. K. Kumar. *Macromolecules* **2010**, *43*, 1564–1570.

12. M. Ejaz, S. Yamamoto, K. Ohno, Y. Tsujii, T. Fukuda. *Macromolecules* **1998**, *31*, 5934–5936.

13. S. Yamamoto, M. Ejaz, Y. Tsujii, M. Matsumoto, T. Fukuda. *Macromolecules* **2000**, *33*, 5602–5607.

14. S. Yamamoto, M. Ejaz, Y. Tsujii, T. Fukuda. *Macromolecules* **2000**, *33*, 5608–5612.

15. A. Nomura, K. Ohno, T. Fukuda, T. Sato, Y. Tsujii. *Polym. Chem.* **2012**, *3*, 148–153.

16. C. Yoshikawa, A. Goto, Y. Tsujii, T. Fukuda, T. Kimura, K. Yamamoto, A. Kishida. *Macromolecules* **2006**, *39*, 2284–2290.

17. C. Yoshikawa, A. Goto, Y. Tsujii, N. Ishizuka, K. Nakanishi, T. Fukuda. *J. Polym. Sci., Part A: Polym. Chem.* **2007**, *45*, 4795–4803.

18. K. Ohno, T. Morinaga, S. Takeno, Y. Tsujii, T. Fukuda. *Macromolecules* **2006**, *39*, 1245–1249.

19. K. Ohno, T. Morinaga, S. Takeno, Y. Tsujii, T. Fukuda. *Macromolecules* **2007**, *40*, 9143–9150.

20. T. Morinaga, K. Ohno, Y. Tsujii, T. Fukuda. *Macromolecules* **2008**, *41*, 3620–3626.

21. T. Morinaga, K. Ohno, Y. Tsujii, T. Fukuda. *Eur. Polym. J.* **2007**, *43*, 243–248.

22. Y. Huang, T. Morinaga, Y. Tai, Y. Tsujii, K. Ohno. *Langmuir* **2014**, *30*, 7304–7312.

23. H. Sabouri, Y. Huang, K. Ohno, S. Perrier. *Nanoscale* **2015**, *7*, 19036–19046.

24. W. K. Kegel, A. van Blaaderen. *Science* **2000**, *287*, 290–293.

25. P. N. Pusey, W. Vanmegen. *Nature* **1986**, *320*, 340–342.

26. W. Vanmegen, S. M. Underwood. *Nature* **1993**, *362*, 616–618.

27. A. Kose, S. Hachisu. *J. Colloid Interface Sci.* **1974**, *46*, 460–469.

28. Z. D. Cheng, W. B. Russell, P. M. Chaikin. *Nature* **1999**, *401*, 893–895.

29. J. X. Zhu, M. Li, R. Rogers, W. Meyer, R. H. Ottewill, W. B. Russell, P. M. Chaikin. *Nature* **1997**, *387*, 883–885.

30. S. Hachisu, Y. Kobayashi, A. Kose. *J. Colloid Interface Sci.* **1973**, *42*, 342–348.

31. S. Hachisu, K. Takano. *Adv. Colloid Interface Sci.* **1982**, *16*, 233–252.

32. I. S. Sogami, T. Yoshiyama. *Phase Transitions* **1990**, *21*, 171–182.

33. R. Williams, R. S. Crandall. *Phys. Lett. A* **1974**, *48*, 225‑226.

34. N. A. Clark, A. J. Hurd, B. J. Ackerson. *Nature* **1979**, *281*, 57–60.

35. H. Yoshida, J. Yamanaka, T. Koga, N. Ise, T. Hashimoto. *Langmuir* **1998**, *14*, 569–574.

36. H. Yoshida, K. Ito, N. Ise. *Phys. Rev. B* **1991**, *44*, 435–438.

37. P. A. Hiltner, I. M. Krieger. *J. Phys. Chem.* **1969**, *73*, 2386–2389.

38. T. Okubo. *Prog. Polym. Sci.* **1993**, *18*, 481–517.

39. Y. Huang, A. Takata, Y. Tsujii, K. Ohno. *Langmuir* **2017**, *33*, 7130–7136.

40. T. Sato, T. Morinaga, S. Marukane, T. Narutomi, T. Igarashi, Y. Kawano, K. Ohno, T. Fukuda, Y. Tsujii. *Adv. Mater.* **2011**, *23*, 4868–4872.

41. T. Morinaga, S. Honma, T. Ishizuka, T. Kamijo, T. Sato, Y. Tsujii. *Polymers* **2016**, *8*, 146.

42. T. B. Martin, K. I. S. Mongcopa, R. Ashkar, P. Butler, R. Krishnamoorti, A. Jayaraman. *J. Amer. Chem. Soc.* **2015**, *137*, 10624–10631.

43. H. Koerner, L. F. Drummy, B. Benicewicz, Y. Li, R. A. Vaia. *ACS Macro Lett.* **2013**, *2*, 670–676.

44. J. S. Meth, S. G. Zane, C. Z. Chi, J. D. Londono, B. A. Wood, P. Cotts, M. Keating, W. Guise, S. Weigand. *Macromolecules* **2011**, *44*, 8301–8313.

45. V. Goel, J. Pietrasik, H. C. Dong, J. Sharma, K. Matyjaszewski, R. Krishnamoorti. *Macromolecules* **2011**, *44*, 8129–8135.

46. G. A. Williams, R. Ishige, O. R. Cromwell, J. Chung, A. Takahara, Z. B. Guan. *Adv. Mater.* **2015**, *27*, 3934–3941.

47. R. Ishige, G. A. Williams, Y. Higaki, N. Ohta, M. Sato, A. Takahara, Z. B. Guan. *Iucrj* **2016**, *3*, 211–218.

48. T. Palberg. *J. Phys. Condens. Matter* **1999**, *11*, R323–R360.

49. T. Palberg. *J. Phys.: Condens. Matter* **2014**, *26*, 333101.

50. W. G. Hoover, F. H. Ree. *J. Chem. Phys.* **1967**, *47*, 4873–4878.

51. B. J. Alder, W. G. Hoover, D. A. Young. *J. Chem. Phys.* **1968**, *49*, 3688–3696.

52. P. N. Pusey, W. Vanmegen. *Phys. Rev. Lett.* **1987**, *59*, 2083–2086.

53. M. Daoud, J. P. Cotton. *J. Phys. (Paris)* **1982**, *43*, 531–538.

54. E. B. Zhulina, T. M. Birshtein, O. V. Borisov. *Eur. Phys. J. E* **2006**, *20*, 243–256.

55. J. Kalb, D. Dukes, S. K. Kumar, R. S. Hoy, G. S. Grest. *Soft Matter* **2011**, *7*, 1418–1425.

56. K. Ohno, T. Akashi, Y. Huang, Y. Tsujii. *Macromolecules* **2010**, *43*, 8805–8812.

57. A. Guinier. X-ray Diffraction In Crystals, Imperfect Crystals, and Amorphous Bodies; Dover: New York, **1994**.

58. T. Hashimoto, M. Fujimura, K. Hiromichi. *Macromolecules* **1980**, *13*, 1660–1669.

59. J. K. Percus, G. J. Yevick. *Phys. Rev.* **1958**, *110*, 1–13.

60. M. S. Wertheim. *Phys. Rev. Lett.* **1963**, *10*, 321–323.

61. J. L. Lebowitz. *Phys. Rev.* **1964**, *133*, A895–A899.

62. M. Kotlarchyk, S. H. Chen. *J. Chem. Phys.* **1983**, *79*, 2461–2469.

63. K. Ohno, K. Koh, Y. Tsujii, T. Fukuda. *Angew. Chem. Int. Ed.* **2003**, *42*, 2751–2754.

64. W. Loose, B. J. Ackerson. *J. Chem. Phys.* **1994**, *101*, 7211–7220.

Chapter 3

USAXS analysis of concentration-dependent self-assembling of polymer-brush-modified nanoparticles in ionic liquid: [II] semi dilute-brush regime

3-1. Introduction

Well-defined and low-polydispersity polymers, for example dendrimers, star polymers, and block-copolymer, can be synthesized by living radical polymerization[1-7] (LRP; also called controlled reversible-deactivation radical polymerization as per the IUPAC recommendation). Polymeric nanocolloids such as dendrimers, star polymers, and block-copolymer micelles self-organize in a number of ordered structures. By tuning copolymer molecular weight and composition, solution concentration, monomer incompatibility, and temperature, specific transitions such as body-centered cubic (bcc) and face-centered cubic (fcc) can be placed for experimental convenience. Huge number of research papers have already published from various groups currently. By the way, colloidal suspension also can be formed bcc and fcc for "soft" colloidal crystal, derived from electrostatic (Coulomb) potential. In the papers about simulations on the crystallization of colloidal particles with Coulomb interaction, the structure formation of bcc and fcc was discussed.[8,9] The experimental examples for colloidal suspensions to form bcc structure were silica or latex particle suspensions with Coulomb interaction categorized as "soft" colloidal crystal.[10-15] The other paper also showed that the silica particles which poly(maleic anhydride-*co*-styrene), poly(methyl methacrylate) (PMMA), or polystyrene 'grafted-to' formed bcc or fcc structure.[16]

Our group has already developed synthesizing concentrated polymer brush using surface-initiated living radical polymerization. The graft density in such cases is more than one order of magnitude higher than that of a typical "semi-dilute" polymer brush (SDPB), going deep into the "concentrated"-brush regime.[17-19] Graft chains of such a concentrated polymer brush (CPB) in a good solvent are highly extended, almost to their full lengths, because of the exceptionally high osmotic pressure of the brush,[17,20,21] Because of such a highly stretched conformation, CPB in a good solvent exhibits characteristics such as high resistance against compression, very less mutual interpenetration that gives rise to very high lubrication with an extremely low friction coefficient ($\mu \sim 10^{-4}$),[17,18,22] and definite size exclusion with a very low threshold of molecular weight that gives good biocompatibility in an aqueous system.[17,23,24] Such highly repulsive and lubricating properties lead to a good dispersion of CPB-modified silica nanoparticles (PSiPs), thereby forming stable suspensions and colloidal crystals above a certain concentration. The obtained colloid crystals of PSiPs can be distinguished as a "semi-soft" type[25-29] in contrast to the previously reported "hard"[30-35] and "soft"[36-44] types which are formed by a hard-sphere and electrostatic interactions, respectively. Note that the above-mentioned semi-soft colloidal crystals can be formed even in an ionic liquid in which the electrostatic interactions are shielded. Also using ionic liquid is expected to allow us to verify an assembled structure with higher concentration of PSiP. Our previous work revealed concentration-dependent self-assembling of PSiPs in ionic liquid with a wide range of concentrations.[45] The interparticle potential of PSiPs can be controlled by changing the molecular weight of CPBs, which is categorized as CPB regime with lower molecular weight and semidilute polymer brush (SDPB) regime with higher molecular weight. The crystal structure of PSiP in SDPB regime is expected to be different from the one in CPB regime because not only the mean thickness of the brush layer but also the radial concentration profile of polymer segments and hence the interparticle potential should be functions of the surface density and chain length of graft polymer as well as the size of the core particle. However, there are no paper that the bcc crystal, which is expected to be formed when interparticle potential becomes softer, is experimentally observed in a colloidal system of PSiP.

Among the various methods available for structural analyses, small-angle X-ray scattering (SAXS) method is one of the most powerful techniques. In this study, we carried out measurements at ultra-small angles, because we used over submicron-scale materials. Recently, ultra-small-angle X-ray scattering

(USAXS) was used to analyze the higher-order structure of polymer-brush-modified nanoparticles in a stretched polymer film.[46,47]

In this study, we systematically analyzed higher-order structures of high molecular weight of polymer-brush-modified nanoparticles above the threshold of CPB/SDPB regime in an ionic liquid as a function of particle concentration using the USAXS method.

3-2. Experimental section

3-2-1. Materials

Silica particle (SiP) (SEAHOSTER KE-E10, 20 wt% suspension of SiP in ethylene glycol) was kindly donated by Nippon Shokubai Co., Ltd., Osaka, Japan. Methyl methacrylate (MMA, 99%) was obtained from Nacalai Tesque Inc. and purified by passing through a column of activated basic alumina to remove inhibitor. Tetrahydrofuran (Nacalai Tesque Inc., Japan, 98%) was distilled by Solpure (Techno Sigma Inc., Japan) before using as solvent, and *N*,*N*-diethyl-*N*-(2-methoxyethyl) ammonium bis(trifluoromethane sulfonyl) imide (IL; Kanto Chemical Co., Inc., Japan) was used as received.

3-2-2. Synthesis and characterization of polymer-brush-modified hybrid particles

The silica particles densely grafted with poly(methyl methacrylate) (PMMA–SiPs) were synthesized by surface-initiated atom transfer radical polymerization (ATRP), as reported previously,[29] which gave a graft polymer with M_n=248000, M_w=280000, M_w/M_n =1.13, σ=0.64 chains/nm^2, and σ^*=35% where M_n, M_w, M_w/M_n, σ, and σ^* are the number average molecular weight, the weight average molecular weight, the polydispersity index, the graft density and the surface occupancy of grafted PMMA. The core diameter was 148 nm, which was determined by USAXS previously.[45] The hydrodynamic diameter D_h of PMMA–SiPs in IL at 25 °C was determined by dynamic light scattering (DLS) measurements, which were performed with an ELS-ZA2 (Otsuka Electronics) instrument. The intensity correlation function $g^{(2)}(\tau)$ can be given by a single exponential function, as follows,

$$g^{(2)}(\tau) = 1 + \exp(-2\Gamma\tau) \tag{3-1}$$

where Γ is the characteristic rate for the translational diffusion and τ is the correlation time. Γ is related to the translational diffusion coefficient C_{dif} by

$$\Gamma = C_{\mathrm{dif}} q^2 \tag{3-2}$$

where q is the scattering vector. The hydrodynamic diameter D_{h} can be calculated by the Stokes–Einstein equation

$$D_{\mathrm{h}} = \frac{k_{\mathrm{B}} T}{3\pi\eta C_{\mathrm{dif}}} \tag{3-3}$$

where η is the solvent viscosity, k_{B} is the Boltzmann constant, and T is the absolute temperature.

3-2-3. Preparation of PMMA–SiP/IL composites

The mixed solution was obtained by mixing IL and PMMA–SiP/THF suspension. The concentration of THF was 60 wt% in the solution. Then, the prepared solution was casted by being vapored for 12h and dried in vacuum oven at 90 °C for 24h to obtain PMMA–SiP/IL composites. The weight fraction of PMMA–SiP/IL composites was 3/93, 5/95, 7/93, 10/90, 15/85, 25/75, 35/65, 45/55, 55/45, 65/35 and 75/25, while the sample code of each sample was defined as P-03, P-05, P-07, P-10, P-15, P-25, P-35, P-45, P-55, P-65 and P-75, respectively. The suspensions for P-25, P-35, P-45, P-55, P-65, and P-75 were casted on the Teflon sheet (YODOFLON, manufactured by Yodogawa Hu-Tech Co. Ltd.) and dried in vacuum oven at 90 °C for 24h. On the other hand, the suspensions for P-03, P-05, P-07, P-10, and P-15 were injected into the capillary (Hilgenberg GmbH, Malsfeld, Germany), whose edge-diameters were 3 mm, then, heated with argon gas flow at 90 °C to vapor THF for and dried in vacuum oven at 90 °C for 24h.

3-2-4. Ultra-small-angle/small-angle X-ray scattering (USAXS) measurements

Ultra-small-angle X-ray scattering (USAXS) measurements were performed at the beamlines, BL19B2 and BL03XU, in SPring-8 (Harima, Hyogo, Japan). The USAXS profiles were obtained on a two-dimensional hybrid pixel array detector, PILATUS 2M with 3 × 6 modules (DECTRIS Ltd.) and 1475 × 1679 pixels of 172 μm pixel size at BL19B2, on a complementary metal oxide semiconductor image sensor (CMOS) camera (C11440-22C; Hamamatsu Photonics, Shizuoka, Japan) coupled to an X-ray image intensifier system (V7735P; Hamamatsu Photonics) consisting of 2048 × 2048 pixels with a 43.1 μm pixel size at BL40B2, and on an imaging plate (IP; Rigaku R-AXIS VII) with 3000 × 3000 pixels of a 100 μm pixel size at BL03XU. The X-ray beam size at the sample position (horizontal × vertical) was 300 μm × 100 μm (BL19B2), 600 μm × 600 μm (BL40B2), and 112 μm × 100 μm (BL03XU). The X-ray wavelengths (λ) were 0.0689 nm (BL19B2), 0.19 nm (BL40B2), and 0.15 nm (BL03XU). The sample-to-detector distances were 42629 mm, 41741 mm, or 41546 mm (BL19B2), 4325 mm (BL40B2), and 7870 mm (BL03XU). The scattered intensities are expressed as a function of the scattering vector, $q = (4\pi \sin\theta)/\lambda$, where 2θ is the scattering angle relative to the incident beam. The q value was calibrated using a collagen fiber extracted from a chicken leg.

3-3. Results and Discussion

3-3-1. Structural analyses of PMMA–SiP/IL composites

According to the DLS measurement, the hydrodynamic diameter D_h of PMMA–SiPs in IL is 550 nm. We previously reported that the D_h value of the similar molecular weight of PMMA brush-modified particles (M_n=231000, M_w=293000, M_w/M_n=1.27, σ=0.71 chains/nm^2, and σ^*=40%) in acetone was 580 nm,[26] which was approximately consistent with that of PMMA–SiPs in IL. Acetone is one of a good solvent of PMMA, which means that PMMA brush on SiPs were well-swollen in IL as a good solvent.

The states of all PMMA–SiP/IL composites were determined by a simple test tube inverting method. According to this method, the states of only P-03 and P-05 were liquid. Figure 3-1(a) shows all USAXS intensity profiles of PMMA–SiP/IL composites. For lower concentration of PMMA–SiPs such as P-03 and P-05, there was no diffraction pattern in the USAXS profiles as well as their scattering images (Figure 3-2(a) and (b)). It means that the structure of P-03 and P-05 was liquid-disorder.

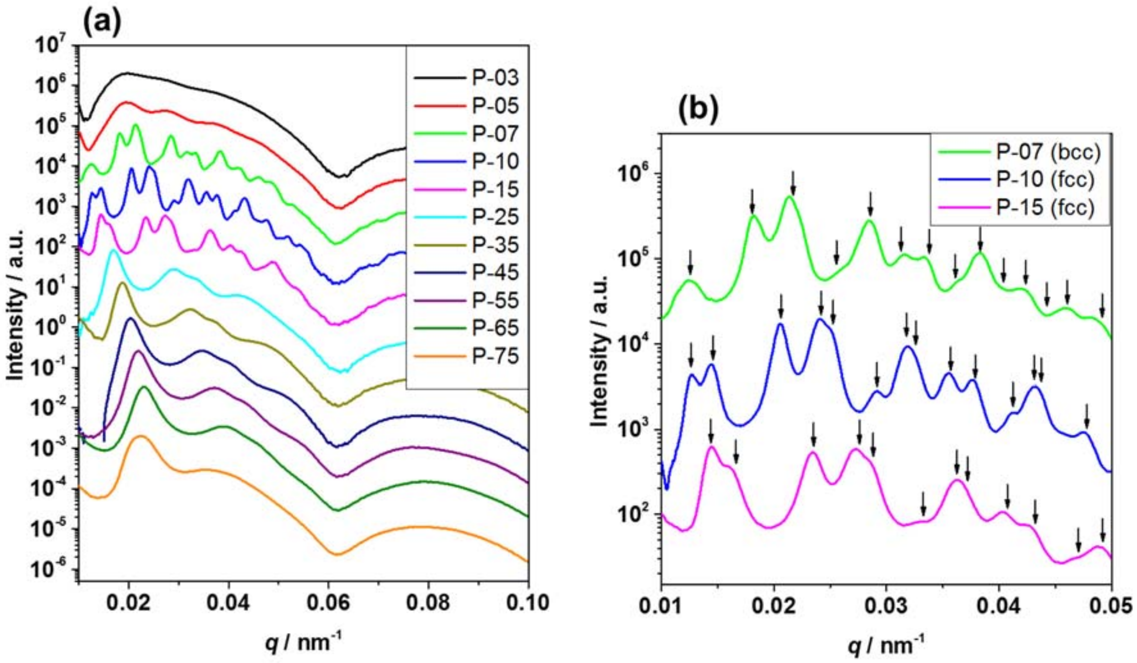

Figure 3-1. (a) USAXS intensity profiles of PMMA–SiP/IL composites measured in BL19B2. The profiles of P-07, P-10, and P-15 include the diffraction patterns derived from colloidal crystals. (b) USAXS intensity profiles of P-07, P-10, and P-15. The inset arrows indicates the predicted diffraction spots as bcc or fcc.

Figure 3-1(b) shows USAXS intensity profiles of P-07, P-10, and P-15, in which the diffraction pattern appeared clearly. For P-07, the first three diffraction peaks were observed at q values of the q/q^*ratio of approximately $1:\sqrt{2}:\sqrt{3}$. This was reasonably ascribed to the bcc- or simple cubic (sc)-type lattice, but not to the fcc, the hcp, or the rhcp. The center-to-center distance D_{dis} between neighboring particles was estimated from the following equations:

$$D_{\mathrm{dis}} = \begin{cases} \dfrac{2\pi}{q_{100}} = \dfrac{2\sqrt{2}\pi}{q_{110}} & \text{(sc)} \\ \dfrac{\sqrt{6}\pi}{q_{110}} = \dfrac{2\sqrt{3}\pi}{q_{200}} & \text{(bcc)} \end{cases} \tag{3-4}$$

where q_{hkl} is the peak value of the diffraction from the (hkl) plane. According to this equation for sc-type, D_{dis} of P-07 is estimated to be 492 nm. This means that if the crystal structure of P-07 was sc, polymer brushes on SiP were strongly shrunk in spite of the lower concentration because D_{h} of PMMA–SiPs in IL is 550 nm. To determine the crystal structure more concisely, using 2D scattering images is

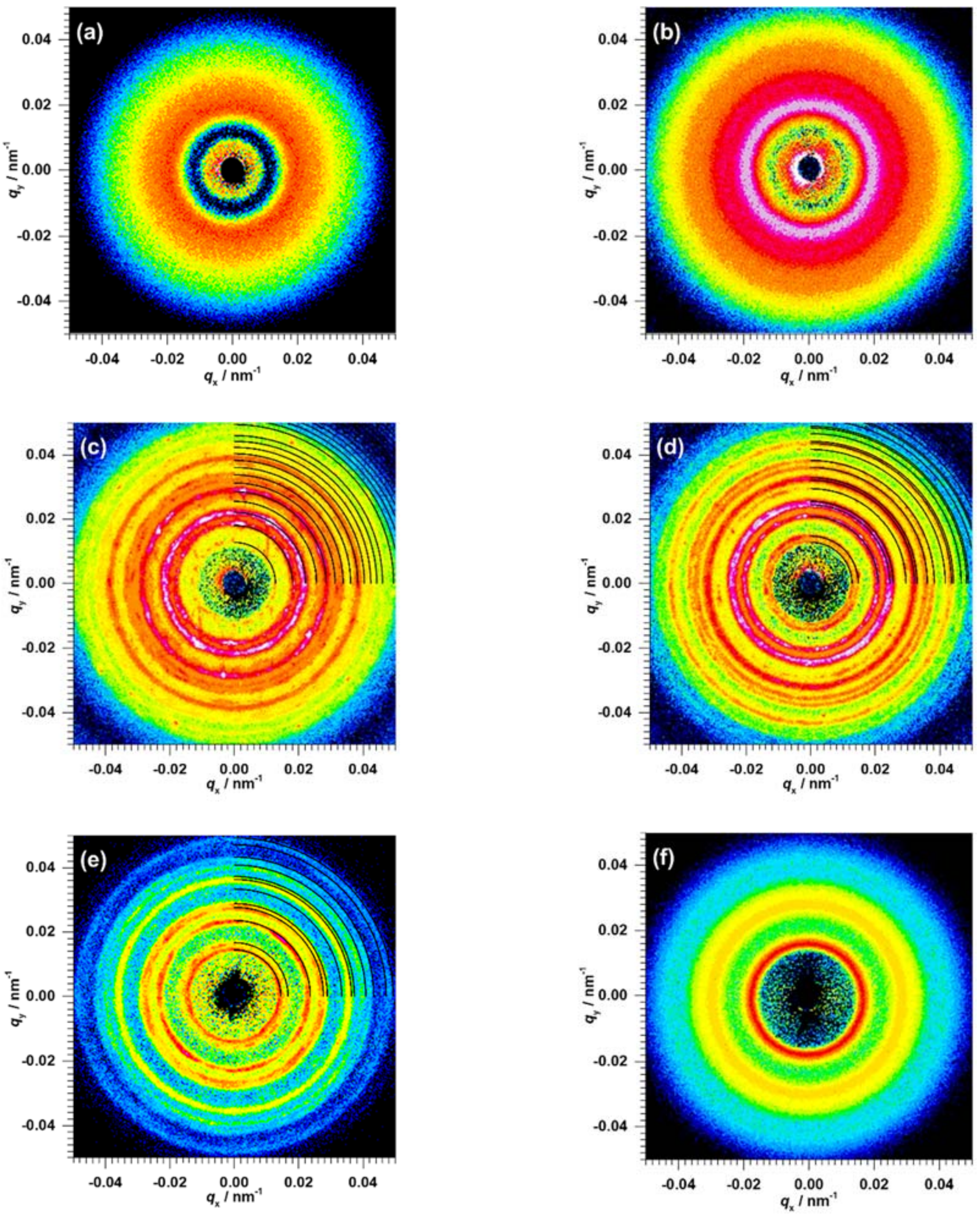

Figure 3-2. USAXS image of (a) P-03, (b) P-05, (c) P-07, (d) P-10, (e) P-15, and (f) P-25 measured in BL19B2. The black lines in each figure are predicted diffraction pattern as (c) bcc and (d)(e) fcc.

effective in terms of finding whether the minor components exist or not. Figure 3-2(a) and Figure 3-3 show diffraction images of P-07 and P-07' with the prediction of bcc-type diffraction pattern having D_{dis} of 603 nm and 610 nm, respectively. These comparisons of diffraction patterns for each sample was well-fitted and other diffraction peaks except bcc were not clearly observed, so the crystal structure of P-07 and P-07' is considered to be bcc.

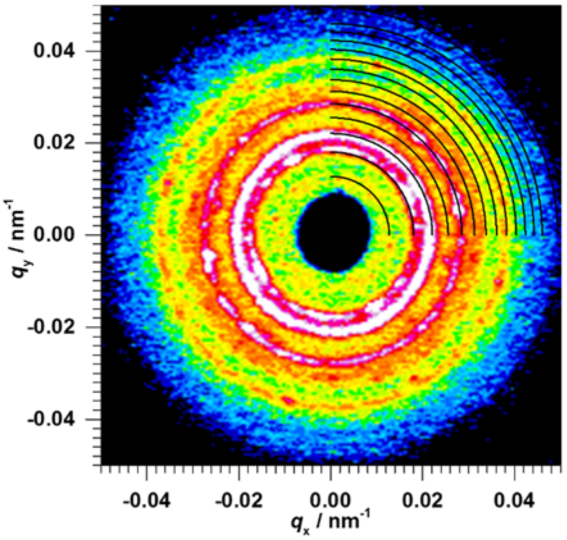

Figure 3-3. USAXS image of P-07 measured in BL03XU. The black lines in each figure are predicted diffraction pattern as bcc. The nearest neighbor distance of PSiP was determined as 610 nm.

For P-10 and P-15, the first three diffraction peaks were observed at q values of the q/q^*ratio of approximately $1:\sqrt{4/3}:\sqrt{8/3}$. The arrow marks for P-10 and P-15 in Figure 3-1(b) denote a fcc crystal having D_{dis} of 607 nm, and 533 nm, respectively. Also the crystal structure of P-10 and P-15 is fcc because there is no diffraction pattern categorized as any other crystals except fcc. These results mean that the crystal structure of P-10 and P-15 is fcc. The more discussion is given by these 2D diffraction images in terms of the comparison of the scattering intensity peak from the bcc- and fcc-crystal. The scattering intensity $I(q)$ is given by[48]

$$I(q) = KN(\langle F(q)^2\rangle + \langle F(q)\rangle^2[Z(q) - 1]) \tag{3-5}$$

where K is a constant depending on the type of radiation and sample properties, N is the number of scattering units, $F(q)$ is the form factor of the particle, and $Z(q)$ is lattice factor. The lattice factor of bcc and fcc crystals are written as follows respectively:[49]

$$Z_{\mathrm{bcc}}(q) = \frac{3\sqrt{3}\pi c}{16{D_{\mathrm{dis}}}^3 q^2} \sum_{\{hkl\}} m_{hkl} {S_{\mathrm{bcc}}}^2 L_{hkl}(q) \tag{3-6}$$

$$Z_{\mathrm{fcc}}(q) = \frac{\sqrt{2}\pi c}{16{D_{\mathrm{dis}}}^3 q^2} \sum_{\{hkl\}} m_{hkl} {S_{\mathrm{fcc}}}^2 L_{hkl}(q) \tag{3-7}$$

where c is constant of order unity whose exact value is calculated using the Porod invariant, D_{dis} is the nearest neighbor distance of nanoparticles, and $L_{hkl}(q)$ is a normalized peak shape function. h, k, and l indicates Miller index for crystals. The summation is over all sets of reflections (hkl) where m_{hkl} is the corresponding peak multiplicity. To discuss their structures more concisely, the comparison of lattice factor of bcc with fcc crystals is considered to be a valid and feasible way. The symmetry factor for bcc and fcc structure S_{bcc} and S_{fcc} are written as follows respectively:

$$S_{\mathrm{bcc}} = f\{1 + \exp[i\pi(h + k + l)]\} = \begin{cases} 2f, & h + k + l = \text{odd} \\ 0, & h + k + l = \text{even} \end{cases} \tag{3-8}$$

$$\begin{aligned} S_{\mathrm{fcc}} &= f\{1 + \exp[i\pi(h + k)] + \exp[i\pi(k + l)] + \exp[i\pi(l + h)]\} \\ &= \begin{cases} 4f, & h, k, l = \text{all odd or all even} \\ 0, & \text{otherwise} \end{cases} \end{aligned} \tag{3-9}$$

where f means atomic scattering factor. Considering that S_{bcc} is 0.5 times as much as S_{fcc}, Z_{bcc} is approximately same order magnitude of Z_{fcc} at the similar q range in peak positions. It means that diffraction peaks are obviously observed if the bcc or fcc crystals exist in the materials. It means that the crystal structure of P-07 is bcc, while P-10 and P-15 are fcc.

To discuss the sample for higher concentration of PSiP, for example P-25, Figure 3-2(f) shows the USAXS pattern of P-25, in which any diffraction patterns weren't clearly observed except the interparticle interference pattern. According to a simple test tube inverting method, the states of P-25 wasn't liquid, so the structure of P-25 is considered as solid-disorder. Also none of the diffraction peak is clearly observed in other USAXS intensity profiles for higher concentration of PSiP in Figure 3-1(a) such as P-35, P-45, P-55, P-65, and P-75, which indicates that the structure of these samples is considered as solid-disorder. Table 3-1 shows the structure and the nearest neighbor distance of PSiP determined from the diffraction patterns.

3-3-2. Structure formation of PMMA–SiP/IL composites

The crystal structure singly appeared in each PMMA–SiP/IL composites, especially P-07 was determined as the bcc structure. There are few papers which the single bcc was observed in colloidal suspensions, so the result that bcc structure singly appeared is one of the strong discussion points. In our

Table 3-1. Structure characteristics of PMMA–SiP/IL composites. C_{PSiP} means the concentration of PSiP/IL composites, and D_{dis} indicates the nearest neighbor distance of PSiP.

Sample ID	C_{PSiP}	Structure	D_{dis}
P-03	3 wt%	Liquid	
P-05	5 wt%	Liquid	
P-07	7 wt%	bcc	603 nm
P-10	10 wt%	fcc	607 nm
P-15	15 wt%	fcc	533 nm
P-25	25 wt%	Disorder	
P-35	35 wt%	Disorder	
P-45	45 wt%	Disorder	
P-55	55 wt%	Disorder	
P-65	65 wt%	Disorder	
P-75	75 wt%	Disorder	

previous work, the fcc structure was mainly formed for semisoft colloidal crystals in organic solvent in SDPB regime, which was expected to form fcc structure in IL as well. In this work, bcc structure was observed as well as fcc structure. Indeed, block copolymers and star polymers in the solution can form bcc structure for generic entropic reasons, which depend on the length scale of the repulsion.[50-55] The phenomenon for PMMA–SiP/IL composites which formed bcc structure is considered to be similar to the case of block copolymers and star polymers, which form like core–shell microsphere. For P-07 and P-10, in the range of the transition from bcc to fcc, the nearest distance between the particles (D_{dis}) was evaluated as approximately 600 nm, which is deemed to indicate that the packing fraction of PMMA–SiP in the composites has relation to bcc-fcc transition. As increasing the concentration of PMMA–SiPs in the composites, the crystal structure was not observed. Our previous work indicated that CPB-modified particles form fcc structure as the particle concentration become higher, which means that the most stable structure is considered as fcc structure for CPB-modified particles. However, the effect of the interpenetration of polymer brushes between PMMA–SiPs cannot be ignored, which possibly causes that the formation of crystals doesn’t occur.

3-4. Conclusion

USAXS method enabled us to fabricate and analyze concentration-dependent self-assembling of higher molecular weight of PMMA–SiPs in IL with a wide range of concentrations. The packing fraction of PMMA–SiPs is considered to be related to change their crystal structures were determined to be fcc as well as bcc, which is the first observation in semisoft colloidal crystal system.

References

1. K. Matyjaszewski. *Macromolecules* **2012**, *45*, 4015–4039.

2. M. Ouchi, T. Terashima, M. Sawamoto. *Chem. Rev.* **2009**, *109*, 4963–5050.

3. E. Rizzardo, D. H. Solomon. *Aust. J. Chem.* **2012**, *65*, 945–969.

4. G. Moad, E. Rizzardo, S. H. Thang. *Aust. J. Chem.* **2012**, *65*, 985–1076.

5. S. Yamago. *Chem. Rev.* **2009**, *109*, 5051–5068.

6. T. Fukuda, A. Goto, K. Ohno. *Macromol. Rapid Comm.* **2000**, *21*, 151–165.

7. C. Boyer, N. A. Corrigan, K. Jung, D. Nguyen, T. K. Nguyen, N. N. M. Adnan, S. Oliver, S. Shanmugam, J. Yeow. *Chem. Rev.* **2016**, *116*, 1803–1949.

8. S. Hamaguchi, R. T. Farouki, D. H. E. Dubin. *Phys. Rev. E* **1997**, *56*, 4671–4682.

9. A. P. Hynninen, M. Dijkstra. *Phys. Rev. E* **2003**, *68*, 021407.

10. Y. Monovoukas, A. P. Gast. *J. Colloid Interface Sci.* **1989**, *128*, 533–548.

11. P. A. Rundquist, P. Photinos, S. Jagannathan, S. A. Asher. *J. Chem. Phys.* **1989**, *91*, 4932–4941.

12. E. B. Sirota, H. D. Ouyang, S. K. Sinha, P. M. Chaikin, J. D. Axe, Y. Fujii. *Phys. Rev. Lett.* **1989**, *62*, 1524–1527.

13. T. Okubo. *Colloid Polym. Sci.* **1992**, *270*, 1018–1026.

14. L. Liu, S. H. Xu, J. Liu, Z. W. Sun. *J. Colloid Interface Sci.* **2008**, *326*, 261–266.

15. P. Wette, I. Klassen, D. Holland-Moritz, D. M. Herlach, H. J. Schope, N. Lorenz, H. Reiber, T. Palberg, S. V. Roth. *J. Chem. Phys.* **2010**, *132*, 131102.

16. T. Okubo, H. Ishiki, H. Kimura, M. Chiyoda, K. Yoshinaga. *Colloid Polym. Sci.* **2002**, *280*, 446–453.

17. Y. Tsujii, K. Ohno, S. Yamamoto, A. Goto, T. Fukuda. *Adv. Polym. Sci.* **2006**, *197*, 1–45.

18. M. Kobayashi, Y. Terayama, M. Kikuchi, A. Takahara. *Soft Matter* **2013**, *9*, 5138–5148.

19. R. Barbey, L. Lavanant, D. Paripovic, N. Schuwer, C. Sugnaux, S. Tugulu, H. A. Klok. *Chem. Rev.* **2009**, *109*, 5437–5527.

20. S. Yamamoto, M. Ejaz, Y. Tsujii, M. Matsumoto, T. Fukuda. *Macromolecules* **2000**, *33*, 5602–5607.

21. S. Yamamoto, M. Ejaz, Y. Tsujii, T. Fukuda. *Macromolecules* **2000**, *33*, 5608–5612.

22. A. Nomura, K. Ohno, T. Fukuda, T. Sato, Y. Tsujii. *Polym. Chem.* **2012**, *3*, 148–153.

23. C. Yoshikawa, A. Goto, Y. Tsujii, T. Fukuda, T. Kimura, K. Yamamoto, A. Kishida. *Macromolecules* **2006**, *39*, 2284–2290.

24. C. Yoshikawa, A. Goto, Y. Tsujii, N. Ishizuka, K. Nakanishi, T. Fukuda. *J. Polym. Sci., Part A: Polym. Chem.* **2007**, *45*, 4795–4803.

25. K. Ohno, T. Morinaga, S. Takeno, Y. Tsujii, T. Fukuda. *Macromolecules* **2006**, *39*, 1245–1249.

26. K. Ohno, T. Morinaga, S. Takeno, Y. Tsujii, T. Fukuda. *Macromolecules* **2007**, *40*, 9143–9150.

27. T. Morinaga, K. Ohno, Y. Tsujii, T. Fukuda. *Macromolecules* **2008**, *41*, 3620–3626.

28. T. Morinaga, K. Ohno, Y. Tsujii, T. Fukuda. *Eur. Polym. J.* **2007**, *43*, 243–248.

29. Y. Huang, T. Morinaga, Y. Tai, Y. Tsujii, K. Ohno. *Langmuir* **2014**, *30*, 7304–7312.

30. W. K. Kegel, A. van Blaaderen. *Science* **2000**, *287*, 290–293.

31. P. N. Pusey, W. Vanmegen. *Nature* **1986**, *320*, 340–342.

32. W. Vanmegen, S. M. Underwood. *Nature* **1993**, *362*, 616–618.

33. A. Kose, S. Hachisu. *J. Colloid Interface Sci.* **1974**, *46*, 460–469.

34. Z. D. Cheng, W. B. Russell, P. M. Chaikin. *Nature* **1999**, *401*, 893–895.

35. J. X. Zhu, M. Li, R. Rogers, W. Meyer, R. H. Ottewill, W. B. Russell, P. M. Chaikin. *Nature* **1997**, *387*, 883–885.

36. S. Hachisu, Y. Kobayashi, A. Kose. *J. Colloid Interface Sci.* **1973**, *42*, 342–348.

37. S. Hachisu, K. Takano. *Adv. Colloid Interface Sci.* **1982**, *16*, 233–252.

38. I. S. Sogami, T. Yoshiyama. *Phase Transitions* **1990**, *21*, 171–182.

39. R. Williams, R. S. Crandall. *Phys. Lett. A* **1974**, *48*, 225–226.

40. N. A. Clark, A. J. Hurd, B. J. Ackerson. *Nature* **1979**, *281*, 57–60.

41. H. Yoshida, J. Yamanaka, T. Koga, N. Ise, T. Hashimoto. *Langmuir* **1998**, *14*, 569–574.

42. H. Yoshida, K. Ito, N. Ise. *Phys. Rev. B* **1991**, *44*, 435–438.

43. P. A. Hiltner, I. M. Krieger. *J. Phys. Chem.* **1969**, *73*, 2386–2389.

44. T. Okubo. *Prog. Polym. Sci.* **1993**, *18*, 481–517.

45. Y. Nakanishi, R. Ishige, O. Hiroki, K. Sakakibara, K. Ohno, T. Morinaga, T. Sato, T. Kanaya, Y. Tsujii.

46. G. A. Williams, R. Ishige, O. R. Cromwell, J. Chung, A. Takahara, Z. B. Guan. *Adv. Mater.* **2015**, *27*, 3934–3941.

47. R. Ishige, G. A. Williams, Y. Higaki, N. Ohta, M. Sato, A. Takahara, Z. B. Guan. *Iucrj* **2016**, *3*, 211–218.

48. M. Kotlarchyk, S. H. Chen. *J. Chem. Phys.* **1983**, *79*, 2461–2469.

49. S. Forster, A. Timmann, M. Konrad, C. Schellbach, A. Meyer, S. S. Funari, P. Mulvaney, R. Knott. *J. Phys. Chem. B* **2005**, *109*, 1347–1360.

50. G. A. McConnell, A. P. Gast. *Macromolecules* **1997**, *30*, 435–444.

51. G. A. McConnell, A. P. Gast, J. S. Huang, S. D. Smith. *Phys. Rev. Lett.* **1993**, *71*, 2102–2105.

52. T. P. Lodge, B. Pudil, K. J. Hanley. *Macromolecules* **2002**, *35*, 4707–4717.

53. I. W. Hamley, C. Daniel, W. Mingvanish, S. M. Mai, C. Booth, L. Messe, A. J. Ryan. *Langmuir* **2000**, *16*, 2508–2514.

54. M. Laurati, J. Stellbrink, R. Lund, L. Willner, D. Richter, E. Zaccarelli. *Phys. Rev. Lett.* **2005**, *94*.

55. M. Laurati, J. Stellbrink, R. Lund, L. Willner, E. Zaccarelli, D. Richter. *Phys. Rev. E* **2007**, *76*.

Chapter 4

USAXS analysis of concentration-dependent self-assembling of polymer-brush-modified nanoparticles in ionic liquid: [III] Unified Explanation

4-1. Introduction

Well-defined and low-polydispersity polymers can be densely grown up on various solid surfaces by living radical polymerization[1-7] (LRP; also called controlled reversible-deactivation radical polymerization as per the IUPAC recommendation). The graft density in such cases is more than one order of magnitude higher than that of a typical "semi-dilute" polymer brush (SDPB), going deep into the "concentrated"-brush regime.[8-10] Graft chains of such a concentrated polymer brush (CPB) in a good solvent are highly extended, almost to their full lengths, because of the exceptionally high osmotic pressure of the brush.[8,11-13] Because of such a highly stretched conformation, CPB in a good solvent exhibits characteristics such as high resistance against compression, very less mutual interpenetration that gives rise to very high lubrication with an extremely low friction coefficient ($\mu \sim 10^{-4}$),[8,9,14] and definite size exclusion with a very low threshold of molecular weight that gives good biocompatibility in an aqueous system.[8,15,16]

Such highly repulsive and lubricating properties lead to a good dispersion of CPB-modified silica nanoparticles (PSiPs), thereby forming stable suspensions and colloidal crystals above a certain concentration. The obtained colloid crystals of PSiPs can be distinguished as a "semi-soft" type[17-22] in contrast to the previously reported "hard"[23-28] and "soft"[29-37] types which are formed by a hard-sphere and electrostatic interactions, respectively. Note that the above-mentioned semi-soft colloidal crystals can be formed even in an ionic liquid in which the electrostatic interactions are shielded. Different types of higher-order structures can be expected by varying the interparticle potential and particle concentration. For examples, there are typically three types of closed packing pattern: face-centered

cubic (fcc; ABC-stacking), hexagonal close packing (hcp; ABA-stacking), and random-hexagonal close packing (rhcp; random stacking). The difference lies in the way of stacking of the planes (A, B, or C), in which the colloids are hexagonally packed. Previous work by our group reported that PSiPs self-assemble in the rhcp structure in an organic solvent at the liquid/crystal-threshold concentration,[19] while they assemble in the fcc structure in an ionic liquid at a higher particle concentration.[38,39] Thermodynamic equilibrium was confirmed for the former but not for the latter. The latter focused on the application of such a self-assembled structure as a novel pseudo-solid electrolyte to a bipolar-type lithium-ion rechargeable battery. Therefore, a detailed and systematic study of the PSiP self-assembling process in an ionic liquid as a function of particle concentration should be carried out not only to further understand the basics of colloid science but also to develop highly functionalized devices.

This chapter discusses the concentration-dependent self-assembling of PSiP based on the above discussion. However, it is highly challenging to precisely analyze a higher-order structure of PSiP as a function of particle concentration. Among the various methods available for structural analyses, small-angle X-ray scattering (SAXS) method is one of the most powerful techniques. In this study, we systematically analyzed higher-order structures of CPB- and SDPB-modified nanoparticles in an ionic liquid as a function of particle concentration using the USAXS method.

Various static and dynamic aspects of the colloid crystals including phase behavior, crystal nucleation/growth process, and their control have been discussed over the last 50 years not only for fundamental understanding but also for a wide range of applications.[24,40,41] Among others, a so-called "hard sphere (HS)" system showing the Kirkwood–Alder transition,[42,43] i.e., phase transition from liquid to crystal, as well as an amorphous or glass phase with higher concentrations.[24,44] It has been most extensively studied on theories, simulations, and experiments and is still of great importance. The HS-model system most experimentally studied was polymeric colloids (nonswelling-bulk or micro-gel polymeric cores) sterically stabilized and dispersed in non-aqueous solvents, because the electrostatic interaction forming a soft shell must be shielded. For steric stabilization, a lyophilic polymer was usually adsorbed on the core particle. The problem in this system is the compression or desorption of polymeric stabilizer at a high particle concentration. As above-mentioned, our studied system is considered to be a good HS-model because of a sufficiently thin but completely repulsive CPB layer covalently end-grafted on a hard, nonswelling silica core as well as little electrostatic interaction (well shielded) in an ionic liquid.

4-2. Experimental section

4-2-1. Materials

N,*N*-Diethyl-*N*-(2-methacryloylethyl)-*N*-methylammonium bis(trifluoromethylsulfonyl) imide (DEMM) was obtained from Toyo Gosei Co., Ltd., Tokyo, Japan. Methyl methacrylate (MMA, 99%) was obtained from Nacalai Tesque Inc. and purified by passing through a column of activated basic alumina to remove inhibitor. Silica particle (SiP) (SEAHOSTER KE-E10, 20 wt% suspension of SiP in ethylene glycol) was kindly donated by Nippon Shokubai Co., Ltd., Osaka, Japan. *N*,*N*-diethyl-*N*-(2-methoxyethyl) ammonium bis(trifluoromethane sulfonyl) imide (DEME-TFSI; Kanto Chemical Co., Inc., Japan), acetonitrile (Kanto Chemical, 99.5%), and acetone (Wako Pure Chemical Industries, Ltd., Japan, 99.5%) were used as received. Tetrahydrofuran (THF; Nacalai Tesque Inc., Japan, 98%) was

Table 4-1. Characteristics of PSiPs.

Particles	Brush component	M_n[a]	M_w[a]	M_w/M_n[a]	x_w[a]	A_g[b]	σ [chains nm^{-2}] [b]	σ^*
P1	PMMA	6 600	8 400	1.27	84	0.074	0.33	19%
P2	PMMA	24 000	28 300	1.18	283	0.33	0.41	22%
P3	PMMA	131 000	175 000	1.34	1750	3.1	0.70	39%
P4	PMMA	248 000	280 000	1.13	2800	5.6	0.67	37%
P5	PDEMM	27 800	29 900	1.08	62	0.17	0.19	42%

[a] Measured by GPC-MALLS. [b] Determined by TGA results.

distilled by Solpure (Techno Sigma Inc., Japan) before using as solvent. An atom transfer radical polymerization (ATRP)-initiator-holding silane coupling agent, (2-bromo-2-methyl)propionyloxypropyltriethoxysilane (BPE), was synthesized as reported previously.[45]

4-2-2. Synthesis and characterization of polymer-brush-modified hybrid particles

BPE-modified SiP was prepared as mentioned in Chapter 2. P1, P2, and P3 were synthesized by surface-initiated ATRP, as reported previously.[21,46] P4 and P5 means particles used in Chapter 3 and Chapter 2, respectively. Their molecular characteristics are summarized in Table 4-1. The core diameter was 148 nm determined by USAXS as mentioned in Chapter 2. The gel permeation chromatographic (GPC) measurement (GPC-101 high-speed liquid chromatography system, Shoko Science Co, Ltd., Japan) to determine the molecular weight and its distribution. The weight of the grafted polymer relative to the SiP-core weight (A_g) was estimated by thermogravimetry (TGA-50 instrument, Shimadzu, Kyoto, Japan) under an argon atmosphere.

4-2-3. Preparation of PSiP/IL composites

In this study, all samples were prepared as the same way as in Chapter 3. A suspension of PSiP in solvent, acetonitrile for P1, THF for P2, and acetone for P3, was mixed with DEME-TFSI in different compositions; to this solution, each solvent was added to adjust its concentration to 60 wt% in the solution. Then, the prepared solutions were casted by slowly evaporating solvent for 12 h, followed by drying it in a vacuum oven at 90 °C for 24 h to obtain PSiP/IL composites in different compositions. The weight fractions of P1 in the composite were 20, 30, 40, 45, 50, 55, 65, and 70 by wt%, and they were denoted as P1-20, P1-30, P1-40, P1-45 P1-50, P1-55, P1-60, P1-65, and P1-70, respectively. The weight fractions of P2 in the composite were 10, 15, 25, 30, 35, 40, 45, 50, 55, 60, 68, and 75 by wt%, and they were denoted as P2-10, P2-15, P2-20, P2-30, P2-35, P2-40, P2-45 P2-50, P2-55, P2-60, P2-68, and P2-75, respectively. The weight fractions of P3 in the composite were 5, 7, 15, 20, and 30 by wt%, and they were denoted as P3-05, P3-07, P3-15, P3-20, and P3-30, respectively. Samples P2-68 and P2-75 were prepared on a Teflon sheet (YODOFLON, Yodogawa Hu-Tech Co. Ltd.), and others were prepared in the capillary with an outer-diameter of 2 or 3 mm (Hilgenberg GmbH, Malsfeld, Germany) because of their vicidity. For the capillary, a gentle flow of argon was applied.

4-2-4. Measurements

The hydrodynamic diameter D_{h} of all PSiPs in IL at 25 °C was determined by dynamic light scattering (DLS) measurements performed with an ELS-ZA2 (Otsuka Electronics) instrument, as the same way as in Chapter 3.

Ultra-small-angle X-ray scattering (USAXS) measurement was performed at the beamlines, BL19B2 and BL03XU, in SPring-8 (Harima, Hyogo, Japan). The USAXS profiles were obtained on a two-dimensional hybrid pixel array detector, PILATUS 2M with 3 × 6 modules (DECTRIS Ltd.) and 1475 × 1679 pixels of 172 μm pixel size at BL19B2, on a complementary metal oxide semiconductor image sensor (CMOS) camera (C11440-22C; Hamamatsu Photonics, Shizuoka, Japan) coupled to an X-ray image intensifier system (V7735P; Hamamatsu Photonics) consisting of 2048 × 2048 pixels with a 43.1 μm pixel size at BL40B2, and on a cooled charge-coupled device detector (CCD; Hamamatsu Photonics ORCA R2) coupled to an X-ray image intensifier (II; Hamamatsu Photonics V7739P) consisting of 1344 × 1024 pixels with a 63 μm pixel size or an imaging plate (IP; Rigaku R-AXIS VII) with 3000 × 3000 pixels of a 100 μm pixel size at BL03XU. The X-ray beam size at the sample position (horizontal × vertical) was 300 μm × 100 μm (BL19B2), 600 μm × 600 μm (BL40B2), and 112 μm × 100 μm (BL03XU). The X-ray wavelengths (λ) were 0.0689 nm (BL19B2), 0.19 nm (BL40B2), and 0.15 nm (BL03XU). The sample-to-detector distances were 41741 mm, 41546 mm, or 41548 mm (BL19B2), 4325 mm (BL40B2), 2599 mm (BL03XU using II+CCD), and 7870 mm (BL03XU using IP). The scattered intensities are expressed as a function of the scattering vector, $q = (4\pi \sin\theta)/\lambda$, where 2θ is the angle between the incident X-ray beam and the detector measuring the scattered intensity.

The *q* value was calibrated using a collagen fiber extracted from a chicken leg.

Field-emission scanning electron microscopy (FE-SEM) observation was carried out on a JSM-6700F instrument (JEOL Ltd., Japan). In order to observe the cross-sectional surface, the freeze-fractured sample was mounted on a brass stub and sputter-coated with gold/palladium to minimize sample charging using a Hitachi ion sputter E-1010.

4-3. Results and Discussion

According to the DLS measurement, the hydrodynamic diameter D_h of all PSiPs in IL is shown in Figure 4-1. We previously reported that the D_h value of PMMA brush-modified particles in acetone, which was approximately consistent with that of PMMA–SiPs in IL. Acetone is one of a good solvent of PMMA, which means that polymer brush of all PSiPs were well-swollen in IL as a good solvent. Using a simple tube-inverting method, the samples P1-20, P1-30, P1-40, P2-10, P2-15, and P2-20 were found to be liquid. Figure 4-2 shows the 1D USAXS intensity profiles of samples P1-20, P1-30, P1-40, P2-10, P2-15, and P2-20. No diffraction pattern was observed, suggesting that there were little higher-order structures. Figure 4-3(a) and (b) show the 2D USAXS images of P1-45 and P2-30, respectively.

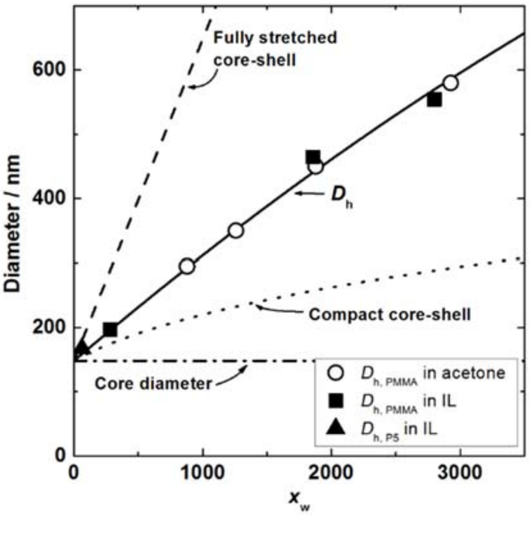

Figure 4-1. Plot of average hydrodynamic diameter D_h of PSiP as a function of degree of weight-average molecular weight x_w of the graft chains.

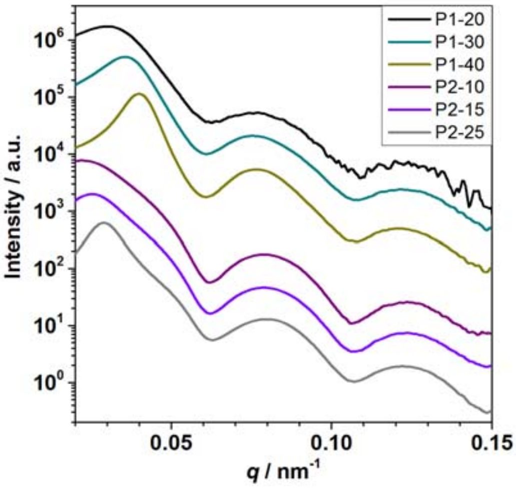

Figure 4-2. 1D USAXS intensity profile of P1-20 to P1-40, and P2-10 to P2-25. All USAXS profiles were obtained at BL03XU using II+CCD.

The diffraction patterns categorized as not only rhcp but also fcc structure were observed. In order to determine the main component structure, it is suitable to compare the intensity of (100) plane of the *hexagonal system* (hcp-type lattice) with one of (200) plane of the fcc-type lattice. The scattering intensity $I(q)$ of the particles can be obtained using the following relation:

$$I(q) = N[\langle F(q)^2\rangle + \langle F(q)\rangle^2 (Z(q) - 1)] \tag{4-1}$$

where *N* is a constant that is a function of the type of radiation used and the sample properties. $Z(q)$ is the lattice factor of particles. $F(q)$ is the form factor of particles, as shown in Chapter 2. Here, Using Miller indices (*hkl*) for a given crystal lattice plane, the lattice factor $Z(q)$ for an ideal undistorted fcc and hcp lattice, $Z_{\mathrm{fcc}}(q)$ and $Z_{\mathrm{hcp}}(q)$, can be written as the following equations:[47]

$$Z_{\mathrm{fcc}}(q) = \frac{\sqrt{2}\pi c}{16 {D_{\mathrm{dis}}}^3 q^2} \sum_{\{hkl\}} m_{hkl}\, {f_{\mathrm{fcc}}}^2 L_{hkl}(q) \tag{4-2}$$

$$Z_{\mathrm{hcp}}(q) = \frac{\sqrt{2}\pi c}{4 {D_{\mathrm{dis}}}^3 q^2} \sum_{\{hkl\}} m_{hkl}\, {f_{\mathrm{hcp}}}^2 L_{hkl}(q) \tag{4-3}$$

where D_{dis} is the center-to-center distance between neighboring particles, m_{hkl} is peak multiplicities, and $L_{hkl}(q)$ is a normalized peak shape function. The term c is a constant of order unity whose exact value is calculated using the Porod invariant. f_{fcc} and f_{hcp} is the symmetry factor that takes into account symmetry-related extinction rules, determined as follows:

$$f_{\mathrm{fcc}} = f\{1 + \exp[i\pi(h + k)] + \exp[i\pi(k + l)] + \exp[i\pi(l + h)]\} \qquad (4\text{-}4)$$

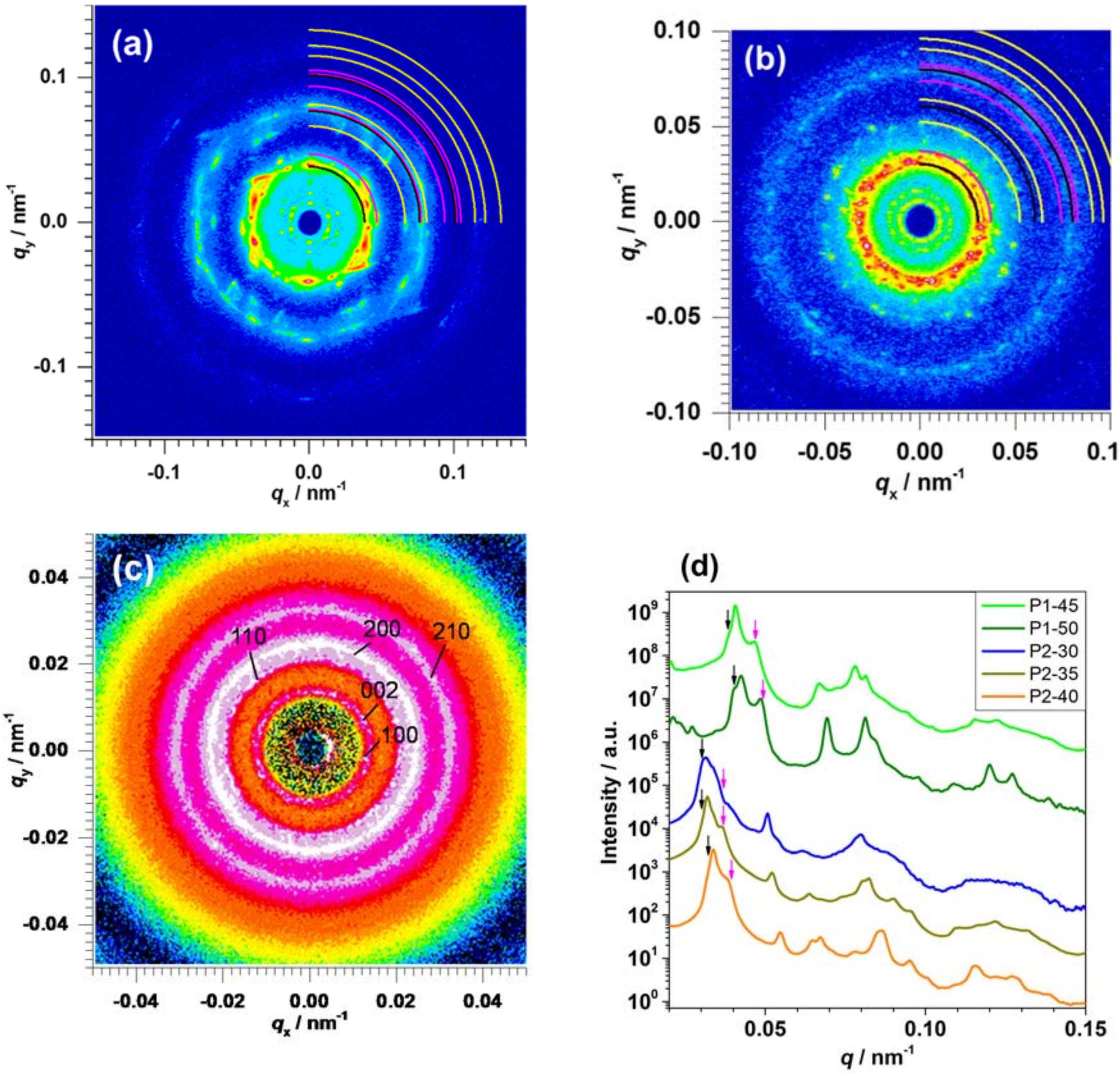

Figure 4-3. (a)(b)(c) 2D USAXS images of (a) P1-45, (b) P2-30, and (c) P3-05. The prediction lines of diffraction patterns of rhcp and fcc structure were colored with black and pink, respectively, while overlapped prediction lines of rhcp as well as fcc were described as yellow. The assigned *hkl* indices of the hcp-type lattice are given in the image of (c) P3-05. (d) 1D USAXS intensity profiles of P1-45, P1-50, P2-30, P2-35, and P2-40. The black and pink arrow indicate the diffraction position of the (100) plane of the hcp-type lattice and the (200) plane of fcc-type lattice, respectively.

$$f_{\mathrm{hcp}} = f\left\{1 + \exp\left[2\pi i\left(\frac{h+2k}{3} + \frac{l}{2}\right)\right]\right\} \tag{4-5}$$

where f means the atomic scattering factor. According to the previous research by Loose and Ackerson,[48] the scattered intensity of (100) plane of rhcp structure is considerably weaker than that of the perfect hcp structure. In this work, the intensity of the (100) plane of the rhcp was expedientially estimated as 1/10 of that of the hcp, which means that the lattice factor $Z(q)_{\mathrm{rhcp},100}$ of the rhcp structure was evaluated as 1/10 of $Z(q)_{\mathrm{hcp},100}$. If the rhcp structure and the fcc structure existed at the same ratio in each composite, the lattice factor ratio $Z(q)_{\mathrm{fcc},200}/Z(q)_{\mathrm{rhcp},100}$ was calculated as 27. However, the experimental lattice factor ratio $Z(q)_{\mathrm{fcc},200}/Z(q)_{\mathrm{rhcp},100}$ of P1-45 and P2-30 were 0.97 and 0.76,

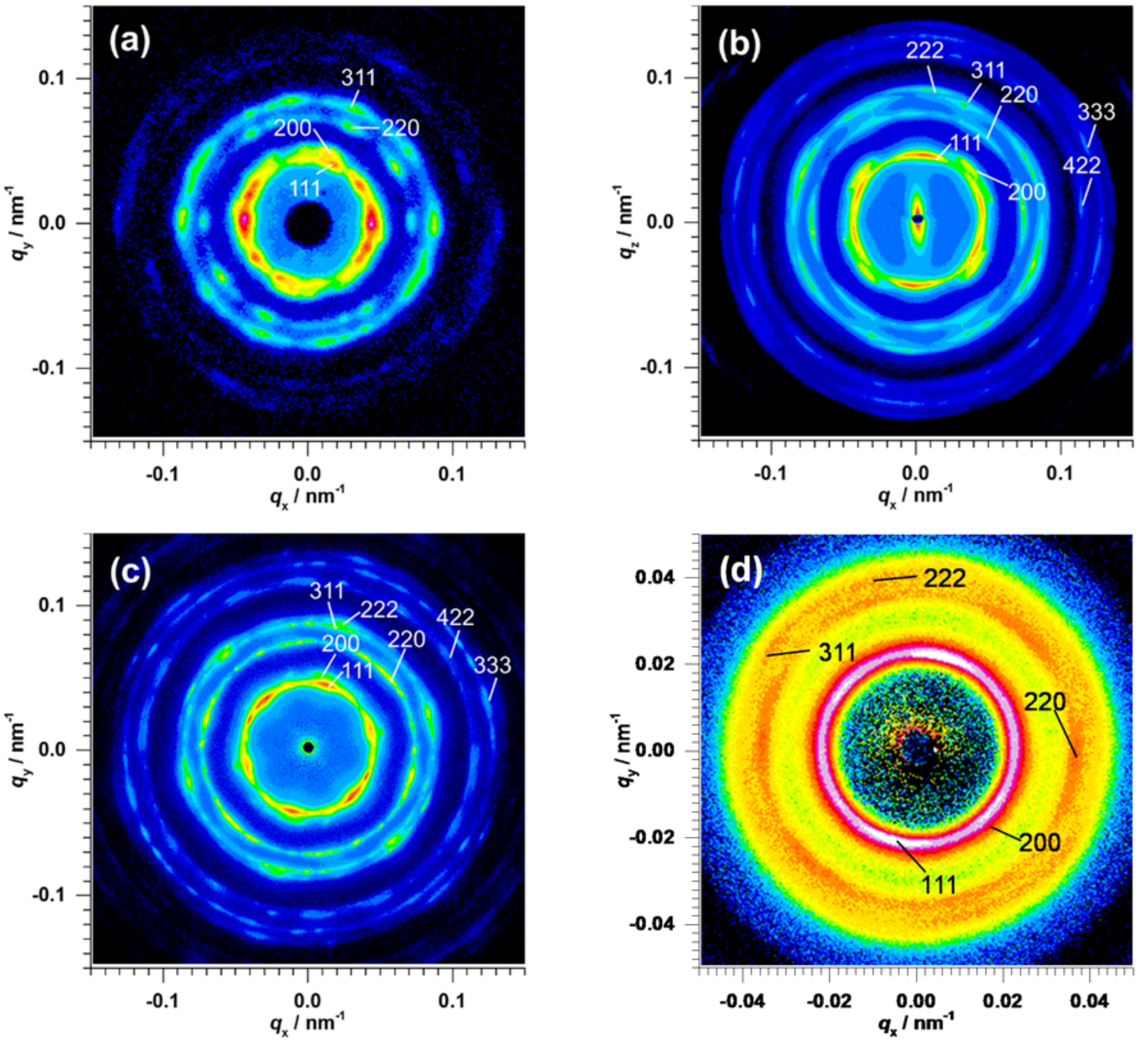

Figure 4-4. 2D USAXS image of (a) P1-55, (b) P2-75 from the edge view, (c) P2-75 from the through view, and (d) P3-30.

respectively, which were lower than the presumed value. According to these comparison, the main structure of these samples was determined as rhcp. Figure 4-3(d) shows 1D USAXS intensity profiles of P1-50, P2-35, and P2-40, as well as P1-45 and P2-30. Due to the same reason for P1-45 and P2-30, the main structure of P1-50, P2-35, and P2-40 was also decided as rhcp. Figure 4-3(c) shows a 2D USAXS image of P3-05. These diffraction peaks were well fitted as those of *hk*0 or 00*l* in the description of the Miller index for the hcp-type lattice. The diffraction patterns of *hkl* (except *hk*0 or 00*l*) that should a ppear for the hcp were not observed. Therefore, the crystal structure of P3-05 was determined as rhcp. Figure 4-4(a) and (d) shows 2D USAXS images of P1-55 and P3-30, respectively. All diffraction peaks were well fitted as those for the fcc-type lattice, which means that the structure of P1-55 and P3-30 was determined as fcc. Figure 4-4(b) and (c) shows the 2D USAXS images from the edge and through-views of P2-75. High-quality diffraction patterns were obtained, especially for the edge-view data, assuming the fcc with the (111) lattice plane parallel to the cast substrate.[48] Good correlation between them was confirmed. One of characteristic diffraction patterns for the fcc is from (200) lattice plane, which was observed clearly in both USAXS images from the edge view. In addition, some diffraction peaks in the through-view data were assigned to the fcc, as shown along with the Miller index in the figure. Indeed,

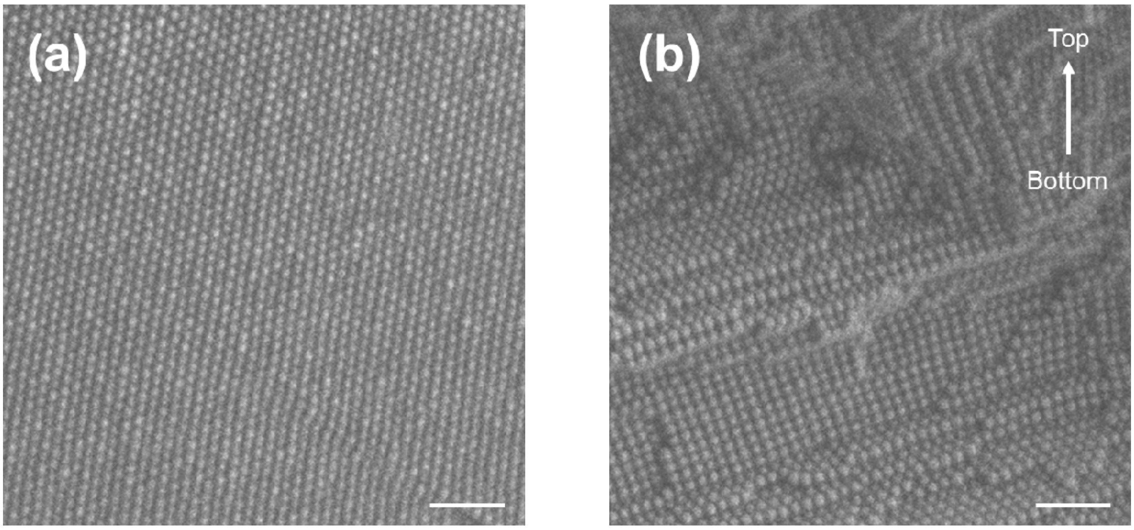

Figure 4-5. (a) The surface and (b) the cross-sectional FE-SEM image of P2-75. The scale bar indicates 1 μm.

the surface and cross-sectional FE-SEM image of P2-75 as shown in Figure 4-5 revealed that PSiPs were regularly stacked as fcc. Figure 4-6(a)–(c) show the 1D profiles of P1-55 to P1-70, P2-45 to P2-75, and P3-07 to P3-30, respectively. These diffraction patterns were also assigned to fcc-type lattice, therefore, the structure of P1-55 to P1-70, P2-45 to P2-75, and P3-07 to P3-30 were determined as fcc. The particle number density *n* was estimated by:

$$n = \frac{f_0/w_0}{f_0/\rho_0 + f_\mathrm{b}/\rho_\mathrm{b} + (1 - f_\mathrm{PSiP})/\rho_\mathrm{IL}} \tag{4-6}$$

$$f_0 = \frac{f_\mathrm{PSiP}}{1 + A_\mathrm{g}} \tag{4-7}$$

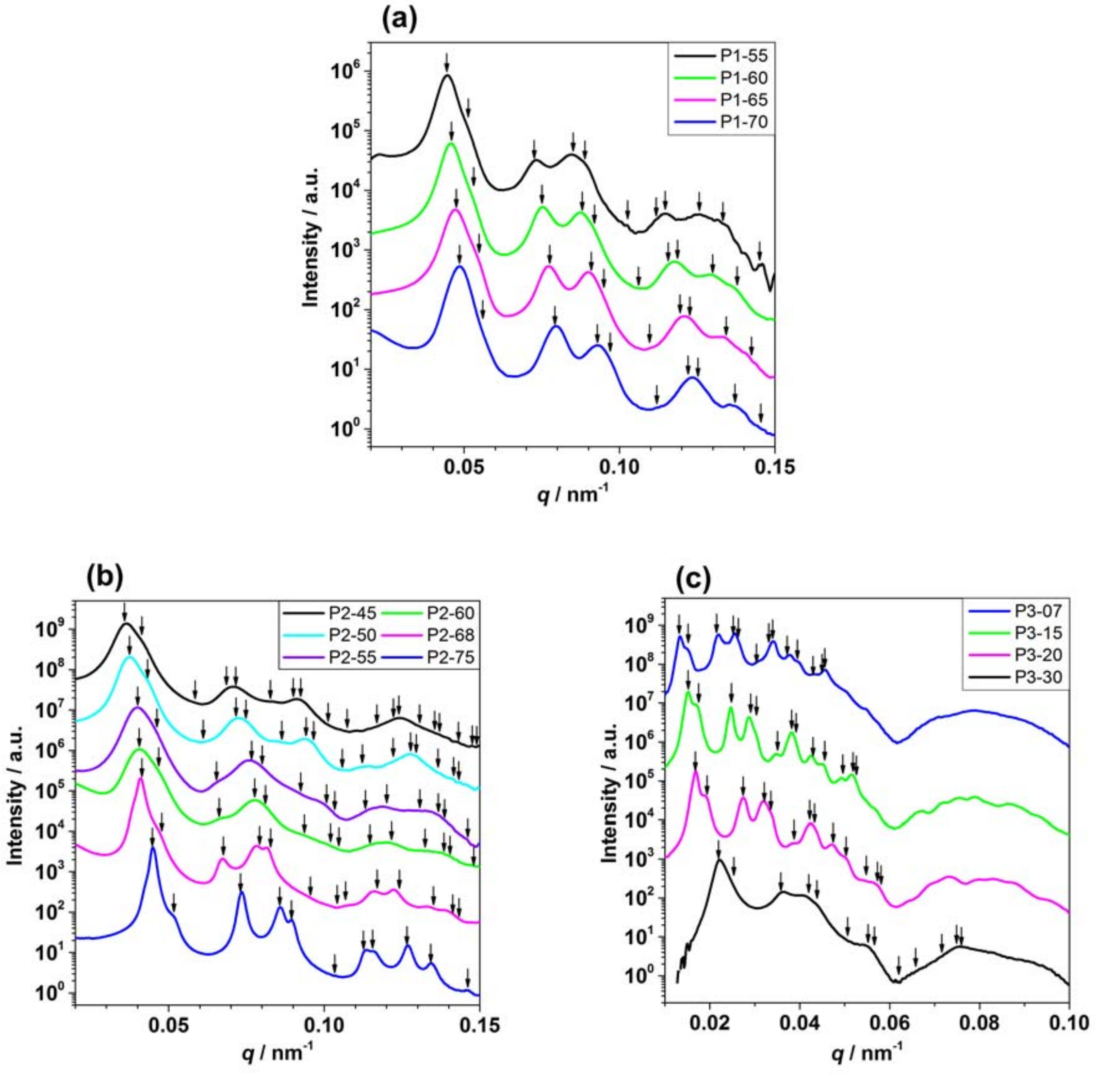

Figure 4-6. 1D USAXS profiles of (a) P1-55 to P1-70, (b) P2-45 to P2-75, and (c) P3-07 to P3-30.

$$f_{\mathrm{b}} = \frac{A_{\mathrm{g}} f_{\mathrm{PSiP}}}{1 + A_{\mathrm{g}}} \tag{4-8}$$

$$w_0 = \frac{4\pi \rho_0 {r_0}^3}{3} \tag{4-9}$$

where f_0, f_{b}, and f_{PSiP} are the weight fraction of the silica-core part, polymer-brush part, and PSiP in the composite, respectively; w_0 is the weight of the silica-core particle; ρ_0, ρ_{b}, and ρ_{IL} are the bulk densities of silica core (2.0), polymer brush (1.18), and IL (1.42), respectively.

During the formation of these higher-order structures, any exudation of IL, i.e., any macroscopic phase separation of the colloidal crystal domain and IL, was not observed. In addition, the center-to-center distance D_{dis} between neighboring particles was estimated from the USAXS data ($D_{\mathrm{dis,diff}}$) and the feed particle concentration ($D_{\mathrm{dis.feed}}$) for the close-packed structures using eq (2-17) and (2-18). $D_{\mathrm{dis,diff}}$ was determined using the averaged value of q_{110} for rhcp or q_{220} for fcc and was confirmed to be equal in an experimental error with that obtained from q_{100} or q_{111}, respectively. Figure 4-7 shows the relationship between $D_{\mathrm{dis,diff}}$ and $D_{\mathrm{dis,deed}}$, which suggests that $D_{\mathrm{dis,diff}}$ was approximately equal to $D_{\mathrm{dis.feed}}$. This result indicates that a homogenous composite of PSiP and IL was successfully prepared and that the colloidal crystal was characterized as the main component, based on the USAXS data.

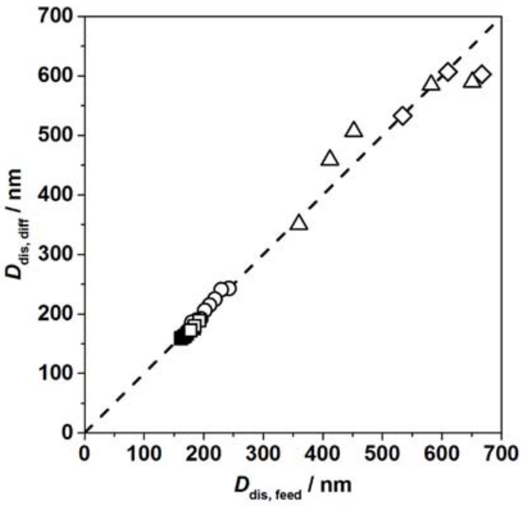

Figure 4-7. Relationship of the center-to-center distance D_{dis} between neighboring particles was estimated from the USAXS data ($D_{\mathrm{dis,diff}}$) and the feed particle concentration ($D_{\mathrm{dis.feed}}$).

Figure 4-8 shows the identified structures as a function of the type and chain length of polymer brushes and the particle number density. In order to describe clearly, the particle number density were normalized at the most compressed situation, of which the graft density of polymer brush is set to be 0.35 chains/nm^2 of PMMA. At low concentrations, the systems are in a liquid/disordered state. Here, a liquid state means that one can observe a flow in a certain time. An ordered arrangement arises at a particular (threshold) concentration. For the PSiP with larger molecular weight, i.e., larger size, the ordering occurs at a lower concentration, and the threshold is close to the separately determined concentration at equilibrium crystallization, understood by Kirkwood–Alder transition. According to the analysis, the brush-component of PSiP has no relationship for the structure formation, which means that the structure formation is entropy-driven, determined by interparticle potential of PSiP. Interestingly, PSiP gave an rhcp structure in the CPB system and a body-centered-cubic (bcc) structure in the softer SDPB system. As particle concentration became higher, the pressure in the system is considered to be

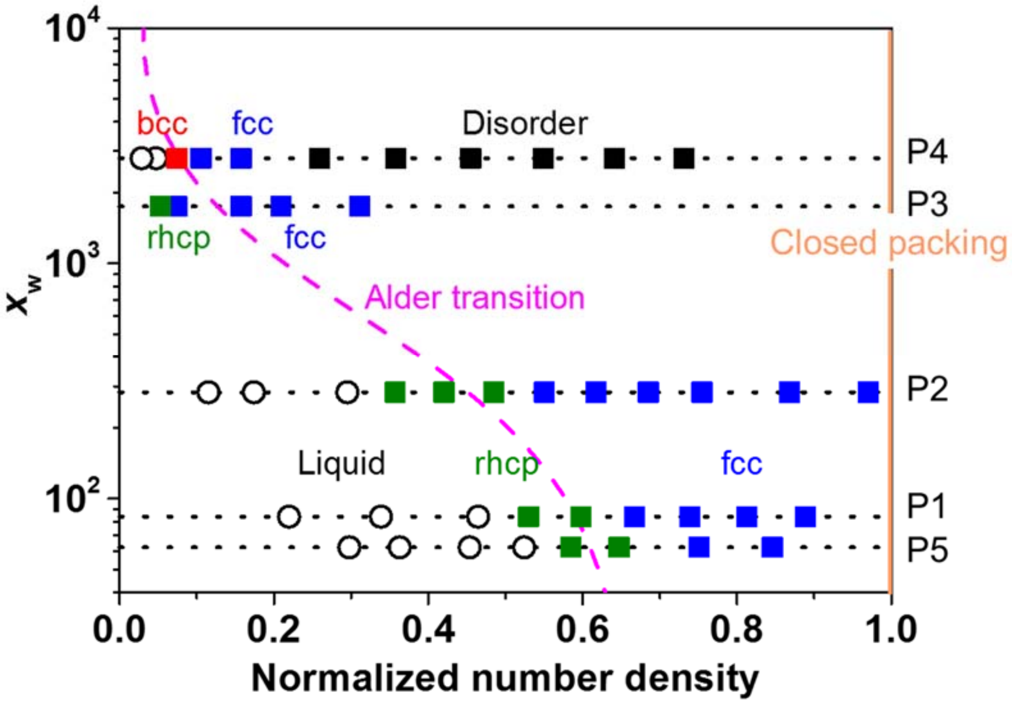

Figure 4-8. The identified structures as a function of the type and chain length of polymer brushes and the number density of PSiP normalized by the one of compact-closed packing.

higher, which results in the compression and deformation of polymer brush on nanoparticles, inducing the structure change from rhcp to fcc in CPB system, while the interpenetration among polymer brush on nanoparticles is considered to result in interrupting the formation of crystal in SDPB system. If particles with and without the compression and deformation are defined as “soft” and “hard” type particles, respectively, the interparticle potential of PSiPs presumes to become softer when particle concentration and brush length increases.

4-4. Conclusion

I analyzed higher-order structures of polymer-brush-modified nanoparticles in IL as a function of chain length of polymer brushes and the particle concentrations. According to the analysis, the following contents were revealed: (i) the structure formation is entropy-driven, not related to the brush component, (ii) the crystallization of PSiPs can be explained by Kirkwood–Alder transition, especially rhcp structure appears in CPB regime, (iii) interparticle potential is considered to become softer as the particle concentration is higher and the chain length of polymer brush is longer, which mean unified explanation of the structure formation of repulsive colloidal crystals.

References

1. K. Matyjaszewski. *Macromolecules* **2012**, *45*, 4015–4039.

2. M. Ouchi, T. Terashima, M. Sawamoto. *Chem. Rev.* **2009**, *109*, 4963–5050.

3. E. Rizzardo, D. H. Solomon. *Aust. J. Chem.* **2012**, *65*, 945–969.

4. G. Moad, E. Rizzardo, S. H. Thang. *Aust. J. Chem.* **2012**, *65*, 985–1076.

5. S. Yamago. *Chem. Rev.* **2009**, *109*, 5051–5068.

6. T. Fukuda, A. Goto, K. Ohno. *Macromol. Rapid Comm.* **2000**, *21*, 151–165.

7. C. Boyer, N. A. Corrigan, K. Jung, D. Nguyen, T. K. Nguyen, N. N. M. Adnan, S. Oliver, S. Shanmugam, J. Yeow. *Chem. Rev.* **2016**, *116*, 1803–1949.

8. Y. Tsujii, K. Ohno, S. Yamamoto, A. Goto, T. Fukuda. *Adv. Polym. Sci.* **2006**, *197*, 1–45.

9. M. Kobayashi, Y. Terayama, M. Kikuchi, A. Takahara. *Soft Matter* **2013**, *9*, 5138–5148.

10. R. Barbey, L. Lavanant, D. Paripovic, N. Schuwer, C. Sugnaux, S. Tugulu, H. A. Klok. *Chem. Rev.* **2009**, *109*, 5437–5527.

11. M. Ejaz, S. Yamamoto, K. Ohno, Y. Tsujii, T. Fukuda. *Macromolecules* **1998**, *31*, 5934–5936.

12. S. Yamamoto, M. Ejaz, Y. Tsujii, M. Matsumoto, T. Fukuda. *Macromolecules* **2000**, *33*, 5602–5607.

13. S. Yamamoto, M. Ejaz, Y. Tsujii, T. Fukuda. *Macromolecules* **2000**, *33*, 5608–5612.

14. A. Nomura, K. Ohno, T. Fukuda, T. Sato, Y. Tsujii. *Polym. Chem.* **2012**, *3*, 148–153.

15. C. Yoshikawa, A. Goto, Y. Tsujii, T. Fukuda, T. Kimura, K. Yamamoto, A. Kishida. *Macromolecules* **2006**, *39*, 2284–2290.

16. C. Yoshikawa, A. Goto, Y. Tsujii, N. Ishizuka, K. Nakanishi, T. Fukuda. *J. Polym. Sci., Part A: Polym. Chem.* **2007**, *45*, 4795–4803.

17. K. Ohno, T. Morinaga, S. Takeno, Y. Tsujii, T. Fukuda. *Macromolecules* **2006**, *39*, 1245–1249.

18. K. Ohno, T. Morinaga, S. Takeno, Y. Tsujii, T. Fukuda. *Macromolecules* **2007**, *40*, 9143–9150.

19. T. Morinaga, K. Ohno, Y. Tsujii, T. Fukuda. *Macromolecules* **2008**, *41*, 3620–3626.

20. T. Morinaga, K. Ohno, Y. Tsujii, T. Fukuda. *Eur. Polym. J.* **2007**, *43*, 243–248.

21. Y. Huang, T. Morinaga, Y. Tai, Y. Tsujii, K. Ohno. *Langmuir* **2014**, *30*, 7304–7312.

22. Y. Huang, A. Takata, Y. Tsujii, K. Ohno. *Langmuir* **2017**, *33*, 7130–7136.

23. W. K. Kegel, A. van Blaaderen. *Science* **2000**, *287*, 290–293.

24. P. N. Pusey, W. Vanmegen. *Nature* **1986**, *320*, 340–342.

25. W. Vanmegen, S. M. Underwood. *Nature* **1993**, *362*, 616–618.

26. A. Kose, S. Hachisu. *J. Colloid Interface Sci.* **1974**, *46*, 460–469.

27. Z. D. Cheng, W. B. Russell, P. M. Chaikin. *Nature* **1999**, *401*, 893–895.

28. J. X. Zhu, M. Li, R. Rogers, W. Meyer, R. H. Ottewill, W. B. Russell, P. M. Chaikin. *Nature* **1997**, *387*, 883–885.

29. S. Hachisu, Y. Kobayashi, A. Kose. *J. Colloid Interface Sci.* **1973**, *42*, 342–348.

30. S. Hachisu, K. Takano. *Adv. Colloid Interface Sci.* **1982**, *16*, 233–252.

31. I. S. Sogami, T. Yoshiyama. *Phase Transitions* **1990**, *21*, 171–182.

32. R. Williams, R. S. Crandall. *Phys. Lett. A* **1974**, *48*, 225–226.

33. N. A. Clark, A. J. Hurd, B. J. Ackerson. *Nature* **1979**, *281*, 57–60.

34. H. Yoshida, J. Yamanaka, T. Koga, N. Ise, T. Hashimoto. *Langmuir* **1998**, *14*, 569–574.

35. H. Yoshida, K. Ito, N. Ise. *Phys. Rev. B* **1991**, *44*, 435–438.

36. P. A. Hiltner, I. M. Krieger. *J. Phys. Chem.* **1969**, *73*, 2386–2389.

37. T. Okubo. *Prog. Polym. Sci.* **1993**, *18*, 481–517.

38. T. Sato, T. Morinaga, S. Marukane, T. Narutomi, T. Igarashi, Y. Kawano, K. Ohno, T. Fukuda, Y. Tsujii. *Adv. Mater.* **2011**, *23*, 4868–4872.

39. T. Morinaga, S. Honma, T. Ishizuka, T. Kamijo, T. Sato, Y. Tsujii. *Polymers* **2016**, *8*, 146.

40. T. Palberg. *J. Phys. Condens. Matter* **1999**, *11*, R323–R360.

41. T. Palberg. *J. Phys.: Condens. Matter* **2014**, *26*, 333101.

42. W. G. Hoover, F. H. Ree. *J. Chem. Phys.* **1967**, *47*, 4873–4878.

43. B. J. Alder, W. G. Hoover, D. A. Young. *J. Chem. Phys.* **1968**, *49*, 3688–3696.

44. P. N. Pusey, W. Vanmegen. *Phys. Rev. Lett.* **1987**, *59*, 2083–2086.

45. K. Ohno, T. Akashi, Y. Huang, Y. Tsujii. *Macromolecules* **2010**, *43*, 8805–8812.

46. Y. Huang, A. Takata, Y. Tsujii, K. Ohno. *Langmuir* **2017**, *33*, 7130 – 7136.

47. S. Forster, A. Timmann, M. Konrad, C. Schellbach, A. Meyer, S. S. Funari, P. Mulvaney, R. Knott. *J. Phys. Chem. B* **2005**, *109*, 1347–1360.

48. W. Loose, B. J. Ackerson. *J. Chem. Phys.* **1994**, *101*, 7211–7220.

Chapter 5

Understanding Dynamics of Self-Assembling of Polymer-brush-modified Nanoparticles/Ionic Liquid Composites by Shear Oscillation

5-1. Introduction

Well-defined and low-polydispersity polymers can be densely grown up on various solid surfaces by living radical polymerization[1-7] (LRP; also called controlled reversible-deactivation radical polymerization as per the IUPAC recommendation). The graft density in such cases is more than one order of magnitude higher than that of a typical “semi-dilute” polymer brush (SDPB), going deep into the “concentrated”-brush regime.[8-10] Graft chains of such a concentrated polymer brush (CPB) in a good solvent are highly extended, almost to their full lengths, because of the exceptionally high osmotic pressure of the brush.[8,11-13] Because of such a highly stretched conformation, CPB in a good solvent exhibits characteristics such as high resistance against compression, very less mutual interpenetration that gives rise to very high lubrication with an extremely low friction coefficient ($\mu \sim 10^{-4}$),[8,9,14] and definite size exclusion with a very low threshold of molecular weight that gives good biocompatibility in an aqueous system.[8,15,16]

Such highly repulsive and lubricating properties lead to a good dispersion of CPB-modified silica nanoparticles (PSiPs), thereby forming stable suspensions and colloidal crystals above a certain concentration. The obtained colloid crystals of PSiPs can be distinguished as a “semi-soft” type[17-21] in contrast to the previously reported “hard”[22-27] and “soft”[28-36] types which are formed by a hard-sphere and electrostatic interactions, respectively. Note that the above-mentioned semi-soft colloidal crystals can be formed even in an ionic liquid in which the electrostatic interactions are shielded. Different types of higher-order structures can be expected by varying the interparticle potential and particle concentration. For examples, there are typically three types of closed packing pattern: face-centered

cubic (fcc; ABC-stacking), hexagonal close packing (hcp; ABA-stacking), and random-hexagonal close packing (rhcp; random stacking). The difference lies in the way of stacking of the planes (A, B, or C), in which the colloids are hexagonally packed. Previous work by our group reported that PSiPs self-assemble in the rhcp structure in an organic solvent at the liquid/crystal-threshold concentration,[19] while they assemble in the fcc structure in an ionic liquid at a higher particle concentration.[37,38] Thermodynamic equilibrium was confirmed for the former but not for the latter. The latter focused on the application of such a self-assembled structure as a novel pseudo-solid electrolyte to a bipolar-type lithium-ion rechargeable battery. Therefore, a detailed and systematic study of the PSiP self-assembling process in an ionic liquid as a function of particle concentration should be carried out not only to further understand the basics of colloid science but also to develop highly functionalized devices.

This chapter discusses the oscillation-induced self-assembling of PSiP based on the above discussion, in addition, in order to control not only the structure but also the orientation for the application on functional materials such as electrolytes for devices. The structure control results in the functional development of materials, so many researchers are interested in the structure dynamics of self-assembling. To achieve in controlling the structure and orientation of materials to obtain the designable properties, various processes including shear oscilattion,[39,40] dip-coating, drop-coating, wire-coating, and spin-coating have been used in recent years.[41-43] In this study, we carried out time-resolved ultra-small-angle X-ray scattering (USAXS) measurements to analyze the higher-order structure of the composites of polymer-brush-modified nanoparticles and ionic liquid as well as the process of the structure formation.

5-2. Experimental section

5-2-1. Materials

N,*N*-Diethyl-*N*-(2-methacryloylethyl)-*N*-methylammonium bis(trifluoromethylsulfonyl) imide (DEMM-TFSI) was obtained from Toyo Gosei Co., Ltd., Tokyo, Japan. Silica particle (SiP)

(SEAHOSTER KE-E10, 20 wt% suspension of SiP in ethylene glycol) was kindly donated by Nippon Shokubai Co., Ltd., Osaka, Japan. *N*,*N*-diethyl-*N*-(2-methoxyethyl) ammonium bis(trifluoromethane sulfonyl) imide (DEME-TFSI; Kanto Chemical Co., Inc., Japan) and acetonitrile (Kanto Chemical, 99.5%), were used as received. An atom transfer radical polymerization (ATRP)-initiator-holding silane coupling agent, (2-bromo-2-methyl)propionyloxypropyltriethoxysilane (BPE), was synthesized as reported previously.[44]

5-2-2. Preparation of PSiP/IL composites

The concentrated-polymer-brush-afforded hybrid silica nanoparticles (PSiPs) were synthesized as the mentioned in Chapter 2. They had the SiP core and a shell of P(DEMM-TFSI) chains with number-average molecular weight $M_n = 27800$, weight-average molecular weight $M_w = 29900$ and polydispersity index $M_w/M_n = 1.08$, the weight of the grafted polymer in comparison to the SiP-core weight $A_g = 0.13$, end-grafted on the SiP surface with graft density and surface occupancy as high as 0.14 chain/nm^2 and 32%, respectively. A suspension of PSiP in acetonitrile was mixed with DEME-TFSI in the composite; to this solution, acetonitrile was added to adjust its concentration to 60 wt% in the solution. Then, the prepared solutions were cast by slowly evaporating acetonitrile for 12 h, followed by drying it in a vacuum oven at 90 °C for 24 h to obtain PSiP/IL composites. Then, the composites was transferred onto cover glass (Paul Marienfeld KG, Bad Mergentheim, Germany, thickness was 0.12–0.17 mm) using liquid nitrogen. The weight fractions of PSiP in the composite (f_{PSiP}) was 60 wt%.

5-2-3. Measurements

Ultra-small-angle X-ray scattering (USAXS) measurement was performed at the beamlines BL19B2 in SPring-8 (Harima, Hyogo, Japan). The USAXS profiles were obtained on a two-dimensional hybrid pixel array detector, PILATUS 2M with 3 × 6 modules (DECTRIS Ltd.) and 1475 × 1679 pixels of 172 μm pixel size. The X-ray wavelength (λ), the sample-to-detector distance, and the X-ray beam size at the sample position (horizontal × vertical) were 0.0689 nm, 41523 mm, and 300 μm × 100 μm, respectively. The scattered intensities are expressed as a function of the scattering vector, $q = (4\pi \sin\theta)/\lambda$, where 2θ is the scattering angle relative to the incident beam. The q value was calibrated using a collagen fiber extracted from a chicken leg. Shear oscillation conditions were controlled by a CSS-450 high-temperature shearing stage (Linkam Scientific Instruments Ltd., UK). The sample gap was 200 μm. The strain oscillation were produced at a strain γ=0 to 400% and frequency ω=0 to 2 Hz. Time-resolved USAXS measurements were conducted per 24 to 25 seconds with 15 seconds exposure on the detector. After shear oscillation, USAXS measurements were also carried out with 1 min exposure.

5-3. Results and Discussion

According to the discussion in Chapter 2, the cast membrane of this concentration was formed as random hexagonal close packing (rhcp). In this work, the diffraction patterns were observed by the regularly-arrayed structures of PSiP. Figure 5-1 and 5-2(a) show 2D USAXS images and 1D USAXS intensity profiles circular-averaged over all azimuthal angles of each shear oscillation, respectively. Considering various conditions of shear oscillation, the diffraction pattern was disappeared with γ=200% and ω=2 Hz. which is considered to be the disordering operation to delete the preparation history. The

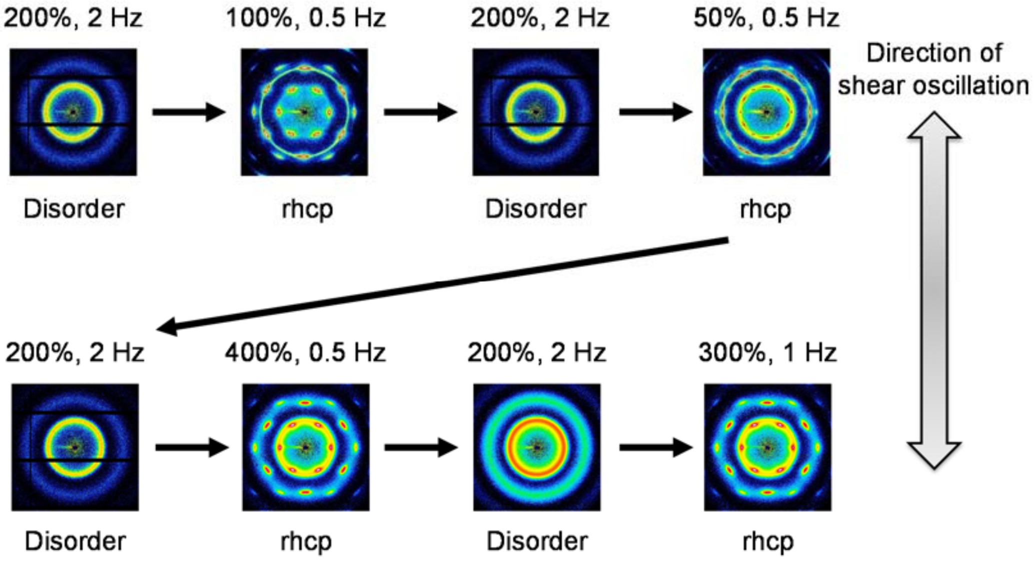

Figure 5-1. 2D USAXS images of PSiP/IL composites after shear oscillation.

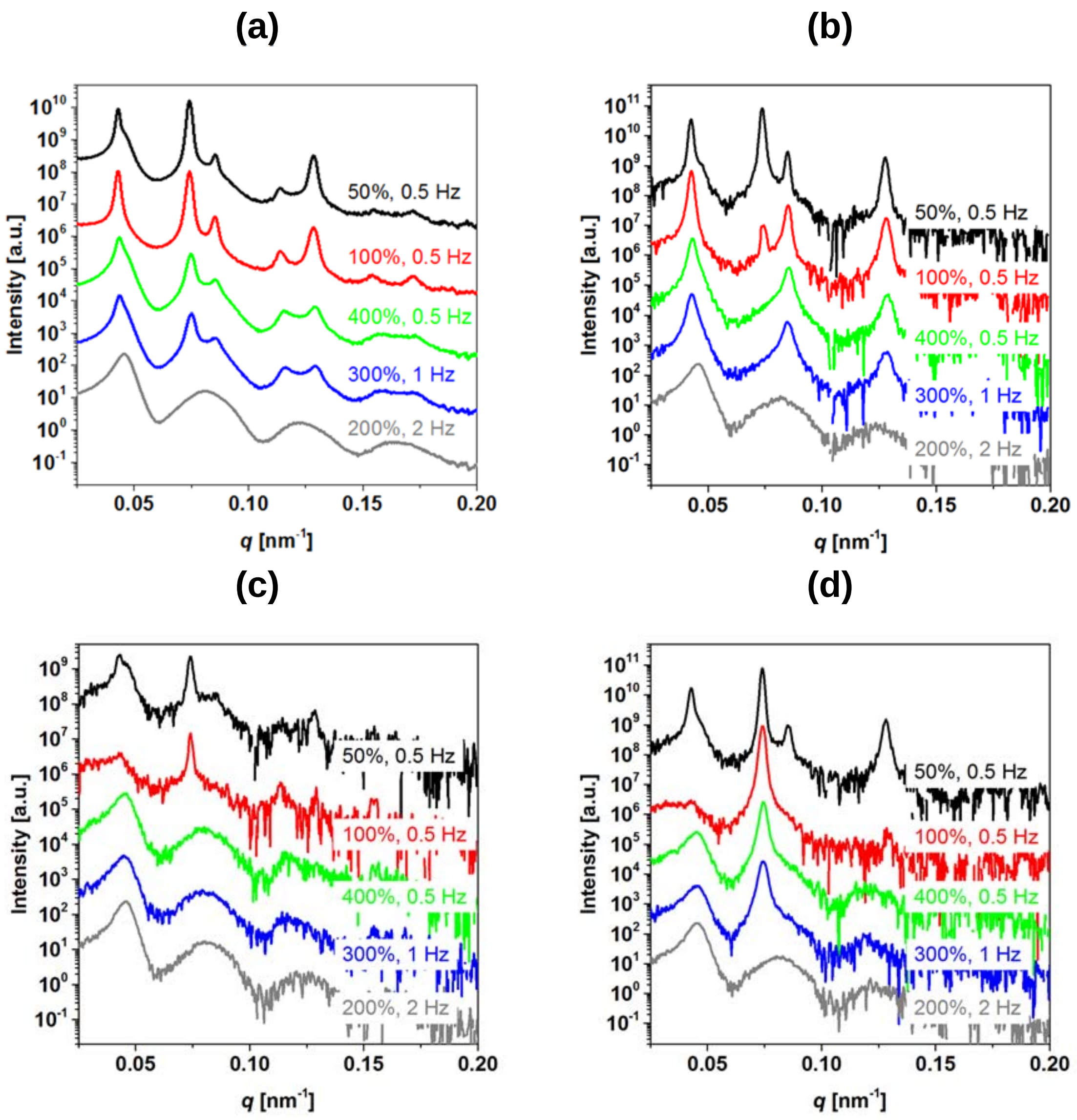

Figure 5-2. 1D USAXS intensity profiles of PSiP/IL composites after shear oscillation: (a) circular-averaged over all azimuthal angles and (b)(c)(d) at the azimuthal angle of (b) 0°, (c) 15°, and (c) 30°.

USAXS patterns for disorder remained after the shear oscillation, which suggests that a strong shear oscillation made PSiP/IL composites form a "semi" stable state of the disorder structure. Shear condition 1 (γ=100%, ω=0.5 Hz), condition 2 (γ=50%, ω=0.5 Hz), condition 3 (γ=400%, ω=0.5 Hz), or condition 4 (γ=300%, ω=1 Hz) were carried out for 10 minutes after the disordering operation between each conditions. The scattered images before and after stopping shear oscillation were approximately same, and even after several tens of minutes the scattered images of each condition didn't change remarkably. These results indicate that regularly-arrayed structure of PSiP can be formed by suitable shear oscillation and the process of structural formation can be observed by time-resolved USAXS measurement. The diffraction peaks were observed at q values of the q/q^*ratio of approximately 1:√3:√4, assigned to be (*hk*0) plane of the *hexagonal system* (hcp-type lattice). Considering the structure of the cast membrane at the approximately same PSiP concentration in Chapter 2, these crystal structures were determined as rhcp. The center-to-center distance D_{dis} between neighboring particles was estimated from the USAXS data ($D_{\mathrm{dis,diff}}$) for the close-packed structures according to the following equations:

$$D_{\mathrm{dis,diff}} = \frac{4\sqrt{3}\pi}{3q_{100}} = \frac{4\pi}{q_{110}} \qquad (5\text{-}1)$$

where, q_{hkl} is the peak value of the diffraction from the (*hkl*) plane of hcp-type lattice. According to eq (5-1), the value of D_{dis} from these diffraction patterns in Figure 5-1 were 168–169 nm, which was approximately equal to $D_{\mathrm{dis,diff}}$ from the diffraction pattern of the cast membrane with the same PSiP concentration, 172 nm. Also using eq (2-18), the value of $D_{\mathrm{dis.feed}}$ from the feed particle concentration was estimated to be 175 nm, which was approximately equal to the value of $D_{\mathrm{dis,diff}}$ as well. These results indicate that a homogenous composite of PSiP and IL was successfully prepared and that the colloidal crystal was characterized as the main component, based on the USAXS data. Analyzing these diffraction pattern indicates that the close packed plane of PSiP was parallel to the substrate of cover glass, and PSiP arrayed along the direction of shear oscillation described as Figure 5-3. However, the diffraction pattern of shear condition 2 (γ=50%, ω=0.5 Hz) was different from the others, the detail study is ongoing.

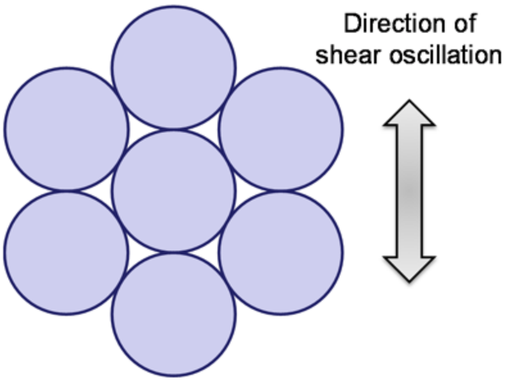

Figure 5-3. Schematic illustration of PSiP ordering by shear oscillation.

In order to discuss the crystal structure more in detail in terms of crystallinity, analyze the USAXS intensity profiles at specified azimuthal angles φ, as shown in Figure 5-2(a)–(c). If PSiPs are perfectly oriented as Figure 5-3, the USAXS intensity profile at $\varphi = 15°$ doesn't include any diffraction peaks. On the other hand, if PSiP sample includes amorphous component, the pattern derived from disorder is observed, in some cases, the shoulder appears at the right side of the first peak position (q_{100}). In the case of shear condition 1 (γ=100%, ω=0.5 Hz), the USAXS profile of shear condition 1 (γ=100%, ω=0.5 Hz) at $\varphi = 15°$ and 30° have less peak intensity at the first peak position, and all peaks derived from the crystal structure were clearly observed in the USAXS profile at each specified azimuthal angle, especially the peak of (110) plane of the hcp-type lattice, which indicates that though the orientation was partially disordered, the sample of shear condition 1 had extremely high crystallinity. In the case of shear condition 2, 3 and 4, the peak derived from amorphous was observed, which suggests that the too weak or strong shear oscillation to order PSiPs resulted in including the amorphous structure.

To characterize the degree of order observed in the normalized scattering patterns as a function of azimuthal angle φ, the integrated intensity over an annular region at a given q was calculated with the use of the "alignment factor" (A_{f}) as follows:[39,45]

$$A_{\mathrm{f}}(q) = \frac{\int_0^{2\pi} I(q,\varphi)\cos(n\varphi - \beta)\, d\varphi}{\int_0^{2\pi} I(q,\varphi) d\varphi} \tag{5-2}$$

where n is an integer indicating the symmetry of order and β is the angle of alignment relative to the flow. As defined here with the choice of an appropriate for each order symmetry, the absolute value of A_{f} can range from 0 to 1 meaning complete disorder or complete order, respectively. Figure 5-4 shows alignment factors at q_{110} of PSiP/IL composites, which indicates that crystallization and extremely highly orientation of PSiP by shear oscillation was completed within about 200 seconds, and the crystal structure remained after the shear oscillation. The value of Af didn't reach maximum (= 1.0), caused by including amorphous or less-ordered structures partially. The initial slope in Figure 5-4 means the speed of the crystal formation of PSiP, showing no significant difference among the shear condition. As an

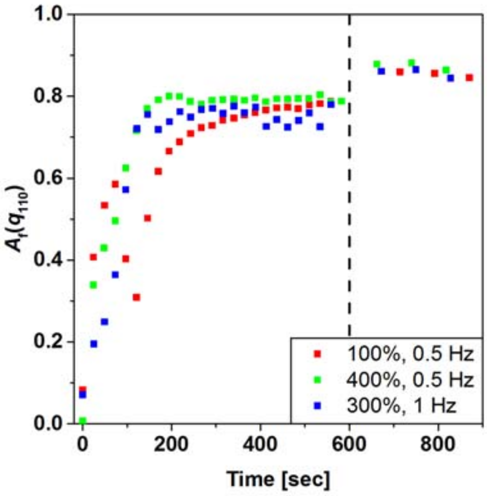

Figure 5-4. Alignment factors at q_{110} for shear ordered PSiP/IL composites on shear condition 1, 3, and 4. The shear oscillation was carried out in 600 sec.

example of the research on soft-type colloidal crystals using shear oscillation, oscillatory-shear-induced silica particles in toluene/ethanol suspension was enumerated.[40] In this system, a stable structure was fcc because of the soft-type, however, a certain shear-oscillation made particles form rhcp as well as fcc. Compared with this work using PSiP, the speed of structural formation of PSiP/IL composites was as fast as the one of the reference work using silica particles despite extremely high viscosity and particle concentration. This is considered to be significant property derived from the elasticity and low friction of PSiP. It suggests that shear oscillation increases the motions of colloidal particles, getting higher energy to overcome the potential capacity wall and to form more stable structure. And much more shear oscillation made particles form a normally unstable state, which means the disorder operation. According to above discussion, the potential for structural formation in each system can be illustrated as Figure 5-5. In PSiP system, it is possible to say that a suitable shear oscillation induces high-arrayed rhcp structure because there is little difference between fcc and hcp structure. On the other hand, in soft-type colloidal system, it may be interpreted as follows: the most customarily stable structure is fcc, however, shear oscillation induces particles to form customarily unstable structure such as rhcp and amorphous structure.

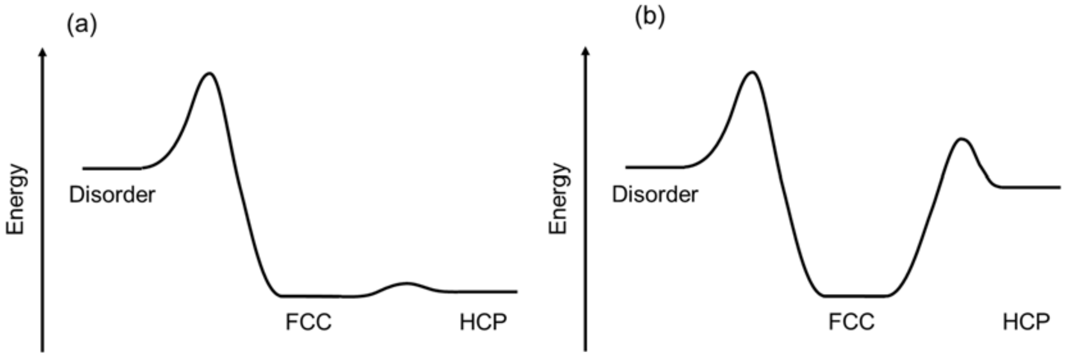

Figure 5-5. Schematic illustration of energy diagram of structural formation for (a) PSiP-type and (b) soft-type colloidal particles.

5-4. Conclusion

I analyzed the shear-induced structure formation and dynamics of CPB-modified nanoparticles with IL in various shear oscillation using time-resolved USAXS. The shear-induced crystal structure was extremely arrayed, assumed to be rhcp. The speed of shear-induced structure formation of PSiP was as fast as that of soft-type colloidal particles in spite of high viscosity and particle concentration. This achievement is considered to be caused by the high elasticity of the swollen CPBs in IL as a good solvent. This work can result in the development of functional materials using PSiP applied to electronic devices.

References

1. K. Matyjaszewski. *Macromolecules* **2012**, *45*, 4015–4039.

2. M. Ouchi, T. Terashima, M. Sawamoto. *Chem. Rev.* **2009**, *109*, 4963–5050.

3. E. Rizzardo, D. H. Solomon. *Aust. J. Chem.* **2012**, *65*, 945–969.

4. G. Moad, E. Rizzardo, S. H. Thang. *Aust. J. Chem.* **2012**, *65*, 985–1076.

5. S. Yamago. *Chem. Rev.* **2009**, *109*, 5051–5068.

6. T. Fukuda, A. Goto, K. Ohno. *Macromol. Rapid Comm.* **2000**, *21*, 151–165.

7. C. Boyer, N. A. Corrigan, K. Jung, D. Nguyen, T. K. Nguyen, N. N. M. Adnan, S. Oliver, S. Shanmugam, J. Yeow. *Chem. Rev.* **2016**, *116*, 1803–1949.

8. Y. Tsujii, K. Ohno, S. Yamamoto, A. Goto, T. Fukuda. *Adv. Polym. Sci.* **2006**, *197*, 1–45.

9. M. Kobayashi, Y. Terayama, M. Kikuchi, A. Takahara. *Soft Matter* **2013**, *9*, 5138–5148.

10. R. Barbey, L. Lavanant, D. Paripovic, N. Schuwer, C. Sugnaux, S. Tugulu, H. A. Klok. *Chem. Rev.* **2009**, *109*, 5437–5527.

11. M. Ejaz, S. Yamamoto, K. Ohno, Y. Tsujii, T. Fukuda. *Macromolecules* **1998**, *31*, 5934–5936.

12. S. Yamamoto, M. Ejaz, Y. Tsujii, M. Matsumoto, T. Fukuda. *Macromolecules* **2000**, *33*, 5602–5607.

13. S. Yamamoto, M. Ejaz, Y. Tsujii, T. Fukuda. *Macromolecules* **2000**, *33*, 5608–5612.

14. A. Nomura, K. Ohno, T. Fukuda, T. Sato, Y. Tsujii. *Polym. Chem.* **2012**, *3*, 148–153.

15. C. Yoshikawa, A. Goto, Y. Tsujii, T. Fukuda, T. Kimura, K. Yamamoto, A. Kishida. *Macromolecules* **2006**, *39*, 2284–2290.

16. C. Yoshikawa, A. Goto, Y. Tsujii, N. Ishizuka, K. Nakanishi, T. Fukuda. *J. Polym. Sci., Part A: Polym. Chem.* **2007**, *45*, 4795–4803.

17. K. Ohno, T. Morinaga, S. Takeno, Y. Tsujii, T. Fukuda. *Macromolecules* **2006**, *39*, 1245–1249.

18. K. Ohno, T. Morinaga, S. Takeno, Y. Tsujii, T. Fukuda. *Macromolecules* **2007**, *40*, 9143–9150.

19. T. Morinaga, K. Ohno, Y. Tsujii, T. Fukuda. *Macromolecules* **2008**, *41*, 3620–3626.

20. T. Morinaga, K. Ohno, Y. Tsujii, T. Fukuda. *Eur. Polym. J.* **2007**, *43*, 243–248.

21. Y. Huang, T. Morinaga, Y. Tai, Y. Tsujii, K. Ohno. *Langmuir* **2014**, *30*, 7304–7312.

22. W. K. Kegel, A. van Blaaderen. *Science* **2000**, *287*, 290–293.

23. P. N. Pusey, W. Vanmegen. *Nature* **1986**, *320*, 340–342.

24. W. Vanmegen, S. M. Underwood. *Nature* **1993**, *362*, 616–618.

25. A. Kose, S. Hachisu. *J. Colloid Interface Sci.* **1974**, *46*, 460–469.

26. Z. D. Cheng, W. B. Russell, P. M. Chaikin. *Nature* **1999**, *401*, 893–895.

27. J. X. Zhu, M. Li, R. Rogers, W. Meyer, R. H. Ottewill, W. B. Russell, P. M. Chaikin. *Nature* **1997**, *387*, 883–885.

28. S. Hachisu, Y. Kobayashi, A. Kose. *J. Colloid Interface Sci.* **1973**, *42*, 342–348.

29. S. Hachisu, K. Takano. *Adv. Colloid Interface Sci.* **1982**, *16*, 233–252.

30. I. S. Sogami, T. Yoshiyama. *Phase Transitions* **1990**, *21*, 171–182.

31. R. Williams, R. S. Crandall. *Phys. Lett. A* **1974**, *48*, 225–226.

32. N. A. Clark, A. J. Hurd, B. J. Ackerson. *Nature* **1979**, *281*, 57–60.

33. H. Yoshida, J. Yamanaka, T. Koga, N. Ise, T. Hashimoto. *Langmuir* **1998**, *14*, 569–574.

34. H. Yoshida, K. Ito, N. Ise. *Phys. Rev. B* **1991**, *44*, 435–438.

35. P. A. Hiltner, I. M. Krieger. *J. Phys. Chem.* **1969**, *73*, 2386–2389.

36. T. Okubo. *Prog. Polym. Sci.* **1993**, *18*, 481–517.

37. T. Sato, T. Morinaga, S. Marukane, T. Narutomi, T. Igarashi, Y. Kawano, K. Ohno, T. Fukuda, Y. Tsujii. *Adv. Mater.* **2011**, *23*, 4868–4872.

38. T. Morinaga, S. Honma, T. Ishizuka, T. Kamijo, T. Sato, Y. Tsujii. *Polymers* **2016**, *8*, 146.

39. J. M. McMullan, N. J. Wagner. *J. Rheol.* **2009**, *53*, 575–588.

40. Y. D. Yan, J. K. G. Dhont, C. Smits, H. N. W. Lekkerkerker. *Physica A* **1994**, *202*, 68–80.

41. H. Ogawa, M. Takenaka, T. Miyazaki, A. Fujiwara, B. Lee, K. Shimokita, E. Nishibori, M. Takata. *Macromolecules* **2016**, *49*, 3471–3477.

42. S. Watanabe, K. Inukai, S. Mizuta, M. T. Miyahara. *Langmuir* **2009**, *25*, 7287‑7295.

43. N. Vogel, M. Retsch, C. A. Fustin, A. del Campo, U. Jonas. *Chem. Rev.* **2015**, *115*, 6265–6311.

44. K. Ohno, T. Akashi, Y. Huang, Y. Tsujii. *Macromolecules* **2010**, *43*, 8805–8812.

45. L. M. Walker, N. J. Wagner. *Macromolecules* **1996**, *29*, 2298–2301.

Chapter 6

Understanding Dynamics of Self-Assembling of Polymer-Brush-Modified Nanoparticles/Ionic Liquid Composites by Dip-coating Method

6-1. Introduction

Colloidal particles are applied to optical,[1-4] chemical and bio-sensing,[5,6] data storage, and photonic band gap materials.[7] The structure control results in the functional development of materials, so many researchers are interested in the structure dynamics of self-assembling. To achieve in controlling the structure and orientation of materials to obtain the designable properties, various processes including dip-coating, drop-coating, wire-coating, and spin-coating have been used in recent years.[8-10] Most predominantly, direct assembly methods take advantage of solvent evaporation to control the deposition of colloids. Such techniques are usually referred to as convective assemblies and are based on the formation of a very thin liquid film in the meniscus region of at the three-point contact line. The dominating forces governing the crystallization mechanism are immersion capillary forces that push the particles together once the height of the liquid film falls below the colloid diameter.[11] Evaporation-induced deposition methods that rely on capillary forces require low particle-surface interactions so that particles can freely diffuse across the substrate, seeking their lowest energy configuration. Among such methods, the dip-coating method was introduced to form homogeneous, well-ordered monolayers over larger areas.[12]

In Chapter 2, the self-assembling of concentrated-polymer-brush (CPB)-modified nanoparticle (PSiP) in ionic liquid (IL) in various range of particle concentration was discussed. In this chapter, in order to observe the self-assembly process as well as to control the alignment of structures of the composites of polymer-brush-modified nanoparticles (PSiPs) with ionic liquid (IL), the *in situ* observation of dip-coating of PSiPs was carried out using ultra-small-angle X-ray scattering (USAXS) and X-ray absorption measurements. In addition, the structure analysis of dip-coated membrane was also carried out using Grazing-incidence small-angle X-ray scattering (GISAXS), which has been used for nanometer level structural analysis of thin organic and inorganic films.[13-20]

6-2. Experimental section

6-2-1. Materials

N,*N*-Diethyl-*N*-(2-methacryloylethyl)-*N*-methylammonium bis(trifluoromethylsulfonyl) imide (DEMM-TFSI) was obtained from Toyo Gosei Co., Ltd., Tokyo, Japan. Silica particle (SiP) (SEAHOSTER KE-E10, 20 wt % suspension of SiP in ethylene glycol) was kindly donated by Nippon Shokubai Co., Ltd., Osaka, Japan. The mean diameter of the SiP was 148 nm with a relative standard deviation of 10%, as measured by USAXS in Chapter 2. Acetonitrile (Kanto Chemical, 99.5%) and *N*,*N*-diethyl-*N*-(2-methoxyethyl) ammonium bis(trifluoromethane sulfonyl) imide (IL; Kanto Chemical Co., Inc., Japan) were used as received. Ultrathin quartz substrates (10 mm × 15 mm × 20 μm) were purchased from ATOCK Co., Ltd., Ibaraki, Japan.

6-2-2. Preparation of PSiP/IL composite membrane

The concentrated-polymer-brush-afforded hybrid silica nanoparticles (PSiPs) were synthesized as the mentioned in Chapter 2. They had the SiP core and a shell of P(DEMM-TFSI) chains with number-average molecular weight $M_n = 27800$, weight-average molecular weight $M_w = 29900$ and polydispersity index $M_w/M_n = 1.08$, the weight of the grafted polymer in comparison to the SiP-core weight $A_g = 0.17$, end-grafted on the SiP surface with graft density and surface occupancy as high as 0.19 chain/nm^2 and 42%, respectively. The PSiPs were dispersed in acetonitrile, and IL was mixed in the suspension. The weight composition of PSiP/IL/acetonitrile was 29.6/10.4/60. The PSiP/IL-mixed suspension was poured into the glass cell (the inside dimension was 4 mm × 15 mm × 10 mm) for dip-coating, and the PSiP/IL composite membrane was dip-coated on the quartz substrate. The speed of dip-coating was at first 5 μm/sec until the dip-coated distance reached 2 mm, after then 2 μm/sec. The obtained membrane was dried in vacuum oven at 90 ^{o}C for 12h.

6-2-3. USAXS and GISAXS measurement

USAXS and GISAXS measurement were performed at the beamlines, BL40B2 and BL03XU, in SPring-8 (Harima, Hyogo, Japan). The USAXS profiles were obtained on a complementary metal oxide semiconductor image sensor (CMOS) camera (C11440-22C; Hamamatsu Photonics, Shizuoka, Japan) coupled to an X-ray image intensifier system (V7735P; Hamamatsu Photonics) consisting of 2048 × 2048 pixels with a 43.1 μm pixel size at BL40B2. The GISAXS profiles were measured with a cooled charge-coupled device detector (CCD) (ORCA R2; Hamamatsu Photonics) coupled to an X-ray image intensifier (V7739P) consisting of 1344 × 1024 pixels with a 63 μm pixel size at BL03XU. The X-ray beam size at the sample position (horizontal × vertical) was 600 μm × 600 μm (BL40B2) and 112 μm × 100 μm (BL03XU). The X-ray wavelengths (λ) were 0.19074 nm (BL40B2) and 0.15 nm (BL03XU). The sample-to-detector distances were 4325 mm (BL40B2), and 2661 mm (BL03XU). The scattered intensities are expressed as a function of the scattering vector, $q = (4\pi \sin\theta)/\lambda$, where 2θ is the scattering angle relative to the incident beam. The q value was calibrated using a collagen fiber extracted from a chicken leg.

6-2-4. In situ USAXS and X-ray absorption measurement during dip-coating

In situ synchrotron radiation USAXS measurements of dip-coating was also performed at the beamline BL03XU. The set-up overview was shown in Figure 1-8. USAXS profiles from the through view were measured on a CCD (ORCA R2; Hamamatsu Photonics) coupled to an X-ray image intensifier (V7739P) consisting of 1344 × 1024 pixels with a 63 μm pixel size. The X-ray wavelength, the X-ray beam size at the sample position (H × V), and the sample-to-detector distance were 0.15 nm, 112 μm × 100 μm, and 2626 mm, respectively. Ionization chamber was set between the sample and the vacuum path in order to evaluate the X-ray absorption of the suspension containing of PSiP/IL composites. The exposure time and the time interval of the ion chamber as well as the CCD detector were 100 ms and 1 min, respectively.

6-2-5. High-precision dip-coater and dip-cell for in situ USAXS measurements

For *in situ* synchrotron radiation USAXS and X-ray absorption measurements on dip-coating process of PSiP/IL composites, we designed the measurement system with a dip-coater and dip-cell. The position of the dip-cell was being brought down from that of incidence X-ray during dip-coating process to prepare the PSiP/IL composite membrane. The detector and the ion-chamber started obtaining scattered images and measuring X-ray absorption when dip-coater began to be brought down. The dip-cell has half-circles whose diameters were 0.5 mm on the top edge to obtain scattered images through meniscus of PSiP/IL suspension.

6-2-6. SEM observations

Field-emission scanning electron microscopy (FE-SEM) observation was carried out on a JSM-6700F instrument (JEOL Ltd., Japan). In order to observe the cross-sectional surface, the freeze-fractured sample was mounted on a brass stub and sputter-coated with gold/palladium to minimize sample charging using a Hitachi ion sputter E-1010.

6-3. Results and Discussion

6-3-1. Structural analysis of dip-coated PSiP/IL composite membrane

The surface FE-SEM image of dip-coated PSIP/IL composite membrane is shown in Figure 6-1. The two-dimensional close-packed (cp) planes of PSiP were clearly observed in this FE-SEM image, corresponding to the (001) plane in the description of Miller index for the *hexagonal system*, in which

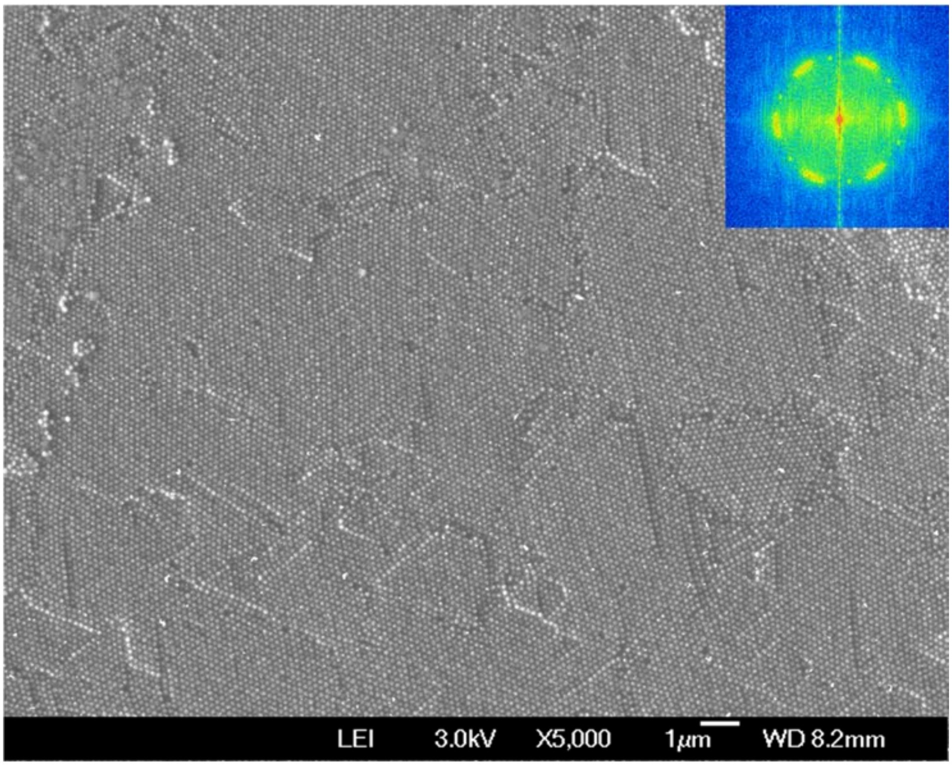

Figure 6-1. The field emission scanning electron microscopy (FE-SEM) image of the dip-coated membrane of PSiP/IL composites. The upper right inset show fast Fourier transform images from the FE-SEM images.

the cp plane is defined as an *x*-*y* plane of a unit lattice. This result indicates that this PSiP/IL composite membranes was deemed to form close packing structure as fcc, hcp, and rhcp.

GISAXS images with incident angle α_i = 0.07, 0.10, and 0.20° for dip-coated PSiP/IL composite membrane are shown in Figure 6-2(a). The vertical and horizontal directions in the images are defined as the *z*- and *x*-axis, respectively. As incident angle increased, the diffraction pattern due to the reflected incident beam shifted toward the *z*-axis direction. For the peak analysis to determine the crystal structure, it is considered to be suitable to use a GISAXS image in which the diffraction peaks due to the transmitted X-ray beams are separated from those of reflected X-ray beams. Figure 6-3(a) indicates the GISAXS image with incident angle α_i = 0.20° with possible diffraction peaks of fcc indicated by red circles (transmitted) and blue squares (reflected) in the figure assuming the fcc with the (111) lattice plane in the description of Miller index for fcc parallel to the dip-coat substrate. The nearest particle distance was calculated as 168 nm. The angles α and $2\theta_{xy}$ in the GISAXS 2D profiles are the vertical and horizontal components of the output angle, respectively. However, these prediction circles were not fitted to the GISAXS image, which means the crystal structure of PSiP/IL membrane is not fcc. Here, the diffraction patterns derived from the transmitted X-ray and the reflected X-ray appeared symmetrically at α = 0°. If the ideal measurement were carried out, the center line of transmitted-

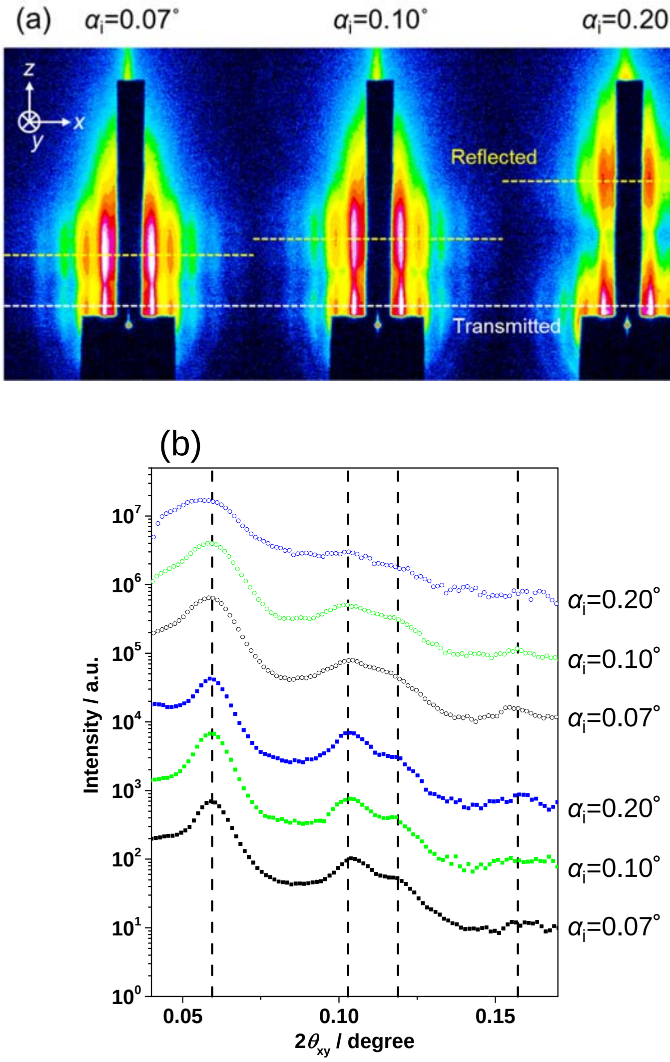

Figure 6-2. (a) Measured GISAXS patterns of dip-coated PSiP/IL composite membrane. The incident angle α_i for each image is inset in each image. Insert dash lines represent the 0th layer line for the reflected beam (yellow), and the 0th layer line for transmitted beam which was incident from the edge of the membrane and refracted inside the membrane (white). (b) GISAXS intensity profiles of dip-coated membrane. Inset dashed lines mean the predicted diffraction peaks of (*hk*0) plane of the hcp lattice.

scattered patterns appeared at the direct beam position, α = -0.20°. However, the direct beam position was α = -0.20°, the center line of transmitted-scattered patterns appeared at α = -0.16°. This strange results may be caused by the transmitted X-ray which may go toward the edge of the sample, described as Figure 6-4. Figure 6-3(b) indicates GISAXS images with incident angle α_i = 0.20° with possible diffraction peaks of hcp indicated by red circles (transmitted) and blue squares (reflected) in the figure assuming the hcp with the (001) lattice plane in the description of Miller index for hcp parallel to the

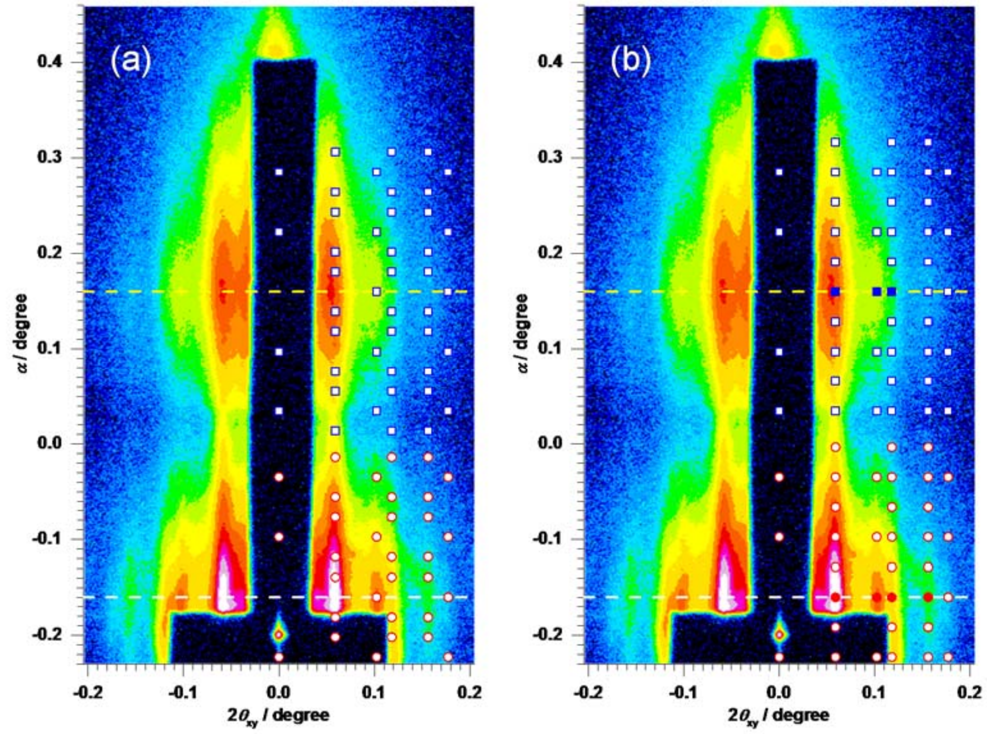

Figure 6-3. Comparison between a measured GISAXS pattern with α_i=0.20° and simulated scattering spots which is estimated from (a) the fcc-type lattice and (b) the hcp-type lattice. Inset blue squares and red circles denote simulated scattering spots by the reflected and transmitted X-ray beams, respectively. Filled marks are considered as the scattering spots.

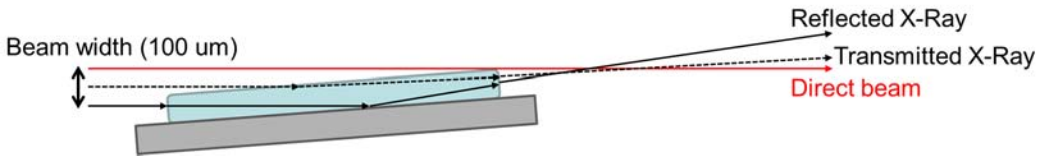

Figure 6-4. The schematic image of GISAXS measurement for the dip-coated membrane of PSiP/IL composites.

dip-coat substrate. The nearest particle distance was also calculated as 168 nm. The filled marks, which means the measured diffraction peak positions, were well fitted as those of *hk*0 in the description of the Miller index for the *hexagonal system* (hcp-type lattice). Figure 6-2(b) shows line SAXS intensity profiles on $2\theta_{xy}$-axis line for transmitted and reflected scattering image (white and yellow line). These intensity profile were consistent with (*hk*0) plane diffraction patterns of (*hk*0) plane in the description of Miller index for the *hexagonal system*, which measn the structure of the PSiP dip-coated membrane was assigned to be rhcp. The SAXS image of PSiP/IL composite membrane from the through view is shown in Figure 6-5. The diffraction patterns of (*hk*0) plane in the description of Miller index for the *hexagonal system* were clearly observed. The top-right inset in Figure 6-1 was the the fast Fourier transforms (FFT) of FE-SEM image of PSiP/IL composite membrane. The FFT image show similar geometry to the scattering patterns of Figure 6-5, which indicated that cp plane of PSiP were three-dimensionally ordered and parallel to the substrate. In addition, time-resolved scattered images from the through view were

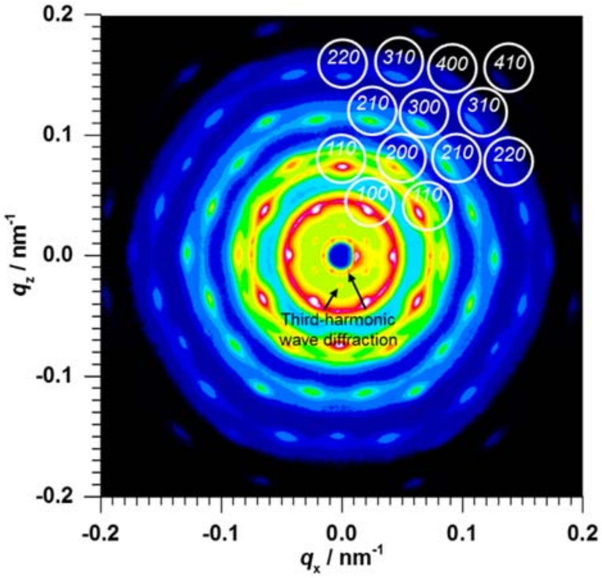

Figure 6-5. Measured SAXS patterns of dip-coated PSiP/IL composite membrane from the through view, which was obtained in BL40B2. Diffraction spots derived from (*hk*0) planes of the hcp-type lattice as well as third-harmonics wave diffraction were observed, which is consistent with the results of GISAXS measurements.

shown in Figure 6-6, assigned to be rhcp as well. Figure 6-7 shows a cross-sectional FE-SEM image of a dip-coated membrane, indicating that the thickness of the dip-coated membrane was 70 μm.

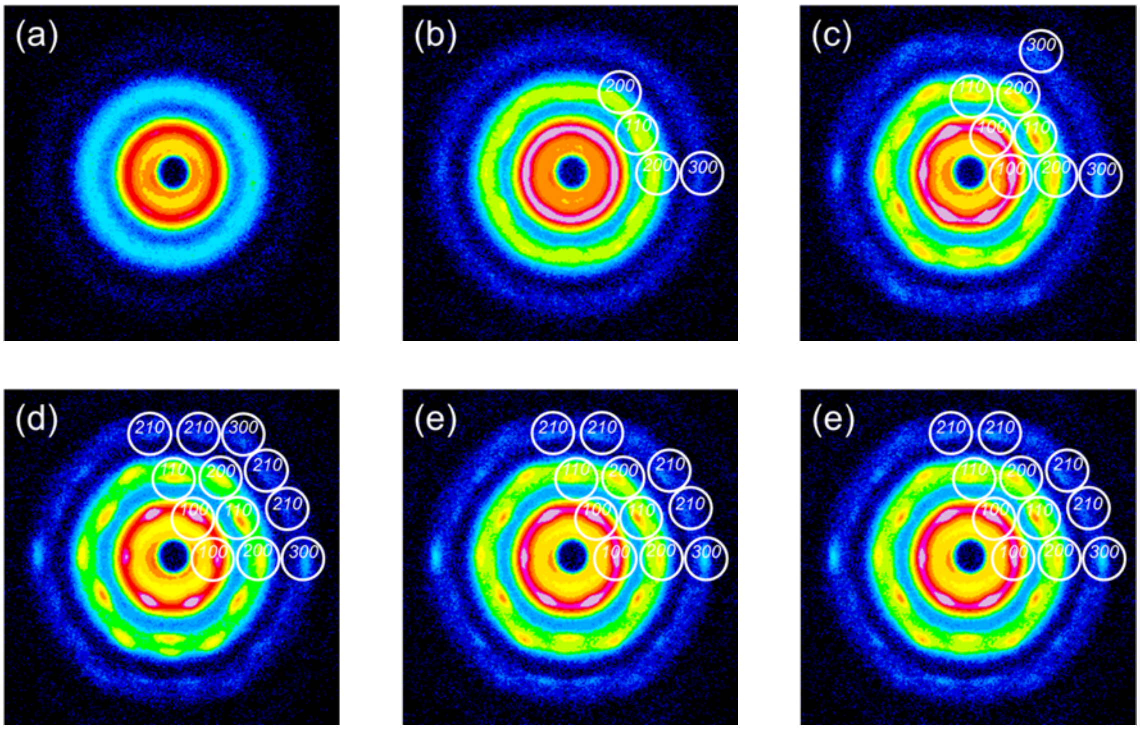

Figure 6-6. Time-resolved SAXS patterns of dip-coated PSiP/IL composite membrane from the through view at (a) 23, (b) 24, (c) 25, (d) 30, (e) 35, and (f) 43 min, which was started at z = -3.6 mm. Diffraction spots derived from (*hk*0) planes of the hcp-type lattice were observed in some images, which are consistent with the results of GISAXS measurements in BL03XU and USAXS measurement from the through view in BL40B2.

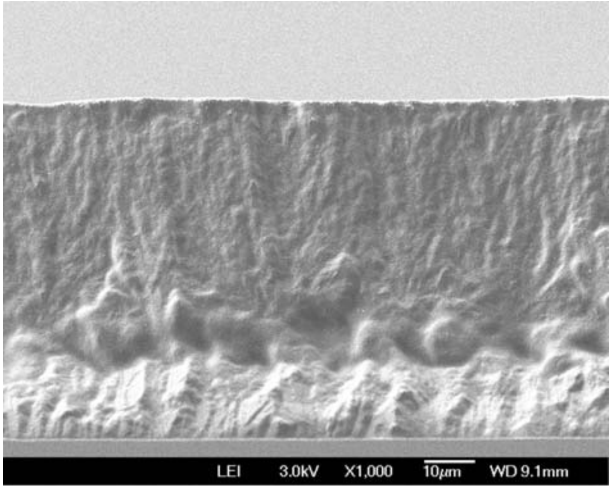

Figure 6-7. The cross-sectional FE-SEM image of dip-coated membrane, whose thickness is 70 um.

6-3-2. Structural dynamics of dip-coated PSiP/IL composite membrane

The particle number density N_d was estimated by the diffraction patterns using following equation:

$$N_\mathrm{d} = \frac{3\sqrt{6}{q_{100}}^3}{64\pi^3} = \frac{\sqrt{2}{q_{110}}^3}{64\pi^3} = \frac{3\sqrt{6}{q_{200}}^3}{512\pi^3} \tag{6-1}$$

The particle number density n was estimated by as well:

$$N_\mathrm{d} = \frac{f_0\phi_\mathrm{m}/w_0}{f_0/\rho_0 + (1-f_0)/\rho_\mathrm{IL}} \tag{6-2}$$

$$f_0 = \frac{f_\mathrm{PSiP}}{1+A_\mathrm{g}} \tag{6-3}$$

$$w_0 = \frac{4\pi\rho_0{r_0}^3}{3} \tag{6-4}$$

where ϕ_m is the volume fraction of the mixture of PSiP and IL, f_0 and w_0 are the weight fraction of the silica-core part and the weight of one core particle, respectively; ρ_0 and ρ_IL are the bulk densities of silica core (2.0) and IL (1.42), respectively. To estimate ϕ_m in the meniscus, using X-ray absorbance (μR), described as follows, is efficient:

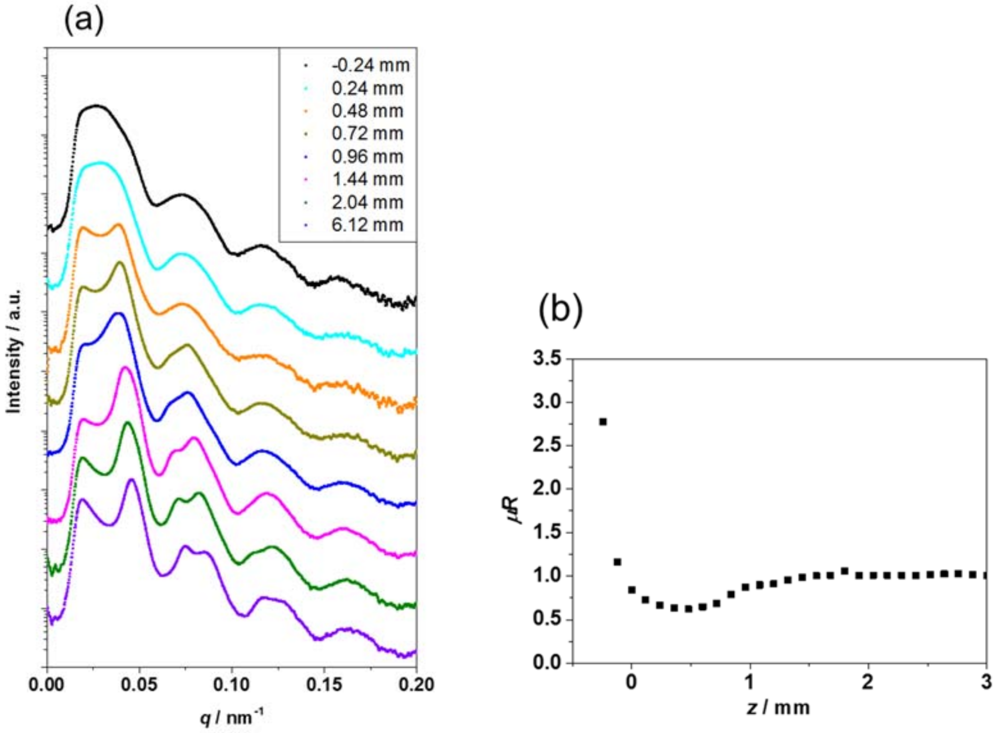

Figure 6-8. (a) Measured USAXS intensity profiles and (b) the X-ray absorbance during the dip-coating experiment for PSiP/IL composite membrane, whose the first position was z = -2.6 mm.

$$\mu R = [\mu_\mathrm{m}\phi_\mathrm{m} + \mu_\mathrm{s}(1-\phi_\mathrm{m})]y_\mathrm{d} \tag{6-5}$$

where y_d is the distance of meniscus in the X-ray incidence direction, μ_s is the X-ray absorption coefficient of the solvent (acetonitrile), and μ_m and ϕ_m are the X-ray absorption coefficient and the volume fraction of the mixture of PSiP and IL, respectively. μ_m is given as follows because there is considered to be few difference between CPB and IL in terms of the scattering length density:

$$\mu_\mathrm{m} = \frac{\mu_0 f_0/\rho_0 + \mu_\mathrm{IL}(1-f_0)/\rho_\mathrm{IL}}{f_0/\rho_0 + (1-f_0)/\rho_\mathrm{IL}} \tag{6-6}$$

Here, ϕ_m is expressed as follows:

$$\phi_\mathrm{m} = \frac{\mu R - \mu_\mathrm{s} y_\mathrm{d}}{(\mu_\mathrm{m}-\mu_\mathrm{s})y_\mathrm{d}} \tag{6-7}$$

Figure 6-8 and 6-9 show the USAXS intensity profiles and X-ray absorbance at different positions. According to these results, the number density of PSiP can be determined by eq (6-1) in the case of having diffraction patterns and eq (6-2) for not having diffraction patterns in the range described in Figure 6-10. Considering the solvent evaporation at the different position, normalization of the starting

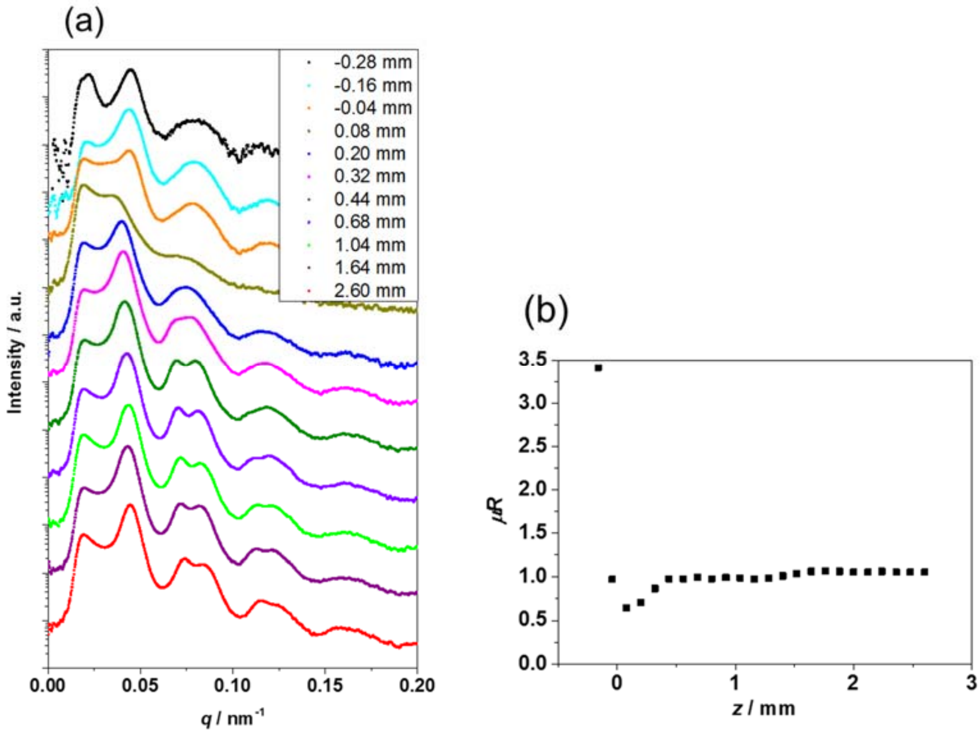

Figure 6-9. (a) Measured USAXS intensity profiles and (b) the X-ray absorbance during the dip-coating experiment for PSiP/IL composite membrane, whose the first position was z = -3.6 mm.

position using μR described as Figure 6-11. Figure 6-12 shows the plot of the number density of PSiP and full width at half maximum (FWHM) of (110) plane of the hcp-type lattice during dip-coating v.s. the meniscus distance z. This plot means the particle concentration and the orientation of PSiP in and around meniscus of the dip-coating. Figure 6-13 shows the schematic illustration of the dynamics of the dip-coating process. The diffraction patterns appeared about at near z = 1 mm, which suggested the crystallization started around the meniscus. The particle concentration was rapidly increased in the meniscus, which is considered to induce the crystallization. Above the meniscus (z > 1 mm), the value of FWHM was gradually decreased, which means that the orientation of PSiPs were progressing as

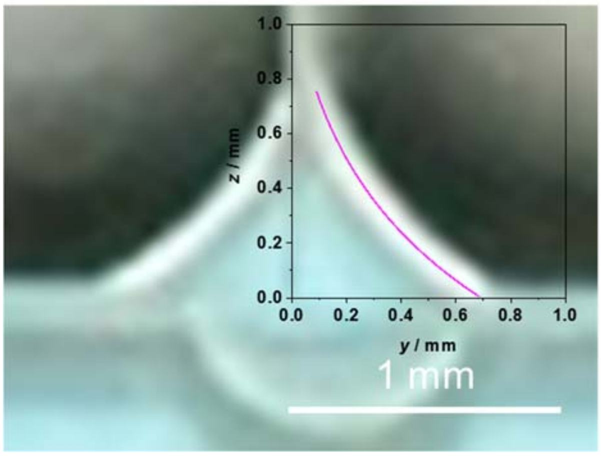

Figure 6-10. The meniscus profile for the simulation of the number density of PSiP by X-ray absorption.

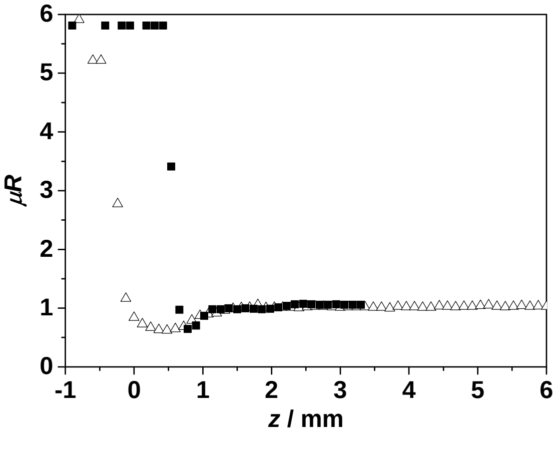

Figure 6-11. The X-ray absorbance during the dip-coating measurement. Filled black square plots are moved -0.5 mm for the alignment of the z-axes.

solvent was being vapored despite high particle concentration. One of the property of CPB in good solvent is high elasticity, which is considered to result in forming well-ordered and oriented structure of PSiPs in dip-coated membrane. In addition, this crystallization from liquid to rhcp during dip-coating is consistent with the results in Chapter 2.

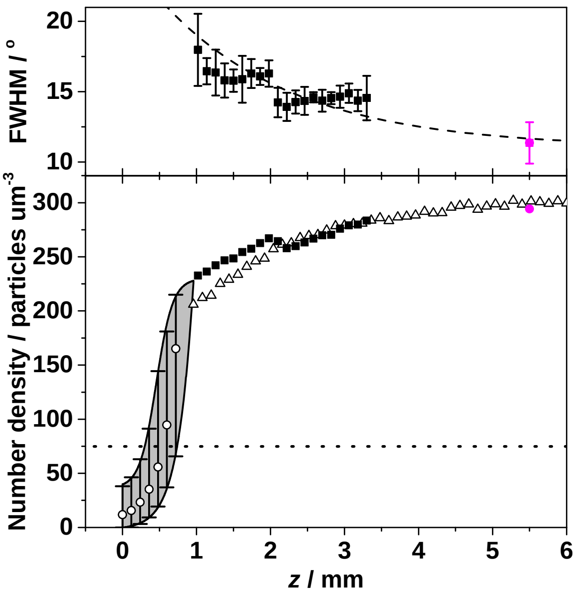

Figure 6-12. Plot of the number density of PSiP and FWHM of (110) plane of the hcp-type lattice during and after dip-coating: (open circle) obtained by X-ray absorption; (others) estimated from diffraction patterns of which the first position of dip-coating was (open triangle) z = -2.6 mm and (filled black square) z = -3.6 mm, and (pink square) after dip-coating.

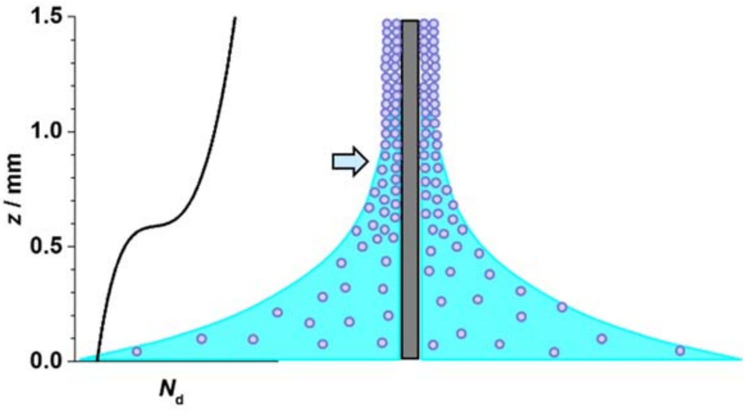

Figure 6-13. The schematic illustration of the meniscus of dip-coating. The arrow indicates the crystallization point. N_d indicates the number density of PSiP.

6-4. Conclusion

I fabricated and analyzed higher-order structures of the composites of CPB-modified nanoparticles and ionic liquid and revealed the concentration-dependent crystallization of PSiP. The higher-order (crystal) structures of PSiP/IL composites are rhcp and fcc, although the structure depends on the concentration of PSiP. While the swollen CPBs in good solvents indicate high elasticity, this work reveals the relationship between the concentration and the higher-order structure of colloidal particles with high elasticity. In future, the relationship between the concentration and the interparticle potential of colloidal particles will be investigated to understand the formation of higher-order structure of colloidal particles with polymer brushes.

References

1. E. Yablonovitch. *Phys. Rev. Lett.* **1987**, *58*, 2059–2062.

2. S. John. *Phys. Rev. Lett.* **1987**, *58*, 2486–2489.

3. J. M. Weissman, H. B. Sunkara, A. S. Tse, S. A. Asher. *Science* **1996**, *274*, 959–960.

4. H. S. Yang, J. Jang, B. S. Lee, T. H. Kang, J. J. Park, W. R. Yu. *Langmuir* **2017**, *33*, 9057–9065.

5. J. H. Holtz, S. A. Asher. *Nature* **1997**, *389*, 829–832.

6. A. Boden, M. Bhave, P. Y. Wang, S. Jadhav, P. Kingshott. *ACS Appl. Mater. Interfaces* **2018**, *10*, 2264−2274.

7. J. R. Lawrence, Y. R. Ying, P. Jiang, S. H. Foulger. *Adv. Mater.* **2006**, *18*, 300–303.

8. H. Ogawa, M. Takenaka, T. Miyazaki, A. Fujiwara, B. Lee, K. Shimokita, E. Nishibori, M. Takata. *Macromolecules* **2016**, *49*, 3471–3477.

9. S. Watanabe, K. Inukai, S. Mizuta, M. T. Miyahara. *Langmuir* **2009**, *25*, 7287–7295.

10. N. Vogel, M. Retsch, C. A. Fustin, A. del Campo, U. Jonas. *Chem. Rev.* **2015**, *115*, 6265–6311.

11. P. A. Kralchevsky, K. Nagayama. *Langmuir* **1994**, *10*, 23−36.

12. A. S. Dimitrov, K. Nagayama. *Langmuir* **1996**, *12*, 1303–1311.

13. E. Metwalli, V. Körstgen, K. Schlage, R. Meier, G. Kaune, A. Buffet, S. Couet, S. V. Roth, R. Röhlsberger, P. Müller-Buschbaum. *Langmuir* **2013**, *29*, 6331–6340.

14. N. Paul, E. Metwalli, Y. Yao, M. Schwartzkopf, S. Yu, S. V. Roth, P. Muller-Buschbaum, A. Paul. *Nanoscale* **2015**, *7*, 9703–9714.

15. T. P. Lodge, B. Pudil, K. J. Hanley. *Macromolecules* **2002**, *35*, 4707–4717.

16. M. Shibayama, T. Hashimoto, H. Kawai. *Macromolecules* **1983**, *16*, 1434–1443.

17. F. M. Abuzaina, A. J. Patel, S. Mochrie, S. Narayanan, A. Sandy, B. A. Garetz, N. P. Balsara. *Macromolecules* **2005**, *38*, 7090–7097.

18. V. Mishra, S. M. Hur, E. W. Cochran, G. E. Stein, G. H. Fredrickson, E. J. Kramer. *Macromolecules* **2010**, *43*, 1942–1949.

19. S. H. Kim, M. J. Misner, T. P. Russell. *Adv. Mater.* **2004**, *16*, 2119–2123.

20. A. Hexemer, P. Muller-Buschbaum. *Iucrj* **2015**, *2*, 106–125.

Chapter 7

Fabrication of quasi-solid electrolyte of concentrated-polymer-brush-modified nanoparticles self-assembled in iodide-containing ionic liquid toward dye-sensitized solar cell

7-1. Introduction

Dye-sensitized solar cells (DSSCs), which was first reported by Grätzel et al,[1] have attracted much attention as alternatives which are replaced from conventional inorganic photovoltaic devices. The energy conversion efficiency of DSSCs reach more than 10% when using iodide/iodine liquid electrolytes as the conducting element.[2-10] Despite offering relatively high conversion efficiencies for solar energy, typical DSSCs suffer from durability problems that result from their use of organic liquid electrolytes, which causes serious problems such as electrolyte leakage, volatilization, and so on.[11-15] To overcome these problems, many research groups have been searching for alternatives to replace the liquid electrolytes, such as solid-state or quasi-solid-state electrolytes.[16-19]

Herein, our group suggests using the technique of concentrated polymer brushes, which have many interesting properties such as high stretching, high orientation, high elasticity, low friction, and so on.[20] Concentrated polymer brushes can be synthesized by surface-initiated living radical polymerization, and this surface-modification technique has been applied to many types of substrates.[21] Particularly, brush-modified silica nanoparticles (PSiPs) can form semi-colloidal crystals because of high elasticity between polymer brushes on silica nanoparticles.[22-25]

One of the application of semi-soft colloidal crystals to the electrolyte for lithium ion batteries was previously reported.[26,27] In addition, our recent work also revealed that using dip-coating method enables the production of quasi-solid membrane with regularly-arrayed PSiP in ionic liquid.[28] In this paper, I aimed to apply a PSiP membrane to electrolyte for DSSCs. The strategy is the following points: First of all, we focused on fabricating PSiP membrane with regularly-arrayed structures in the presence of iodine/iodide redox components (I^-/I_3^-). Next, we demonstrated the photovoltaic characteristics of DSSC using PSiP membranes.

7-2. Experimental section

7-2-1. Chemicals

An atom transfer radical polymerization (ATRP)-initiator-holding silane coupling agent ((2-bromo-2-methyl)propionyloxypropyltriethoxysilane, BPE) was synthesized as reported previously.[29] Copper(I) chloride (Cu(I)Cl; Wako Pure Chemical Industries, Ltd., Japan, 99.9%) was washed with glacial acetic acid (Wako, 99.7%) to remove any soluble oxidized impurities, filtered, washed with ethanol (Wako) and diethyl ether (Wako), and finally dried. *N*,*N*-Diethyl-*N*-(2-methacryloylethyl)-*N*-methylammonium bis(trifluoromethylsulfonyl) imide (DEMM-TFSI) was obtained from Toyo Gosei

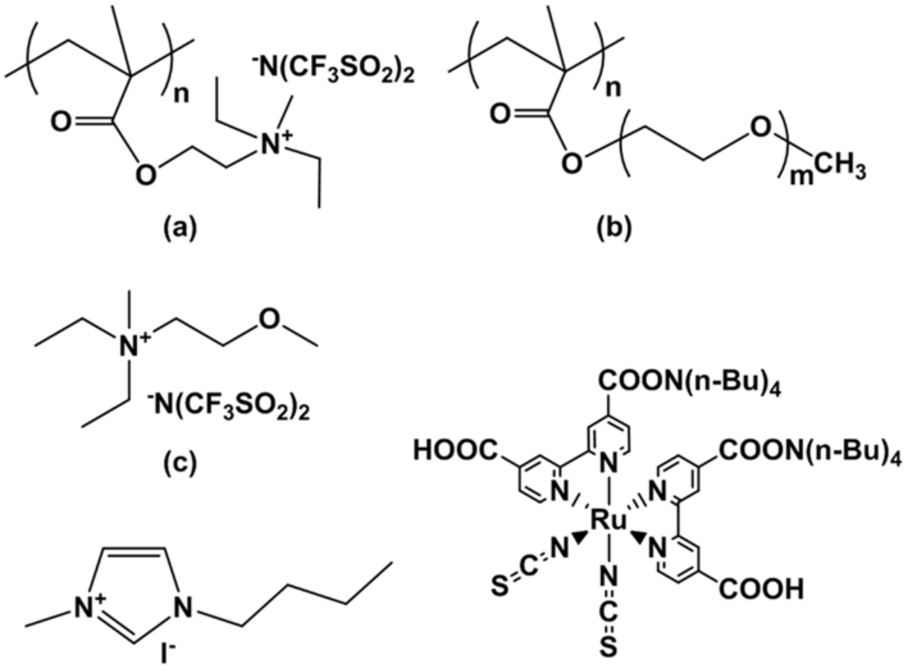

Figure 7-1. Molecular structures of (a) P(DEMM-TFSI), (b) P(PEGMA), (c) DEME-TFSI, (d) BMII, and (e) N719.

Co., Ltd., Japan. Poly((ethylene glycol) methyl ether methacrylate) (PEGMA; the number average molecular weight M_n = 500) was purchased from Sigma-Aldrich Co. LLC, Japan. *N*,*N*-diethyl-*N*-(2-methoxyethyl) ammonium bis(trifluoromethane sulfonyl) imide (DEME-TFSI; Kanto Chemical Co., Inc., Japan), 1-butyl-3-methylimidazolium iodide (BMII; Kanto Chemical), iodine (I_2; Wako, 99.8%), and titanium(IV) chloride ($TiCl_4$; Wako, 99.0%) were used as received. Nanocrystalline TiO_2 (Ti-nanoxide T/SP), scattering TiO_2 (Ti-nanoxide R/SP), and cis-dithiocyanate-*N*,*N*'-bis (4-carboxylate-4-tetrabutylammoniumcarboxylate-2,2'-bipyridine) ruthenium(II) (N719 dye, Ruthenizer 535-bisTBA) were purchased from Solaronix SA, Switzerland. All other reagents were commercially available and used as received. Standard samples of poly(ethylene glycol) (PEG) and poly(methyl methacrylate) (PMMA) were obtained from Polyplastics Co., Ltd., Japan.

7-2-2. Synthesis and characterization of polymer-brush-modified hybrid particles

Silica particle (SiP) (SEAHOSTER KE-E10, 20 wt % suspension of SiP in ethylene glycol) was kindly donated by Nippon Shokubai Co., Ltd., Osaka, Japan and surface-modified by BPE as reported previously.[29] According to Chapter 2, the average core diameter and the standard deviation of thus obtained SiPs (BPE–SiPs) were determined to be 148 nm and 8 nm, respectively, by the ultrasmall angle X-ray scattering (USAXS) method. Polymer-brush-modified hybrid particles (PSiP) were synthesized by the surface-initiated ATRP. In brief, BPE–SiP was dispersed in a degassed polymerization solution containing monomer (DEMM-TFSI or PEGMA), catalytic complexes (Cu(I)Cl and Cu(II)Cl_2 with Ligand), 2-(EiB)Br and solvent (anisole or DNF), and heated at 60 °C for the prescribed time. Three samples P1, P2 and P3 were obtained under the polymerization conditions listed in Table 7-1. P1 is P(DEMM-TFSI)-brush-modified SiP, the same as reported in Chapter 2, and P2 and P3 are P(PEGMA)-brush-modified SiPs. At polymerization, 2-(EiB)Br was added as a nonfixed (free) initiator not only to control the polymerization but also to produce a free (unbound) polymer, which was reasonably assumed to have the same molecular weight and distribution as a graft polymer. After the polymerization, an aliquot of the polymerization solution was subjected to the proton nuclear magnetic resonance (^{1}H NMR) measurement (AL300 spectrometer, 300 MHz, JEOL, Japan) to estimate the monomer conversion and the gel permeation chromatographic (GPC) measurement (GPC-101 high-speed liquid chromatography system, Shoko Science Co, Ltd., Japan) to determine the molecular weight and its distribution. The obtained PSiPs were purified by repeated cycles of redispersion/centrifugation in acetonitrile. The weight of the grafted polymer relative to the SiP-core weight (A_g) was estimated by thermogravimetry (TGA-50 instrument, Shimadzu, Kyoto, Japan) under an argon atmosphere. Table 7-2 summarizes the polymerization results and the characteristics of the obtained PSiPs. Here, the graft density (σ) and the surface occupancy (σ^*) were calculated from the estimated values of $M_{n,exp}$, A_g, and SiP-core diameter assuming that the density of P(DEMM-TFSI), P(PEGMA) and SiP-core are 1.42, 1.15, and 2.0, respectively. Note that the $M_{n,exp}$ value of each particle was very close to the theoretical one estimated from the conversion assuming complete initiation, and that the M_w/M_n ratio was nearly equal to that estimated using PEG or PMMA calibration, suggesting successful evaluation as the absolute value of the molecular weight and its distribution.

7-2-3. Preparation of PSiP composite membraness

Mixed ionic liquid (mIL; DEME-TFSI/BMII = 63/37 by wt%) and electrolyte solution (ES; 0.15 M of I_2 in mIL) were prepared. The PSiP/IL- or PSiP/ES-composite membranes were fabricated on various substrates by the dip-coating method. The dip-coating solution contains PSiP (22.2 wt%), IL or ES (7.8 wt %), and volatile solvent (70 wt%, acetonitrile unless otherwise specified). The speed of dip-coating was 5 μm/sec in the initial 2 mm in height followed by 2 μm/sec. The obtained membranes were dried in vacuum oven at 60 °C for 12h.

Table 7-1. Polymerization Conditions of Surface-initiated ATRP.

	Temp.	Time	Monomer	Solvent	BPE–SiP	2-(EiB)Br	$CuCl_1$	$CuCl_2$	Ligand
P1	70 °C	18.5 h	DEMM-TFSI	Acetonitrile 150 g	10 g	1.1 g (5.7 mmol)	0.45 g (4.5 mmol)	0.15 g (1.1 mmol)	2,2’-bipyridine 1.9 g (12 mmol)
P2	60 °C	2 h	PEGMA 25 g (50 mmol)	anisole 100 g	5 g	0.23 g (1.2 mmol)	49 mg (0.49 mmol)	3.5 mg (0.026 mmol)	dN-bipy 0.10 g (0.25 mmol)
P3	60 °C	23 h	PEGMA 60 g (120 mmol)	DMF 120 g	4 g	0.42 g (2.2 mmol)	0.21 g (2.1 mmol)	15 mg (0.11 mmol)	2,2’-bipyridine 0.77 g (4.9 mmol)

Table 7-2. Characteristics of Silica Particle Grafted with Concentrated Polymer Brush.

Particle	Brush component	$M_{\mathrm{n,\ theo}}{}^{a}$	$M_{\mathrm{n,\ exp}}{}^{b}$	$M_{\mathrm{w,\ exp}}{}^{b}$	$M_{\mathrm{w}}/M_{\mathrm{n}}{}^{b}$	σ [chains/nm^2] ^{c}	σ*
P1	P(DEMM-TFSI)	24 300	27 800	29 900	1.08	0.19	42%
P2	P(PEGMA)	10 300	9 900	11 800	1.19	0.11	33%
P3	P(PEGMA)	27 500	34 600	42 600	1.23	0.11	33%

[a] Determined by NMR conversion. [b] Measured by GPC-MALLS. [c] Determined by TGA results.

7-2-4. Measurements

For the GPC measurement, a Shodex GPC-101 high-speed liquid chromatography system was equipped with a multi-angle laser light-scattering (MALLS) detector (DAWN HELEOS, Wyatt Technology Co., USA). The eluent and column system was a solution of acetonitrile/water (50/50 by vol/vol) containing 0.1 M $NaNO_3$ and 0.25 M CH_3CO_2H and two SB-806M HQ (Shodex) columns (calibrated by PEO standards) for P(DEMM-TFSI), and DMF containing 10 mM LiBr and two LF-804 (Shodex) columns (calibrated by PMMA standards) for P(PEGMA). Field-emission scanning electron microscopy (FE-SEM) observation was carried out on a JSM-6700F instrument (JEOL Ltd., Japan). In order to observe the cross-sectional surface, the sample was freeze-fractured, mounted on a brass stub and sputter-coated with gold/palladium using a Hitachi ion sputter E-1010. Grazing-angle reflection–absorption infrared (GIR) measurements were carried out on a Bio-Rad FTS-6000 Fourier transform spectrometer equipped with a reflection accessory and a liquid-nitrogen-cooled mercury-cadmium-teluride detector, and ultraviolet–visible (UV-Vis) measurements were performed by a UV-3600 spectrometer (Shimadzu, Japan). The ionic conductivity measurement was carried out using an E4980A Precision LCR Meter (Agilent Technologies, Inc., USA) with the frequency from 20 Hz to 2 MHz at 30 °C using the line-patterned conductivity electrode (BAS Inc., Japan). Optical microscopic observations were carried out on a digital microscope Keyence VHX-2000 with the lens VH-Z20R (Keyence, Japan). Ultra-small angle X-ray scattering (USAXS) measurement was performed for a sample prepared on an silicon wafer at the beamline BL19B2 in SPring-8 (Harima, Hyogo, Japan). The USAXS profiles were obtained on a two-dimensional hybrid pixel array detector, PILATUS 2M with 3 × 6 modules (DECTRIS Ltd.) and 1475 × 1679 pixels of 172 μm pixel size. The X-ray wavelength (λ), the sample-to-detector distance, and the X-ray beam size at the sample position (horizontal × vertical) were 0.0689 nm, 41523 mm, and 300 μm × 100 μm, respectively. The scattered intensities are expressed as a function of the scattering vector, $q = (4\pi \sin\theta)/\lambda$, where 2θ is the scattering angle relative to the incident beam. The q value was calibrated using a collagen fiber extracted from a chicken leg. The thickness of PSiP membranes, of which the edge was scratched to identify the surface of substrates, was measured by a Wyko NT9100 surface profiler (Veeco Instruments, Inc., USA).

7-2-5. DSSC preparation and characterization

A dye-adsorbing porous TiO_2 anode was prepared as follows. On the fluorine-doped tin oxide (FTO; sheet resistance of 10 Ω cm^{-2}, Asahi glass Co. Ltd., Japan), the TiO_2 anatase colloidal paste (Solaronix Ti-nanoxide T/SP) was coated and sintered at 140 °C for 15 min and at 475 °C for 30 min. This cycle was repeated with the same paste and then another TiO_2 anatase colloidal paste (Solaronix Ti-nanoxide R/SP). The resulting TiO_2 electrode with a thickness of 12 μm was treated with 40 mM $TiCl_4$ aqueous solution at 70 °C for 30 min followed by annealing at 140 °C for 15 min and 475 °C for 30 min and finally immersed in a mixture of acetonitrile and 2-methyl-2-propanol (1:1) containing a 0.5 mM N719 dye at 40 °C for 24 h to obtain the dye-TiO_2 electrode.

A cathode electrode was an indium-tin-oxide (ITO; 5 Ω cm^{-2}, Geomatec Co., Ltd., Kanagawa, Japan) substrate sputtered with Pt using a Hitachi ion sputter E-1010. A PSiP-electrolyte membrane was dip-coated on the Pt/ITO cathode electrode. A DSSC was prepared by bonding together thus obtained cathode with the dye-TiO_2 anode pre-degassed and pre-filled with ES. For a liquid electrode, the Pt/ITO cathode and dye-TiO_2 anode electrodes were stuck together with a Himilan spacer (Mitsui-Dupont Polychemicals Co., Ltd.) with a thickness of 25 and 50 μm. The DSSC devices were illuminated through a 0.0534 cm^2 mask using a MAX-301 (Asahi spectra Co., Ltd., Japan) to provide an incident irradiance of 100 mW cm^{-2} at the surface of the solar cells. The photogenerated current was measured as a function of applied voltage using a Keithley model 2400 digital source meter.

7-3. Results and Discussion

7-3-1. Preparation and characterization of quasi-solid composite electrolyte membranes

We have already reported that P1 was self-assembled in DEME-TFSI, giving a good performance as a quasi-solid electrolyte for the high-density lithium-ion battery and the high-density electric double layer capacitor. Here, mIL was used as an electrolyte solution toward DSSC application; the composition of mIL was determined referring a previous report on the similar electrolyte applied for DSSC. Figure 7-2(a) shows the cross-sectional FE-SEM image of P1/mIL membrane dip-coated using acetonitrile as a volatile solvent, indicating that the PSiP wasn't regularly stacked. We used different volatile solvents including acetonitrile, acetone, propylene carbonate, and γ-butyrolactone, but resulted in failure. This was judged to be caused presumably by poor affinity between the polymer-brush component and mIL; in fact, P(DEMM-TFSI) was hardly dissolved in mIL. We assumed that the PSiP was easily and well self-assembled in ionic liquid by the dip-coating or solvent-casting method owing to the CPB effect, especially ultra-low friction and completely high repulsiveness, which should be effective in a swollen state, in other words, under the good solvent condition. In the present case, P1 was at first homogenously dipersed with the help of volatile co-solvent but presumably aggregated during vaporization and hence increase concentration of mIL before it was self-assembled. Therefore, we changed the polymer-brush component from P(DEMM-TFSI) to P(PEGMA) which mIL can dissolve. Figures 7-2(b) and (c) show the cross-sectional and surface FE-SEM images of P2/mIL dip-coated membrane, respectively, indicating that the PSiP was regularly stacked. This result also should be worthy of special mention in the regard that the good-solvent condition until a sufficiently high concentration was demonstrated to

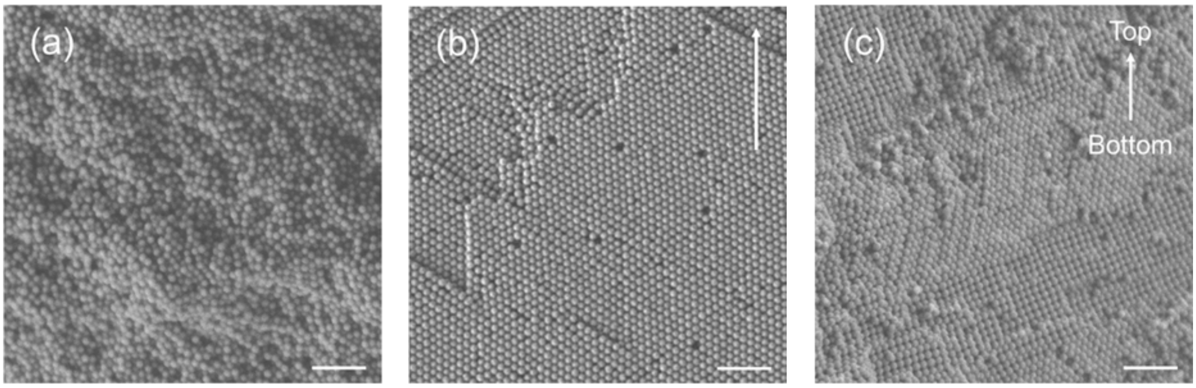

Figure 7-2. (a) A cross-sectional FE-SEM image of the P1/mIL composite membrane. (b) A surface and (c) a cross-sectional SEM images of the P2/ mIL composite membrane. The scale bar indicates 1 μm.

be essential for self-assembling of PSiP in ionic liquid (or other solvents).

Here, we consider the composition of the dip-coated membranes. Figure 7-3 shows FT-IR spectra of P2/mIL membrane by dip-coating as well as solvent-casting. In this wavelength region containing the absorption bands due to SiP core, P(PEGMA) and mIL, there is little difference in the two cases, suggesting that the dip-coated membrane had approximately the same compositions as the solvent-

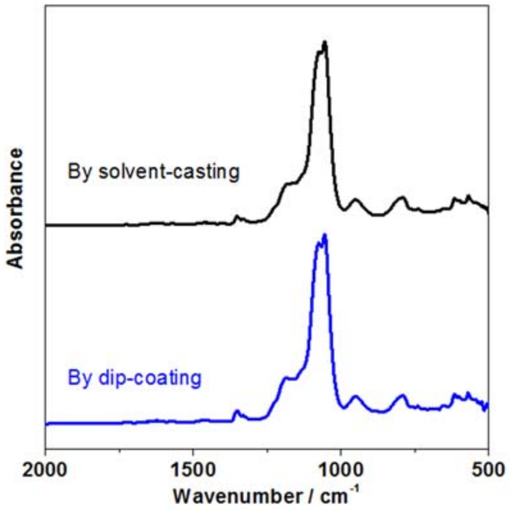

Figure 7-3. IR spectra of P2/mIL composite membrane by solvent casting and dip-coating.

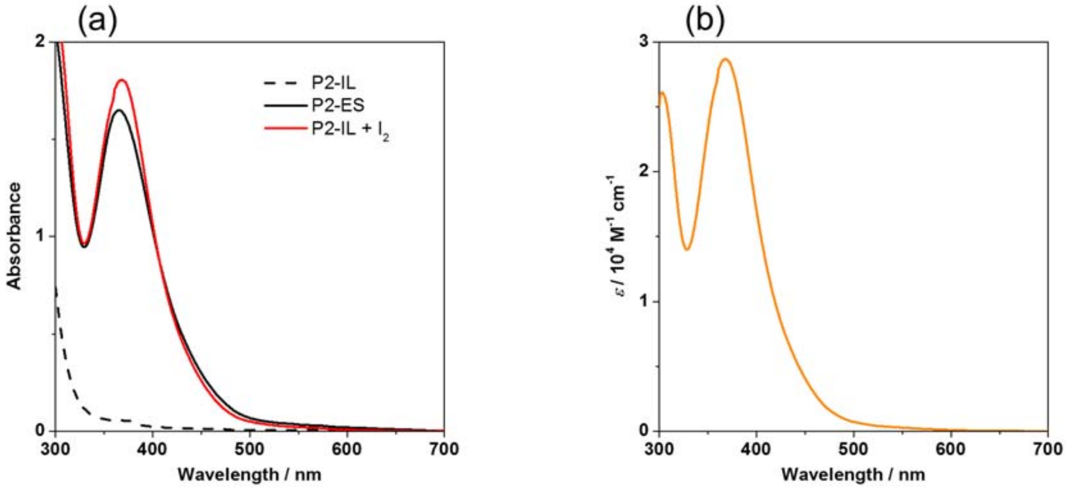

Figure 7-4. (a) UV-spectra of dip-coated membranes using P2. The red line indicates the summation of P2/mIL and 0.15 M I_2 in ES. (b) Plot of absorption coefficient of I_2 in ES.

casted one. For completing an iodide-based (I^-/I_3^-) redox system, the appropriate amount of iodine (I_2) was dissolved in the dip-coating solution, mainly forming I_3^- by the reaction of I^- in the solution. Figure 7-4(a) shows the UV-Vis spectra of the dip-coated P2/mIL- and P2/ES-membranes as well as the theoretical absorbance A_{calc} calculated by eq (7-1) for the latter. The absorption band at around 380 nm was assigned to I_3^- but not to I^- and other components (see the spectrum of the P2/mIL-membrane).

$$A_{\mathrm{calc}} = A_{\mathrm{m}} + \varepsilon_{\mathrm{I}} bc \qquad (7\text{-}1)$$

where A_{m} and b, ε_{I3}^-, c, and φ are the absorbance and thickness of the dip-coated P2/mIL-membrane, the absorption coefficient of I_3^- (estimated from the spectrum of ES, see Figure 7-4(b)), the concentration of I_2 (= 0.15 M) in ES, and the volume fraction of ES (= 0.26 assuming the density of each component to be unity), respectively. Good agreement between the observed and calculated spectra suggests that I_2 was successfully doped in proportion to the feed ratio in the dip-coated solution. Finally, we confirmed that the composition of PSiP and ES (I^-/I_3^- redox system) was approximately the same as the feed ratio in the dip-coated solution.

The ionic conductivity κ of the P2/ES membrane at 30 °C was measured by means of the impedance spectroscopy using the line-pattern electrode. Figure 7-5 shows that the plot of resistance R

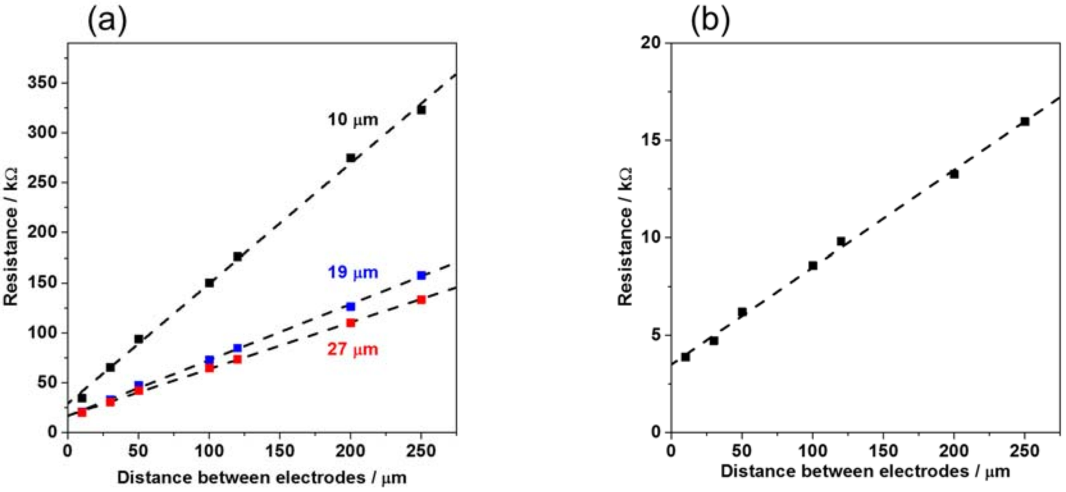

Figure 7-5. Plot of resistance vs distance between electrodes: (a) P2/mIL dip-coated membranes; the thickness of membranes shows in the graph. (b) ES; the thickness was 25 µm.

vs. electrode distance d for the P2/ES dip-coated membrane with thicknesses h of 10, 19, and 27 μm. Each pair of data formed a straight line and well analyzed by the following equation:

$$R = \frac{1}{\kappa}\frac{d}{hl_\mathrm{e}} + R_0 \qquad (7\text{-}2)$$

where R_0 is a contact resistance of the apparatus (all the pairs of data almost coincided in R_0 by extrapolation at $h = 0$). As shown in Figure 7-6, thus obtained κ value was almost constant independently of d, suggesting successful estimation. As summarized in Table 7-3, the P2/ES quasi-solid electrolyte gave a κ value as high as about 0.3 mS/cm, which was about 1/10 of that (determined by the same method) of the ES solution and about 100 times higher than the typical value of a so-called "solid" polymer electrolyte (applied for DSSC without any additives).[30] It should be noted that (i) the P2/ES membrane contains 74 wt% PSiP hardly contributing to the ionic conductivity, (ii) the ion-conducting

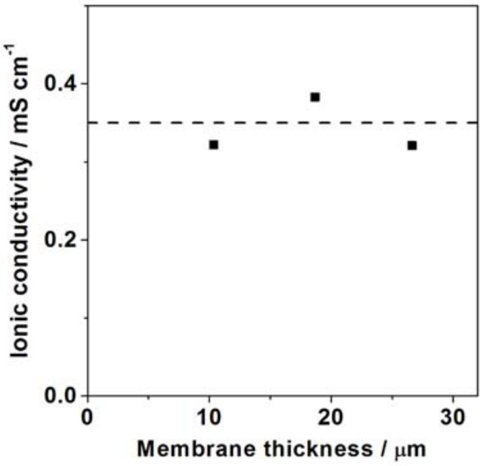

Figure 7-6. Plot of ionic conductivity vs membrane thickness for P2/mIL dip-coated membranes; the conductivity was estimated from the slope in Figure 7-5(a) using eq (7-2).

Table 7-3. Ionic conductivity of electrolytes at 30 °C.

Sample	Ionic conductivity / mS cm^{-1}
ES	3
P2/ES dip-coated membrane	0.3
Polymer solid electrolytes (no additive reagent)[30]	4.7×10^{-3}

channel formed between PSiPs contains polymer-brush component swollen by the ES, and (iii) in spite of these drawbacks, a high ionic conductivity was obtained. Such an enhanced ionic conductivity was previously demonstrated also for the P1/DEME-TFSI composite membrane for the lithium-ion battery.[26,27]

3-2. Preparation and characterization of DSSC

Figure 7-7(a) shows the surface image of P2/mIL membrane observed by the optical microscope, suggesting submillimeter-scale domains divided by some cracks. Such cracks did not cause significant trouble for the above-mentioned conductivity measurement, however, they might result in decreasing the performance of the DSSC prepared with this electrolyte membrane. In order to remove any cracks

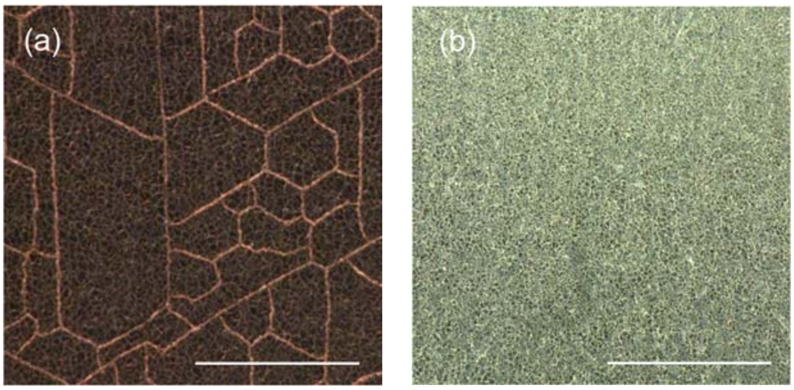

Figure 7-7. The surface OM images of the P(PEGMA)-grafted SiP/mixed IL-composite membranes; using (a) P2 and (b) P3. The scale bar indicates 1 mm.

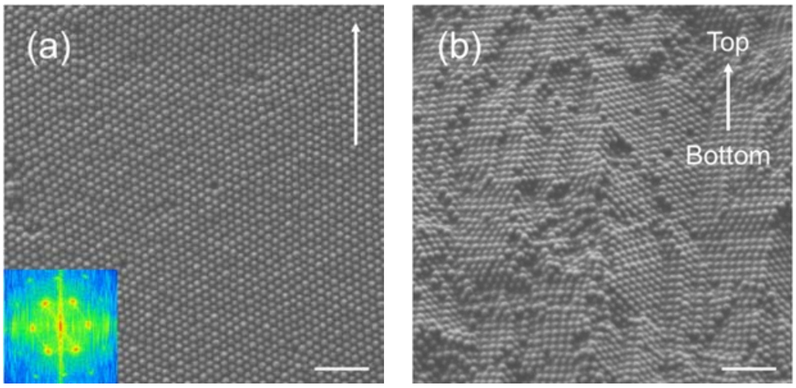

Figure 7-8. (a) Surface and (b) cross-sectional FE-SEM images of the P2/mIL-composite membranes. The scale bar indicates 1 μm.

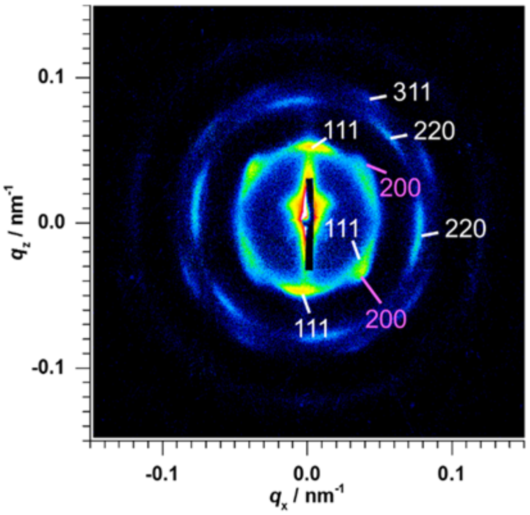

Figure 7-9. A 2D USAXS image of P3/mIL-composite membrane from the edge view. The assigned *hkl* indices of the fcc lattice are given in the image.

with regularly-arrayed structures, we decided to increase the length of graft polymers on nanoparticles and hence the flexibility of the membrane. Figure 7-7(b) shows the surface image of P3/mIL membrane, where P3 has the P(PEGMA)-brush longer but still in the CPB regime. As was expected, no crack was observed in the dip-coated membrane. Figures 7-8 and 7-9 show the FE-SEM image and the edge-view USAXS image of the P3/mIL dip-coated membrane. The bottom-left inset in Figure 4(a) was the the fast Fourier transforms (FFT) of FE-SEM image of P3/mIL membrane, which had high-symmetry hexagonal patterns. These data suggest a regularly-arrayed structure of PSiP; a close-packed plane was highly oriented parallel to the substrate surface and in the plane, one of three axes connecting the neighboring particles was almost normal to the dipping direction. The diffraction peaks of the USAXS image were assigned to the fcc, as shown along with the Miller index in the figure, with the (111) lattice plane parallel to the substrate. In addition, one of characteristic diffraction patterns for the fcc is from (200) lattice plane, which was observed clearly in the USAXS image from the edge view. The center-to-center distance D_{dis} between neighboring particles was estimated to be 162 nm from the USAXS data ($D_{\mathrm{dis,diff}}$) according to the following equation based on the fcc structure:

$$D_{\mathrm{dis,diff}} = \frac{\sqrt{6}\pi}{q_{111}} = \frac{4\pi}{q_{220}} \tag{7-3}$$

where q_{hkl} is the peak value of the diffraction from the (*hkl*) plane. This $D_{\mathrm{dis,diff}}$ value corresponds to the number density of PSiP of 330 particles μm^{-3}. According to my already reported phase diagram of PSiP self-assembled in ionic liquid as a function of polymer-brush length and particle-number density in Chapter 4, the fcc structure was expected in the present case, which was considered to be essential to meet both solidification and good ionic conductivity for a novel electrolyte.

The photovoltaic characteristics of DSSCs are shown as Figure 7-10 and Table 7-4. The device using the non-fluidic P3/ES-electrolyte membrane was demonstrated to give approximately the same performance as that using ES liquid-type electrolyte. The key to success was considered to be due to the following characteristics; (i) a good ionic conductivity as revealed above, (ii) the thinning of the electrolyte layer, and (iii) a good contact between the electrolyte and the electrodes. Concerning (ii), it should be noted that it was difficult to achieve a stable operation of the device prepared using a spacer

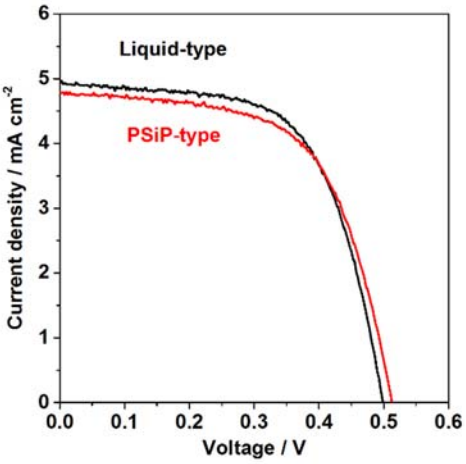

Figure 7-10. Plot of photocurrent density vs voltage for DSSCs; for the details of devices, see the text.

Table 7-4. Photovoltaic characteristics of DSSCs.

Device	*d* / μm	J_{sc} / mA cm^{-2}	V_{oc} / V	*FF*	PCE / %
Liquid-type	38	4.9	0.50	0.63	1.5
PSiP-type	13	4.8	0.51	0.62	1.5

d; thickness of the electrolyte layer, J_{sc}; short-circuit current density, V_{oc}; open-circuit voltage, *FF*; fill factor, PCE; power conversion efficiency.

of 25 μm for the liquid electrolyte layer. The characteristic (iii) is essential for a high-performance DSSC but generally difficult in a solid electrolyte. The drawback was overcome in our newly developed PSiP electrolyte, which was non-fluidic but flexible. This point was reflected especially in V_{oc} and *FF* values the same as those of the liquid device. Even though 1/10 ionic conductivity was not compensated by about 1/3 thickness of the electrolyte layer, the PSiP-device successfully gave the same J_{SC} value as the liquid device. The rate-determining step might be the electron transfer at the interface of the electrode, however, the lack of ionic conductivity of the electrolyte results in poor-functioning photovoltaic characteristics. The photovoltaic characteristics of PSiP-device means that the strategy of using PSiP for ionics devices is effective, which can improve the interfacial property for the present I^-/I_3^--mIL system.

4. Conclusion

I have succeed in fabricating PSiP membrane which formed a regularly-arrayed structure in the presence of I^-/I_3^- by designing of CPB. PSiP membrane had a high ionic conductivity in the presence of I^-/I_3^-, achieving that quasi-solid-state DSSC was fabricated by means of PSiP membranes. This work suggested that the concept of PSiP-type electrolyte with regularly-arrayed structure is universal for various ion diffusion.

References

1. B. O'Regan, M. Grätzel. *Nature* **1991**, *353*, 737–740.

2. N. J. Zhou, K. Prabakaran, B. Lee, S. H. Chang, B. Harutyunyan, P. J. Guo, M. R. Butler, A. Timalsina, M. J. Bedzyk, M. A. Ratner, S. Vegiraju, S. Yau, C. G. Wu, R. P. H. Chang, A. Facchetti, M. C. Chen, T. J. Marks. *J. Am. Chem. Soc.* **2015**, *137*, 4414–4423.

3. J. B. Yang, P. Ganesan, J. Teuscher, T. Moehl, Y. J. Kim, C. Y. Yi, P. Comte, K. Pei, T. W. Holcombe, M. K. Nazeeruddin, J. L. Hua, S. M. Zakeeruddin, H. Tian, M. Grätzel. *J. Am. Chem. Soc.* **2014**, *136*, 5722–5730.

4. Q. Yu, Y. Wang, Z. Yi, N. Zu, J. Zhang, M. Zhang, P. Wang. *ACS Nano* **2010**, *4*, 6032–6038.

5. Y. Chiba, A. Islam, Y. Watanabe, R. Komiya, N. Koide, L. Han. *Jpn. J. Appl. Phys.* **2006**, *45*, L638–L640.

6. M. K. Nazeeruddin, F. De Angelis, S. Fantacci, A. Selloni, G. Viscardi, P. Liska, S. Ito, T. Bessho, M. Grätzel. *J. Am. Chem. Soc.* **2005**, *127*, 16835–16847.

7. F. Gao, Y. Wang, D. Shi, J. Zhang, M. Wang, X. Jing, R. Humphry-Baker, P. Wang, S. M. Zakeeruddin, M. Grätzel. *J. Am. Chem. Soc.* **2008**, *130*, 10720–10728.

8. C.-Y. Chen, M. Wang, J.-Y. Li, N. Pootrakulchote, L. Alibabaei, C.-h. Ngoc-le, J.-D. Decoppet, J.-H. Tsai, C. Grätzel, C.-G. Wu, S. M. Zakeeruddin, M. Grätzel. *ACS Nano* **2009**, *3*, 3103–3109.

9. Y. Cao, Y. Bai, Q. Yu, Y. Cheng, S. Liu, D. Shi, F. Gao, P. Wang. *J. Phys. Chem. C* **2009**, *113*, 6290–6297.

10. Y. Ezhumalai, B. Lee, M. S. Fan, B. Harutyunyan, K. Prabakaran, C. P. Lee, S. H. Chang, J. S. Ni, S. Vegiraju, P. Priyanka, Y. W. Wu, C. W. Liu, S. L. Yau, J. T. Lin, C. G. Wu, M. J. Bedzyk, R. P. H. Chang, M. C. Chen, K. C. Ho, T. J. Marks. *J. Mater. Chem. A* **2017**, *5*, 12310–12321.

11. I. Chung, B. Lee, J. Q. He, R. P. H. Chang, M. G. Kanatzidis. *Nature* **2012**, *485*, 486–489.

12. J. H. Wu, S. Hao, Z. Lan, J. M. Lin, M. L. Huang, Y. F. Huang, L. Q. Fang, S. Yin, T. Sato. *Adv. Funct. Mater.* **2007**, *17*, 2645–2652.

13. J. Bisquert, D. Cahen, G. Hodes, S. Ruhle, A. Zaban. *J. Phys. Chem. B* **2004**, *108*, 8106–8118.

14. R. Komiya, L. Y. Han, R. Yamanaka, A. Islam, T. Mitate. *J. Photochem. Photobiol. A* **2004**, *164*, 123–127.

15. P. Wang, S. M. Zakeeruddin, J. E. Moser, M. K. Nazeeruddin, T. Sekiguchi, M. Grätzel. *Nat. Mater.* **2003**, *2*, 402–407.

16. C. L. Wang, L. Wang, Y. T. Shi, H. Zhang, T. L. Ma. *Electrochim. Acta* **2013**, *91*, 302–306.

17. X. Wang, S. A. Kulkarni, B. I. Ito, S. K. Batabyal, K. Nonomura, C. C. Wong, M. Gratzel, S. G. Mhaisalkar, S. Uchida. *ACS Appl. Mater. Interfaces* **2013**, *5*, 444–450.

18. F. Bella, R. Bongiovanni. *J. Photochem. Photobiol. C* **2013**, *16*, 1–21.

19. J. H. Kim, Y. S. Chi, T. J. Kang. *J. Power Sources* **2013**, *229*, 84–94.

20. Y. Tsujii, K. Ohno, S. Yamamoto, A. Goto, T. Fukuda. *Adv. Polym. Sci.* **2006**, *197*, 1–45.

21. R. Barbey, L. Lavanant, D. Paripovic, N. Schuwer, C. Sugnaux, S. Tugulu, H. A. Klok. *Chem. Rev.* **2009**, *109*, 5437–5527.

22. K. Ohno, T. Morinaga, S. Takeno, Y. Tsujii, T. Fukuda. *Macromolecules* **2006**, *39*, 1245–1249.

23. K. Ohno, T. Morinaga, S. Takeno, Y. Tsujii, T. Fukuda. *Macromolecules* **2007**, *40*, 9143–9150.

24. T. Morinaga, K. Ohno, Y. Tsujii, T. Fukuda. *Eur. Polym. J.* **2007**, *43*, 243–248.

25. T. Morinaga, K. Ohno, Y. Tsujii, T. Fukuda. *Macromolecules* **2008**, *41*, 3620–3626.

26. T. Sato, T. Morinaga, S. Marukane, T. Narutomi, T. Igarashi, Y. Kawano, K. Ohno, T. Fukuda, Y. Tsujii. *Adv. Mater.* **2011**, *23*, 4868–4872.

27. T. Morinaga, S. Honma, T. Ishizuka, T. Kamijo, T. Sato, Y. Tsujii. *Polymers* **2016**, *8*, 146.

28. Y. Nakanishi, H. Ogawa, R. Ishige, K. Ohno, T. Kabe, T. Kanaya, Y. Tsujii. to be submitted.

29. K. Ohno, T. Akashi, Y. Huang, Y. Tsujii. *Macromolecules* **2010**, *43*, 8805–8812.

30. R. A. Senthil, J. Theerthagiri, J. Madhavan. *J. Phys. Chem. Solids* **2016**, *89*, 78–83.

Summary

In **Chapter 1**, the background, purpose, and outline of this thesis were described.

In **Chapter 2**, USAXS analyses were carried out for the samples of PSiP in the CPB regime, modified ionic liquid-type polymer (P(DEMM-TFSI)) brush with 1/10 length of core-diameter, in DEME-TFSI with a wide range of concentrations. According to the analysis of the scattered intensity profiles of PSiP in lower concentration by Percus–Yevick model, the effective diameter of PSiP in good solvent was evaluated. On the other hand, the higher-order structure of PSiP in middle concentration and higher concentration was determined as rhcp and fcc, respectively. In addition, at higher concentration, the regularly-arrayed structure of PSiP was observed by USAXS and a scanning electron microscope. This change of crystal structures is considered to derive from the compression of polymer brush and the difference of osmotic repulsion force.

In **Chapter 3**, In order to reveal the structural formation of PSiP that outer-swollen properties are categorized as SDPB regime, the higher-order structure of high molecular weight of PMMA-modified PSiP, over the threshold of CPB/SDPB regime, in ionic liquid. The results of dynamic light scattering measurement indicated that PSiPs were suspended in ionic liquid as well as in an example of good solvent acetone. USAXS method enabled us to fabricate and analyze concentration-dependent self-assembling of higher molecular weight of PMMA–SiPs in IL with a wide range of concentrations. The packing fraction of PMMA–SiPs is considered to be related to change their crystal structures were determined to be fcc as well as bcc, which is the first observation in semisoft colloidal crystal system.

In **Chapter 4**, I analyzed higher-order structures of polymer-brush-modified nanoparticles in IL as a function of chain length of polymer brushes and the particle concentrations. According to the analysis, the brush component is not related to the structure formation, interparticle potential is considered to be softer as the particle concentration is higher and the chain length of polymer brushes is longer. This work is united explanation for the structure formation of colloidal crystals.

In **Chapter 5**, I analyzed the shear-induced structure formation and dynamics of CPB-modified nanoparticles with IL in various shear oscillation using time-resolved USAXS. The shear-induced crystal structure was extremely arrayed, assumed to be rhcp. The speed of shear-induced structure formation of PSiP was as fast as that of soft-type colloidal particles despite of high viscosity and particle concentration. While the swollen CPBs in good solvents indicate high elasticity, this work reveals the relationship between the shear oscillation and the higher-order structure of colloidal particles with high elasticity. This work can result in the development of functional materials usin PSiP applied to electronic devices.

In **Chapter 6**, I fabricated and analyzed higher-order structures of the composites of CPB-modified nanoparticles and ionic liquid and revealed the concentration-dependent crystallization of PSiP. The higher-order (crystal) structures of PSiP/IL composites are rhcp and fcc, although the structure depends on the concentration of PSiP. While the swollen CPBs in good solvents indicate high elasticity, this work reveals the relationship between the concentration and the higher-order structure of colloidal particles with high elasticity. In future, the relationship between the concentration and the interparticle potential of colloidal particles will be investigated to understand the formation of higher-order structure of colloidal particles with polymer brushes.

In **Chapter 7**, I have succeed in fabricating PSiP membrane which formed a regularly-arrayed structure in the presence of I^-/I_3^- by designing of CPB. PSiP membrane had a high conductivity n the presense of I^-/I_3^-, achieving that quasi-solid-state DSSC was fabricated by means of PSiP membranes.

List of Publications

Chapter 2.

(1) USAXS Analysis of Concentration-dependent Self-assembling of Polymer-brush-modified Nanoparticles in Ionic Liquid: [I] Concentrated-brush Regime

Y. Nakanishi, R. Ishige, H. Ogawa, K. Sakakibara, K. Ohno, T. Morinaga, T. Sato, T. Kanaya, and Y. Tsujii

Submitted to *J. Chem. Phys.*

Chapter 3.

(2) USAXS Analysis of Concentration-dependent Self-assembling of Polymer-brush-modified Nanoparticles in Ionic Liquid: [II] Semi-diluted-brush Regime

Y. Nakanishi, R. Ishige, H. Ogawa, Y. Huang, K. Sakakibara, K. Ohno, T. Kanaya, and Y. Tsujii

Submitted to *J. Chem. Phys.*

Chapter 4.

(3) Development of Novel Nano-systems for Electrochemical Devices by Hierarchizing Concentrated Polymer Brushes

Y. Tsujii, **Y. Nakanishi**, R. Ishige, K. Ohno, T. Morinaga, and T. Sato

Intelligent Nanosystems for Energy, Information and Biological Technologies **2016**, 195–215.

Chapter 5.

(4) Understanding Dynamics of Self-Assembling of Polymer-brush-modified Nanoparticles/Ionic Liquid Composites by Shear Oscillation

Y. Nakanishi, H. Eguchi, K. Sakakibara, K. Ohno, M. Takenaka, and Y. Tsujii

To be submitted.

Chapter 6.

(5) Understanding Dynamics of Self-Assembling of Polymer-Brush-Modified Nanoparticles/Ionic Liquid Composites by Dip-Coating Method

Y. Nakanishi, H. Ogawa, R. Ishige, K. Ohno, T. Kabe, T. Kanaya, and Y. Tsujii

To be submitted.

Chapter 7.

(6) Fabrication of quasi-solid electrolyte of concentrated-polymer-brush-modified nanoparticles self-assembled in iodide-containing ionic liquid toward dye-sensitized solar cell

Y. Nakanishi, K. Sakakibara, K. Ohno, T. Morinaga, T. Sato, S. Yoshikawa, T. Sagawa, and Y. Tsujii

Submitted to *J. Polym. Sci. A*

Other Associated Publications.

(7) Visualization of Individual Images in Patterned Organic-Inorganic Multilayers Using GISAXS-CT

H. Ogawa, Y. Nishikawa, M. Takenaka, A. Fujiwara, **Y. Nakanishi**, Y. Tsujii, M. Takata, and T. Kanaya

Langmuir **2017**, *33*, 4675–4681.

(8) Controlled synthesis of High-molecular-weight ABA Triblock Copolymers by Atom Transfer Radical Polymerization and their Formation of Ionic Gels

S. –Y. Hsu, R. Ishige, **Y. Nakanishi**, K. Ohno, H. Watanabe, and Y. Tsujii

Submitted to *Macromolecules*

(9) Fabrication and Functionalization of Polymer-brush-modified Epoxy-based Monoliths

Y. Nakanishi, R. Wada, K. Sakakibara, N. Ishizuka, and Y. Tsujii

To be submitted.

Acknowledgements

The present investigations were carried out at the Institute for Chemical Research (ICR), Kyoto University in the period from April 2009 to February 2018.

I would like to express sincere gratitude to an outstanding supervisor, Prof. Yoshinobu Tsujii for his invaluable guidance, stimulating discussions and heartfelt encouragement throughout this work. I am grateful to Prof. Shigeru Yamago, Prof. Mikihito Takenaka, and Emer. Prof. Shinzaburo Ito (Department of Polymer Chemistry, Kyoto University) for their helpful advices on this thesis.

One of the strong research skills that I acquired was the ability to use SAXS, which was taught by Assist. Prof. Ryohei Ishige (Tokyo Institute of Technology) and Assist. Prof. Hiroki Ogawa. In addition, a window of opportunity to start up using synchrotron X-ray beamlines at SPring-8 was provided by Prof. Toshiji Kanaya (High Energy Accelerator Research Organization). Assoc. Prof. Masatoshi Tosaka gave me a lot of technical information about SAXS. Without their enthusiastic guidance, valuable discussions and support, I would have failed to get any experimental information about SAXS/USAXS.

I wish to show my appreciation to all of my colleagues in Prof. Tsujii's Laboratory for their kind help, particularly, to Assoc. Prof. Kohji Ohno, Assist. Prof. Keita Sakakibara, Dr. Yun Huang, and Dr. Hiroshi Eguchi for their active collaborations in part of the study and to Dr. Shu-Yao Hsu for his useful suggestions. I would also like to express my gratitude to Prof. Takaya Sato, Assoc. Prof. Takashi Morinaga (National Institute of Technology, Tsuruoka College), Emer. Prof. Susumu Yoshikawa (Institute of Advanced Energy, Kyoto University), and Prof. Takashi Sagawa (Graduate School of Energy Science, Kyoto University) for their attentive contributions.

The synchrotron USAXS experiments for this work were performed at BL19B2 (Proposal No. 2014B1648, 2015A1718, and 2017B1638), BL03XU (Proposal No. 2017A1845, 2017A7213, and 2017B7283), and BL40B2 (Proposal No. 2014B1469) in SPring-8 with the approval of the Japan Synchrotron Radiation Research Institute (JASRI). I thank Dr. Masugu Sato, Dr. Takeshi Watanabe, Dr.

Keiichi Osaka, Dr. Taizo Kabe, and Dr. Noboru Ohta (JASRI/SPring-8) for their assistance in the experiments at BL19B2, BL03XU, and BL40B2.

I would like to express my appreciation to my friends in ICR, Dr. Yasunobu Egawa, Dr. Ryo Hiramatsu, Dr. Yoshitaka Nishihara, Dr. Takashi Shigeta, Dr. Shotaro Takano, Dr. Jun-ichiro Takaya, and Mr. Haruki Ohfuji, who always engaged in stimulating debates and discussions throughout in studies. I am also much obliged to many people in (or related to) ICR, especially Dr. Hirokazu Masai (National Institute of Advanced Industrial Science and Technology), Assist. Prof. Katsuhiko Takeuchi, Assist. Prof. Bunta Watanabe, Assist. Prof. Eiichi Kayahara, Lecturer Tatsuya Fukushima (Kobe University), and Ms. Keiko Okubo, for their continuous motivation. Moreover, I’m deeply grateful to Dr. Takanori Shima, Mr. Naoya Shigesada, Mr. Takamasa Shimizu (“Gesukai”), Mr. Hiroaki Morita, Dr. Yuria Asao (Debate Circle Co-de), Mr. Yasuaki Okamoto (Meisei Junior and Senior High School), Prof. Mitsuharu Mizuyama (Kyoto University of Education), Prof. Osamu Ikeda (Kyoto Tachibana University), Assoc. Prof. Yoji Tanaka (Doshisha University), Mr. Tsutomu Sugiyama (Kyoto Tachibana Junior and Senior High School), Assist. Prof. Hiroki Tamai (Tohoku Gakuin University), Prof. Kazuko Hirose, Dr. Asato Mizuno, Mr. Masayuki Yamada (Nagoya University Contract Bridge Circle), Mr. Genkai Kitano, Ms. Teiko Kitano, Mr. Genshun Kitano (Kyodai Seiki Juku/Saishouji), and an extremely large number of other people related to me for their warm encouragement.

I wish to express my heartfelt thanks to my family, Shizue Nakanishi (grandmother), Yukiko Nakanishi (mother), Shiro Nakanishi (brother of fraternal twins) and Tomoko Nakanishi (sister-in-law), for their continuous support and encouragement.

Finally, I would like to send a special letter to my late grandfather Masami Nakanishi, informing him that my extraordinary voyage for a Ph.D. has finally been completed.

February, 2018

Yohei Nakanishi